2/3/6/79

NUREG/CR-0422
SAND78-1901
Vol. 8
R-3

Light Water Reactor Safety Research Program Quarterly Report April - June 1978

Nuclear Fuel Cycle Safety Research Department

Printed January 1979

Sandia Laboratories

SF 2900 Q(7-73)

Prepared for

U. S. NUCLEAR REGULATORY COMMISSION

DISCLAIMER

This report was prepared as an account of work sponsored by an agency of the United States Government. Neither the United States Government nor any agency thereof, nor any of their employees, makes any warranty, express or implied, or assumes any legal liability or responsibility for the accuracy, completeness, or usefulness of any information, apparatus, product, or process disclosed, or represents that its use would not infringe privately owned rights. Reference herein to any specific commercial product, process, or service by trade name, trademark, manufacturer, or otherwise does not necessarily constitute or imply its endorsement, recommendation, or favoring by the United States Government or any agency thereof. The views and opinions of authors expressed herein do not necessarily state or reflect those of the United States Government or any agency thereof.

DISCLAIMER

Portions of this document may be illegible in electronic image products. Images are produced from the best available original document.

NOTICE

Available from
National Technical Information Service
Springfield, VA 22161

NUREG/CR-0422
SAND78-1901
R-3

LIGHT WATER REACTOR SAFETY RESEARCH PROGRAM
QUARTERLY REPORT
APRIL - JUNE 1978
Vol. 8

Nuclear Fuel Cycle Safety Research Department
Sandia Laboratories, Albuquerque, NM 87185

Person in Charge: M. Berman

Date Published: January 1979

APPROVED: D. L. McCloskey
Manager, Nuclear Fuel Cycle Safety Research

Director, Nuclear Fuel Cycle Programs

Sandia Laboratories
Albuquerque, NM 87185
operated by
Sandia Corporation
for the
U. S. Department of Energy

Prepared for
Division of Reactor Safety Research
Office of Nuclear Regulatory Research
U. S. Nuclear Regulatory Commission
Washington, DC 20555
Under Interagency Agreement DOE 40-550-75
NRC FIN Nos. A-1019, -1030, -1205, and -1207

CONTENTS

LIGHT WATER REACTOR SAFETY RESEARCH PROGRAM

1. Molten Core/Concrete Interactions Study

1.1 Summary

The Molten Core/Concrete Interactions Study began July 15, 1975, to provide a qualitative, extensive exploration of the phenomena associated with contact between molten-core materials and concrete. The experimental elements of this study are divided into four categories:

1. Deposition of Corium-type melts onto concrete
2. Kinetics and stoichiometry of the thermal decomposition of concrete
3. Response of concrete to high heat fluxes at one surface
4. Simulation experiments which explore phenomena at the interface between a melt and a decomposing solid.

Experimental results are being incorporated in a computer model and a scaling analysis. They will establish scaling parameters for the system and identify key elements of the melt/concrete interaction. A complete project description of the study was issued in October 1975.[1]

During this quarter two especially notable experiments were performed. The first investigated the erosion of concrete by hot, solidified prototypic core material. A cylindrical steel slug was centered in the cavity of a limestone concrete crucible and heated inductively for about 2.4 hours. Its temperature increased to approximately 1380°C during the first hour, after which it was essentially constant for the remainder of the test. Melting of the concrete occurred when the steel temperature reached a value of about 1340°C. Concrete erosion occurred in both downward and radial directions at rates of approximately 1.25 and 0.87 inches/hour, respectively. The downward erosion was fairly uniform but the radial erosion was not; the latter exhibited a maximum in the vicinity of the midpoint of the crucible.

The second experiment provided a striking demonstration of the tremendous capability for detailed, continuous, real-time observation of a melt/concrete interaction that is possible using a combined pulsed X-ray/image intensification system. The X-ray technique was employed during a small-scale test in which a thermitically produced steel melt interacted with a limestone crucible similar to that used in the first test. The resulting videotape recording of the X-ray image provides

a pictorial representation of the interaction having exceptional resolution and detail. It contains a wealth of information about many features of the melt/concrete interaction including:

- Spatial and temporal dependence of concrete erosion
- Melt/concrete interface phenomena
- Gas mass transfer and reaction kinetics
- Transit time of gases passing through the melt
- Melt circulation
- Crush formation on the melt surface and its effect on gas transport through the melt.

The X-ray technique is capable of providing valuable information about these and other aspects of interactions between prototypic materials that has been unavailable heretofore. When analyzed in conjunction with quantitative data, its value is further enhanced. Such information is essential to understanding and modeling the real phenomena.

The analytical effort during the quarter concentrated on development of the improved molten core/concrete interaction model, CORCON. The molten pool layering configurations, chemical reactions, and the mass and energy sources and flow paths to be included in the model were determined. The numerous computations required for the model were defined and organized into a logical sequence. A flow diagram of the model was completed. Programming was begun and concentrated on routines for entering input data and plotting results. Computer plot routines were developed and made operational for providing time histories of pertinent variables and plots and movies showing cavity growth due to concrete erosion. Work continued on the development of phenomenological models for fission product decay heat generation and core/concrete interface heat transfer.

1.2 Molten Core/Concrete Interaction Experimental Program (D. A. Powers)

1.2.1 Attack of Hot Solid Material on Concrete

Attention concerning the interaction of core materials with concrete has been focused on the aggressive behavior of molten materials. However, a phase arises in any core meltdown accident at which the internal heat generation by fission products is insufficient to maintain the core materials in the molten state. It is often conveniently assumed that significant core debris/concrete interactions cease when this state is reached. Such an assumption ignores the observed temperature ranges of concrete melting which are less than the solidification temperatures of core-melt constituents.[2] When continued erosion by solidified core materials is recognized, it is usually assumed to proceed at a slow rate. The attack on concrete by hot solidified, prototypic core materials was studied in the following experiment.

Experiment -- A schematic diagram of the experiment arrangement is shown in Figure 1-1. A cylindrical steel slug 3.25 inches in diameter, 4.25 inches long, and weighing 11 pounds (5 kg) was centered in the cavity of a limestone concrete crucible. The cavity was 3-1/2 inches in diameter and 4-1/2 inches long, providing a 1/8 inch gap between the side of the steel cylinder and the cavity walls. The concrete block itself was 6 inches in diameter and 12 inches long. The composition of the limestone concrete was FeO - 1.44, K_2O - 1.22, CaO - 31.2, SiO_2 - 35.7, Al_2O_3 - 3.6 w/o. The onset of melting of the concrete occurred at about 1100°C. Complete liquefaction of the concrete was estimated to occur at 1400°C.

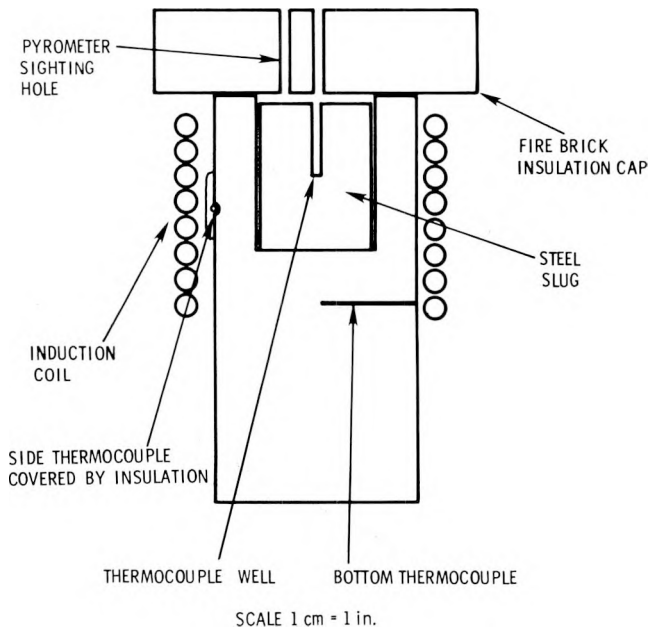

Figure 1-1. Experimental Arrangement Used in Test Burn 2

An ungrounded, 0.040-inch OD stainless steel sheathed, MgO insulated, type K thermocouple was located on the external wall of the crucible 1-1/4 inches above the cavity bottom. The thermocouple was held in a 1/8-inch deep by 1/8-inch wide groove in the wall by a Sauereisen No. 63 castable refractory which was covered by 1/16-inch thick asbestos paper. The thermocouple was affixed in a horizontal attitude on the wall for two inches (50 sheath diameters).

A second, similar, thermocouple was embedded in a 1/4-inch diameter by 2-3/4 inches deep horizontal well 1-1/2 inches below the cavity bottom with Sauereisen No. 63 castable refractory.

The crucible was capped with a 2-1/2-inch thick fireclay block. A type S bare junction thermocouple (0.020-inch wire diameter) was passed through the cap and into a 3/8-inch diameter by 2 inches long, silica-sheathed wall on the centerline of the steel cylinder.

The above assembly was located in an 8-turn helical induction coil. The coil extended from 1/2 inch to 6-1/2 inches below the top of the crucible. The coil was energized by a 50 kW, 3000 Hz Inducto 50 power supply. The apparent power used during the experiment was 5-1/2 to 6 kW. The power factor varied between 0.8 and 0.7 during the test.

All thermocouple data collected during the test were recorded from the analog outputs of commercial digital readouts. The integrating character of these readouts was used to eliminate alternating current noise from the induction power supply.

Results -- The steel temperature during the test is shown in Figure 1-2. As would be expected, the temperature of the steel rose rapidly (~ 1.2°C/min) until the Curie temperature (~ 725°C) was reached. The temperature then rose at a more modest rate (~ 0.3°C/min) until temperatures near 1380 ± 20°C developed in the steel. The temperature was then approximately constant for the remainder of the test (total test time was 8000 seconds).

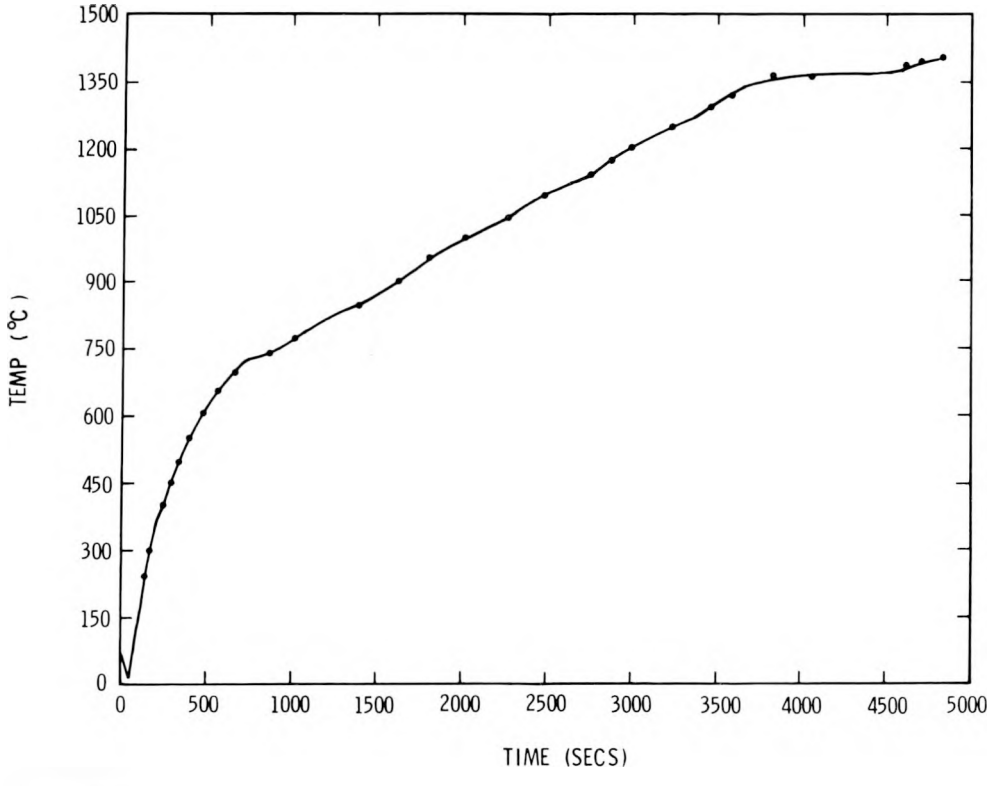

Figure 1-2. Test Burn 2: Steel Temperature

If it is assumed that, between 800° and 1300°C, the steel was adiabatically heated, a lower bound estimate of the power deposition in the metal of 1.0 kW is found. The coupling of apparent power to the steel is then only 20% efficient in this temperature range. When the temperature of

the steel reached 1380 ± 20 °C, power deposited in the steel by induction was transferred to the surroundings. Radiant heat losses from the top of the steel through the 2-1/2 inch thick insulating cap may be neglected.

When the steel reached a temperature of 200 °C, steam began to condense about the test apparatus. At a steel temperature of 900 °C, more vigorous gas evolution occurred. At 1340 ± 10 °C liquid oxides were spewed out of the crucible through gaps in the capping assembly.

Temperatures recorded by the concrete thermocouples are shown in Figures 1-3 and 1-4. In each case the temperature rise in the concrete is rapid until a temperature of 120 ± 10 °C is reached. Then an arrest in the rate of temperature increase occurred whose duration is about 600 seconds for the side thermocouple and 500 seconds for the thermocouple below the cavity of the crucible. Following these arrests, additional arrests in temperature rise occurred at about 400° and 700 °C. The latter of these arrests in the temperature-time curves is barely detectable in the data from the thermocouple below the crucible cavity.

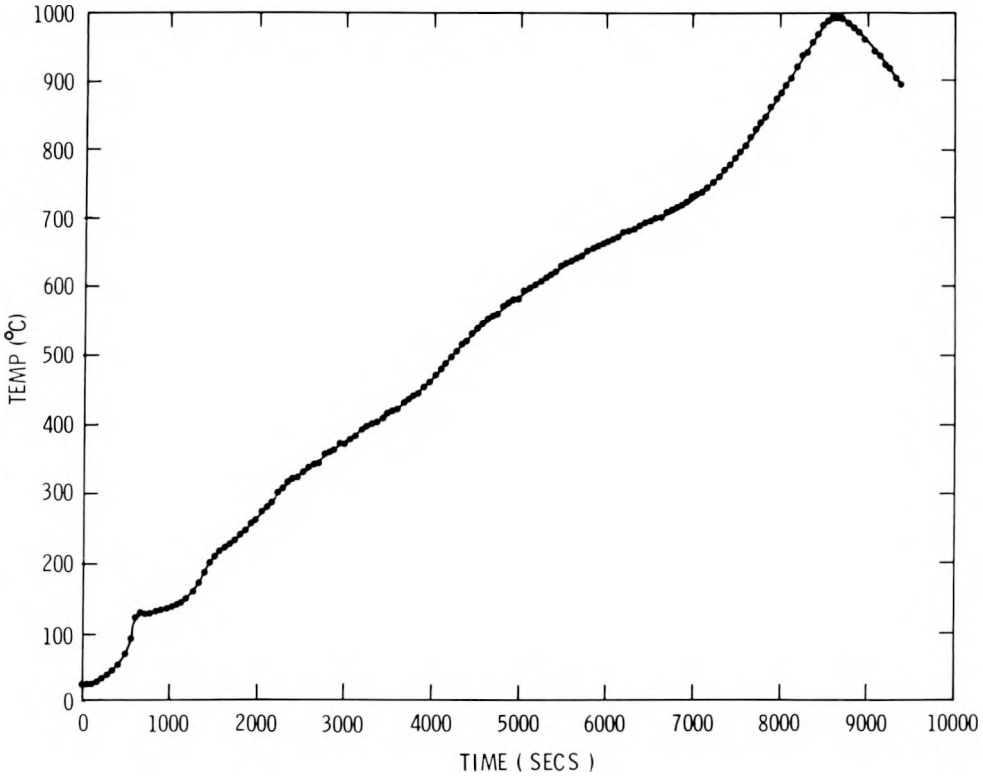

Figure 1-3. Test Burn 2: Side Thermocouple

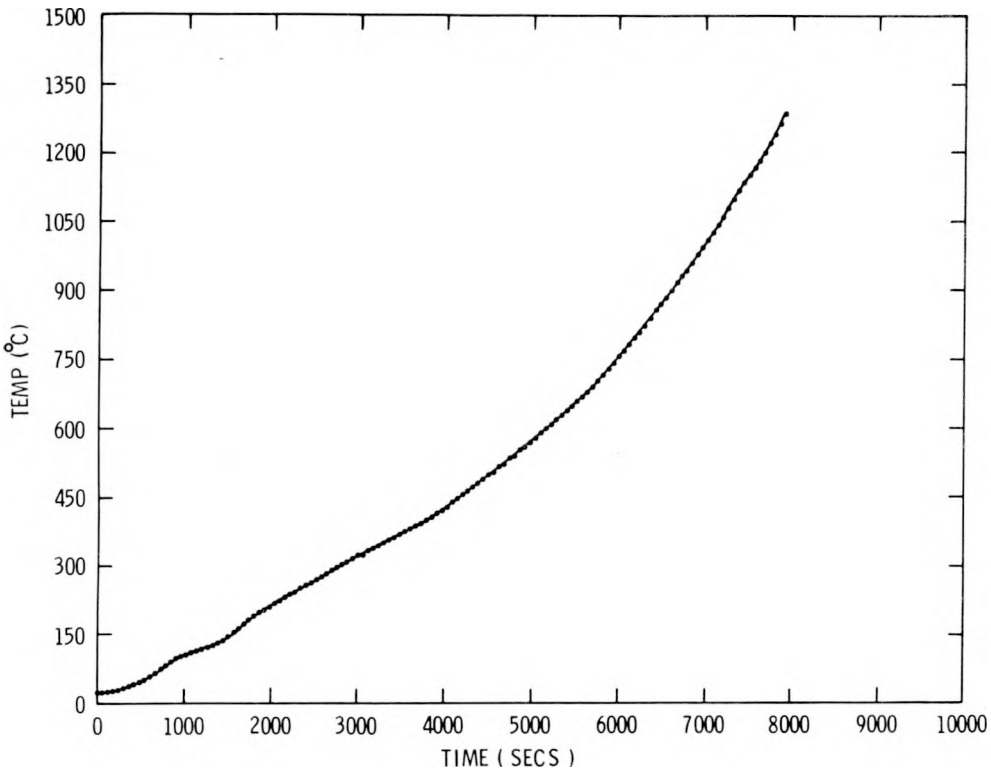

Figure 1-4. Test Burn 2: Bottom Thermocouple

When concrete melting occurred a viscous, black, glassy melt boiled up between the steel and the crucible cavity walls. Erosion of the concrete in a downward direction occurred at a rate of 1.25 inches/hour (calculated from thermocouple burnout times). The radial erosion was somewhat less at about 0.87 inches/hour. Downward erosion was fairly uniform across the bottom of the crucible cavity. Radial erosion was not uniform. Maximum erosion occurred somewhere near the midpoint of the crucible cavity. Unfortunately, the crucible and its contents shattered during cooling before any quantitative measure of the nonuniformity could be made.

1.2.2 Direct Observation of the Interaction Between a High-Temperature Melt and Concrete

It has become increasingly clear that most of the phenomena pertinent to questions of reactor safety are strongly dependent on processes at the melt/concrete interface. As an example, heat transfer from the melt to the concrete dictates not only concrete erosion, but also the extent of gas evolution and the elemental composition of those gases.

Interfacial behavior of high-temperature melts has been the object of considerable speculation. Data concerning the interfacial behavior have been restricted to the following sources:

- Simulation experiments
- Inferences from posttest analyses of experiments with prototypic materials.

Both these sources are fairly unsatisfactory. Simulation experiments are subject to criticism of the choice of simulant. Posttest inspections yield only the final state of the interface which is affected by all events in the test including the cooling after melt solidification.

True understanding of the melt/concrete interaction can come about only if continuous, reliable, real-time observation of the interaction is possible. The feasibility of doing this has been demonstrated during this report period. A pulsed X-ray system and an image intensification system have been used to observe a melt of steel interacting with limestone aggregate concrete. Only a brief account of the experiment is given here.

Experiment -- The crucible was very nearly identical to the one described above. The thermocouple below the crucible cavity was only 1-1/4 inch below the initial bottom of the cavity. The crucible was equipped with an instrumentation tower similar to, but somewhat smaller than the one used in the NSS series of tests.[2] The instrumentation tower allowed gas generation measurements to be made and gas samples to be taken. The crucible was charged with 1978 grams of a stoichiometric aluminum-iron oxide mixture (2) which was reacted to form the high-temperature melt.

The X-ray source was a Varian model 1500 Linatron. The device was operated at 7.5 MeV and a dose rate of 500 rads/minute. A Decalix image intensification system was used to create a visible reproduction of the X-ray image which was recorded on video tape.

Results -- A copy of the video tape is now in the hands of the Fuel Behavior Branch of the Nuclear Regulatory Commission. Collateral data collected during the test are shown as follows:

- Temperature below cavity - Figure 1-5
- Temperature of crucible wall - Figure 1-6
- Gas generation rate - Figure 1-7
- Gas composition versus time - Figure 1-8.

The metallothermic reaction required 2.4 seconds to form the melt completely. The reaction front was quite uniform once it had passed the steel alignment insert at the top of the crucible. For a period of about 2 seconds following contact between the liquid steel and the bottom of the crucible, the melt was subjected to vigorous surges. Then the melt was violently levitated from the surface by gases liberated from the concrete. Melt surging and levitation continued for about half a minute. Gas liberation at this time became more quiescent. Gases were vigorously expelled about the periphery of the melt. These evolved gases considerably reduced the amount of time the melt was in contact with the crucible cavity walls.

Localized gas evolution points also developed at the base of the crucible cavity at points on either side of the crucible centerline as shown in the sketch in Figure 1-9.

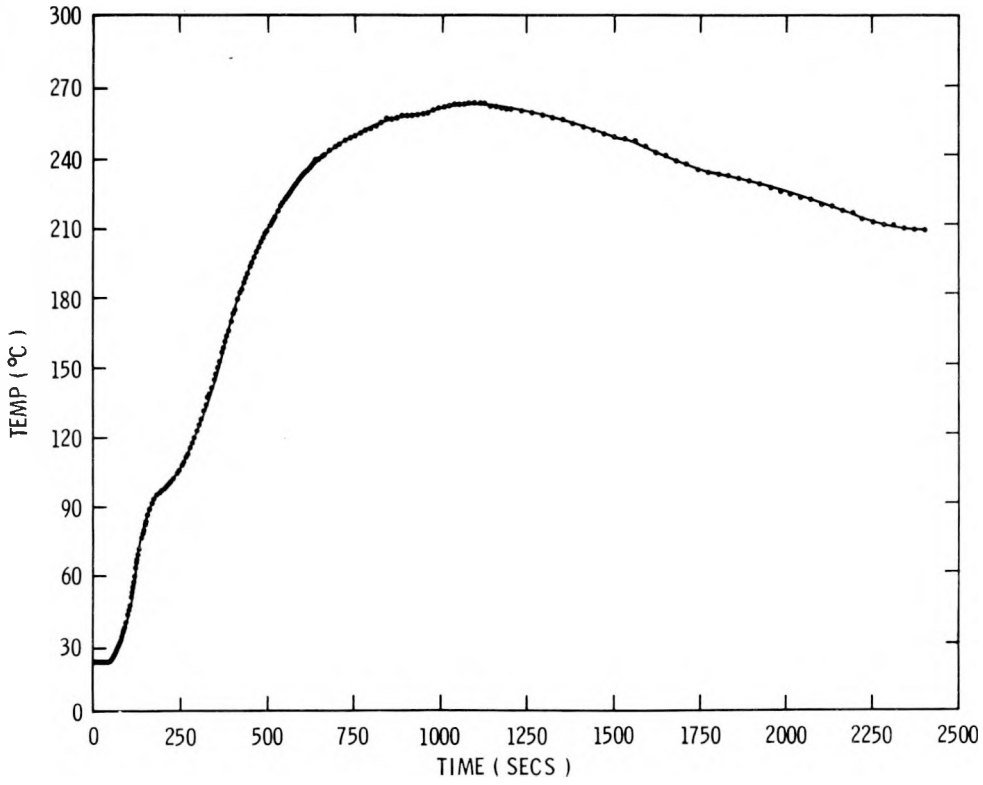

Figure 1-5. Test Burn 1: Thermocuple TC4

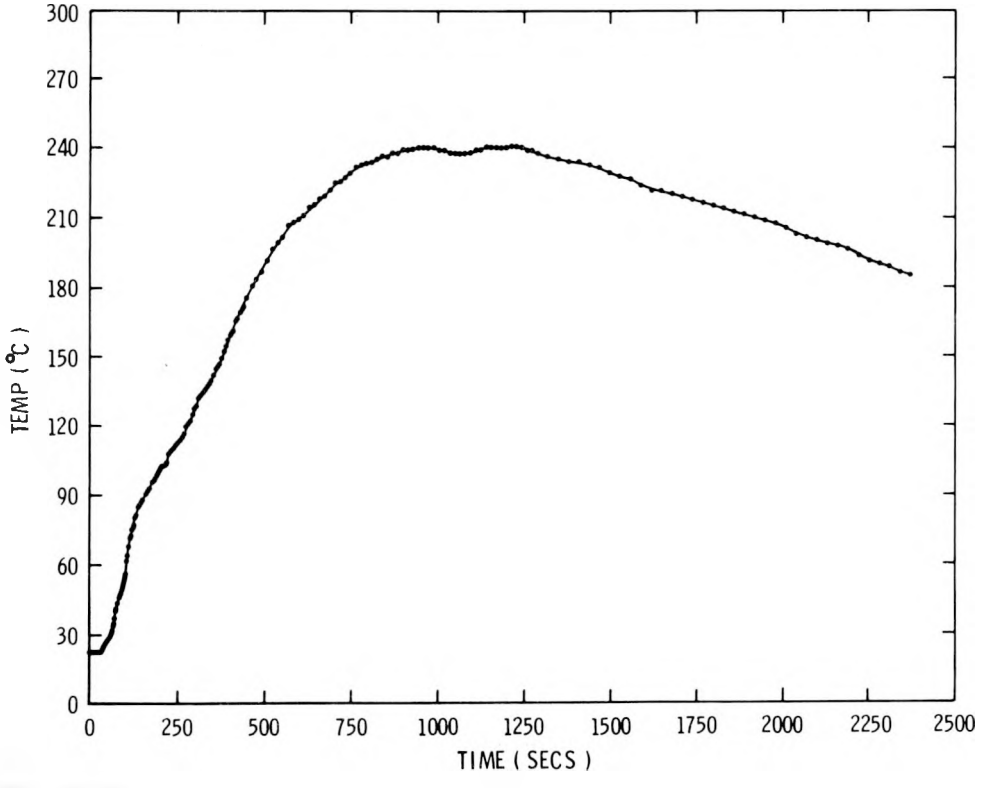

Figure 1-6. Test Burn 1: Thermocouple TC5

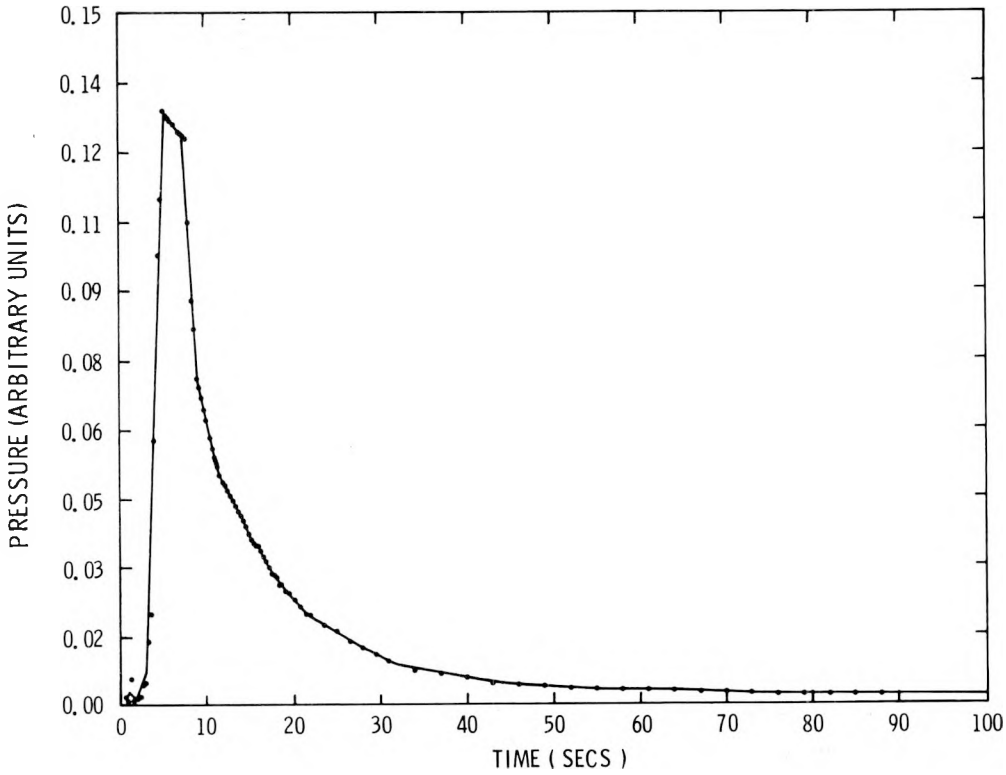

Figure 1-7. Test Burn 1: Gas Flow Data

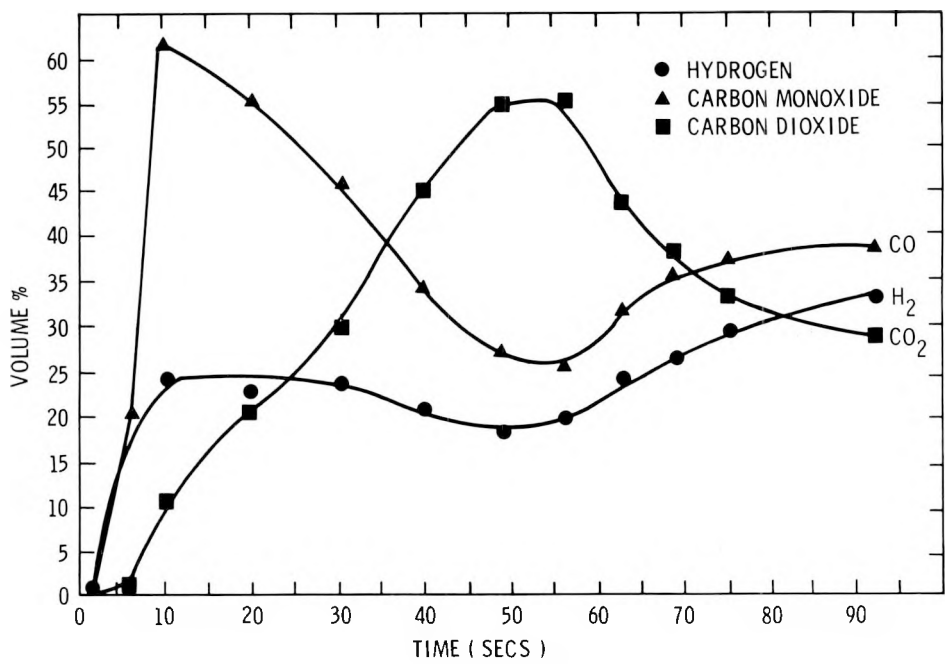

Figure 1-8. Gas Composition vs Time for Test Burn 1

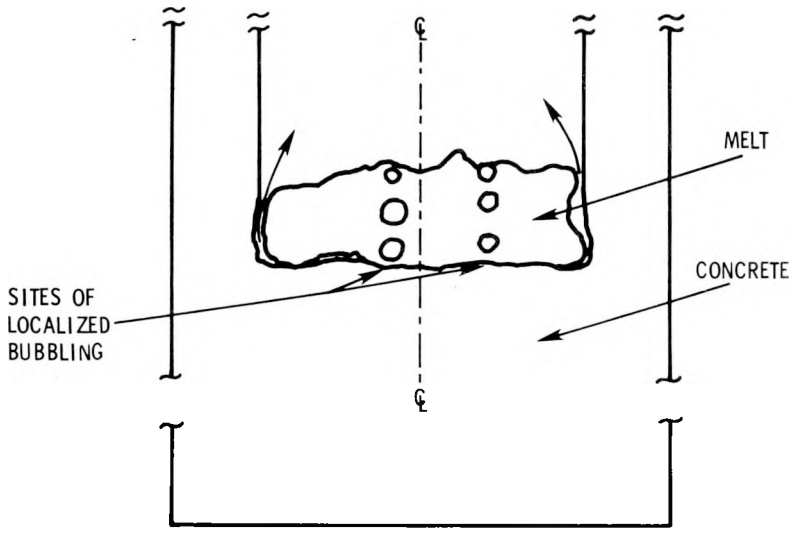

Figure 1-9. Sketch of Localized Bubbling Observed in Test Burn 1

A viscous crust began to develop on the upper surface of the melt 56 seconds after the start of the test. Solidification of the steel melt began 63 seconds after the start of the test and was complete 5 seconds later. No melt temperature measurements were made during Test Burn 1, but the solidification behavior suggests the time-temperature curve shown in Figure 1-10.

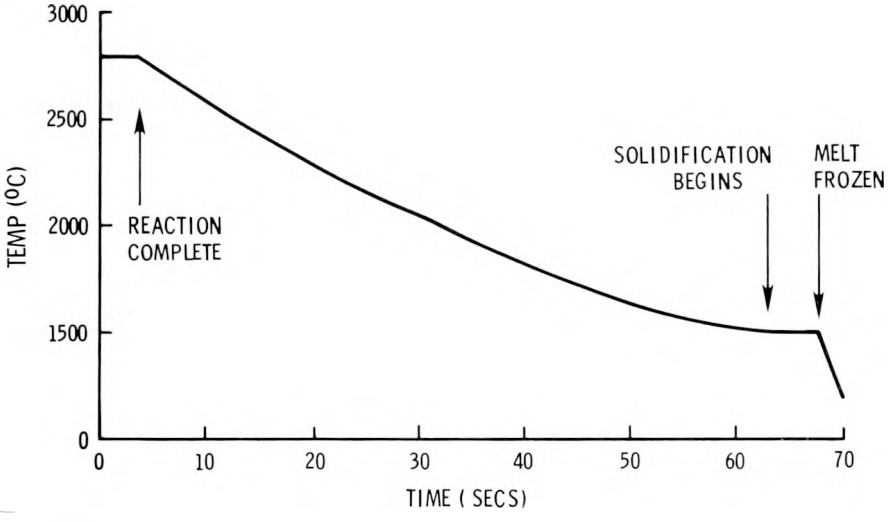

Figure 1-10. Hypothesized Melt Temperature Behavior vs Time

The amount of information available from the motion picture of the melt behavior is overwhelming. Among the many features of the melt/concrete interaction which may be studied with this X-ray technique, in conjunction with quantitative diagnostics, are:

- Spatial and temporal dependence of concrete erosion
- Melt/concrete interface phenomena
- Gas mass transfer and reaction kinetics
- Transit time of gases passing through the melt
- Melt circulation
- Crust formation on the melt surface and its effect on gas transport through the melt.

Test Burn 1 was a demonstration of the feasibility of the experimental technique. It is quite clear from the results that some features of the experiment were not adequate for producing data concerning the prototypic interactions which may be scaled up to realistic situations. In particular it was noted that gas bubbles formed at the melt/concrete interface had dimensions comparable to the melt thickness and not small in comparison to the cavity dimensions.

Attempts are now underway to repeat Test Burn 1 in a way that will alleviate these problems.

1.3 Molten Core/Concrete Interaction Analytical Program (J. F. Muir)

1.3.1 Model Development

Development of an improved molten core/concrete interaction model (CORCON) continued. Alternative pool layering configurations to be treated were defined. These range from a single layer containing either all metals, all oxides, or a homogeneous mixture of the two, to a maximum of three melt layers (two oxidic layers separated by a metallic layer) surmounted by a coolant layer. The latter configuration is illustrated schematically in Figure 1-11. Also included are the melt atmosphere and surroundings, and the melt/concrete and coolant/concrete interface regions.

The chemical reactions to be incorporated in the interaction model were determined. They include the following:

- Oxidation reactions between the concrete decomposition gases (H_2O and CO_2) and metallic species (Fe, Zr, Cr, Ni) present in the metallic layer.[2] Consideration is given to reactions occurring both at the periphery of, and within, the metallic layer. The former involve gases from the concrete that do not enter the melt but pass up through the interface region surrounding the pool, while the latter involve gases that enter the metallic layer along the bottom and sides and percolate up through the layer. Gaseous reaction products flow up through or around the pool to the atmosphere, while the metallic oxides produced rise to accumulate in the upper oxidic layer. Reaction energies are added to the bulk energy of the metallic layer.

- Reduction reactions between gases in the melt atmosphere (H_2 and CO) and metallic oxides (FeO, NiO, and Cr_2O_3) in the top oxidic layer, when such a layer is present. These reactions occur only in the absence of a coolant layer on top of the core melt. Gaseous reaction products return to the atmosphere, while the metallic species released are transported to metallic layer. The energies associated with these reactions are subtracted from the bulk energy of the top oxidic layer.

- Gas phase chemical reactions required to bring the gas mixture above the pool to a state of thermodynamic and chemical equilibrium. The associated reaction energies are added to or subtracted from the bulk gas energy.

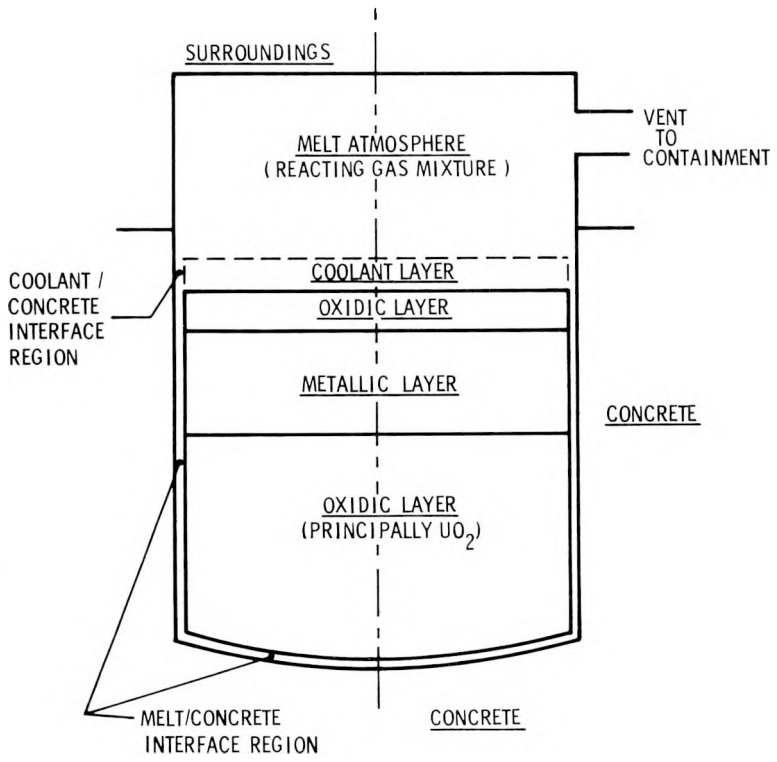

Figure 1-11. Schematic of Possible Pool Layering Configuration

Mass and energy sources and flow paths to be included in the model were determined and are shown schematically in Figure 1-12. These include the fission product decay heat generated within the core melt (E_D); energies from the oxidation (R_1), reduction (R_2), and gas phase equilibrim (R_3) reactions; and heat and mass transport among layers within the pool, between the pool and the concrete (across the interface region), the atmosphere, and the atmosphere surroundings, along the interface region to the atmosphere (for a continuous gas film interface configuration), and between the atmosphere and its surroundings including venting to containment.

The numerous computations required for initiation of a CORCON calculation, and during each subsequent time step, were defined and organized into a logical sequence. This sequence is illustrated by the pseudo-flow diagram presented in Figure 1-13. The program, as it is being written, contains a large number of subroutines in which the various computations are performed and a short main program which controls the flow.

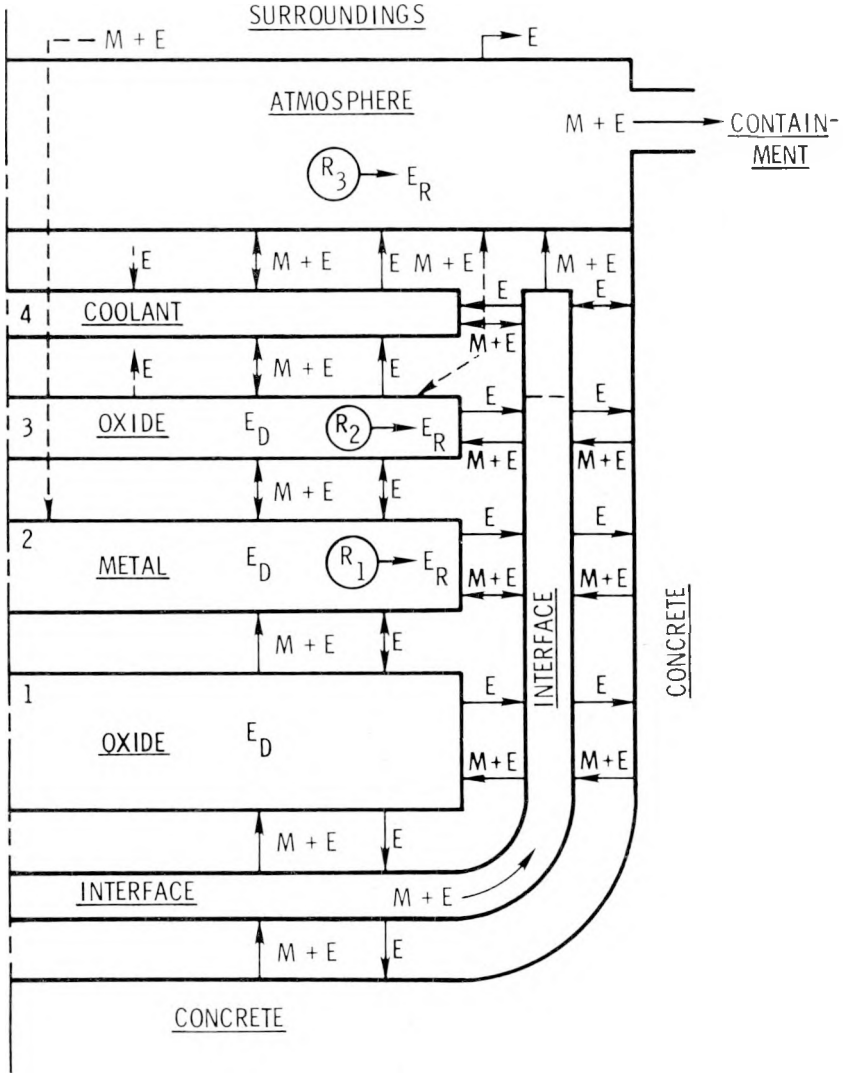

Figure 1-12. Mass and Energy Sources and Flow Paths

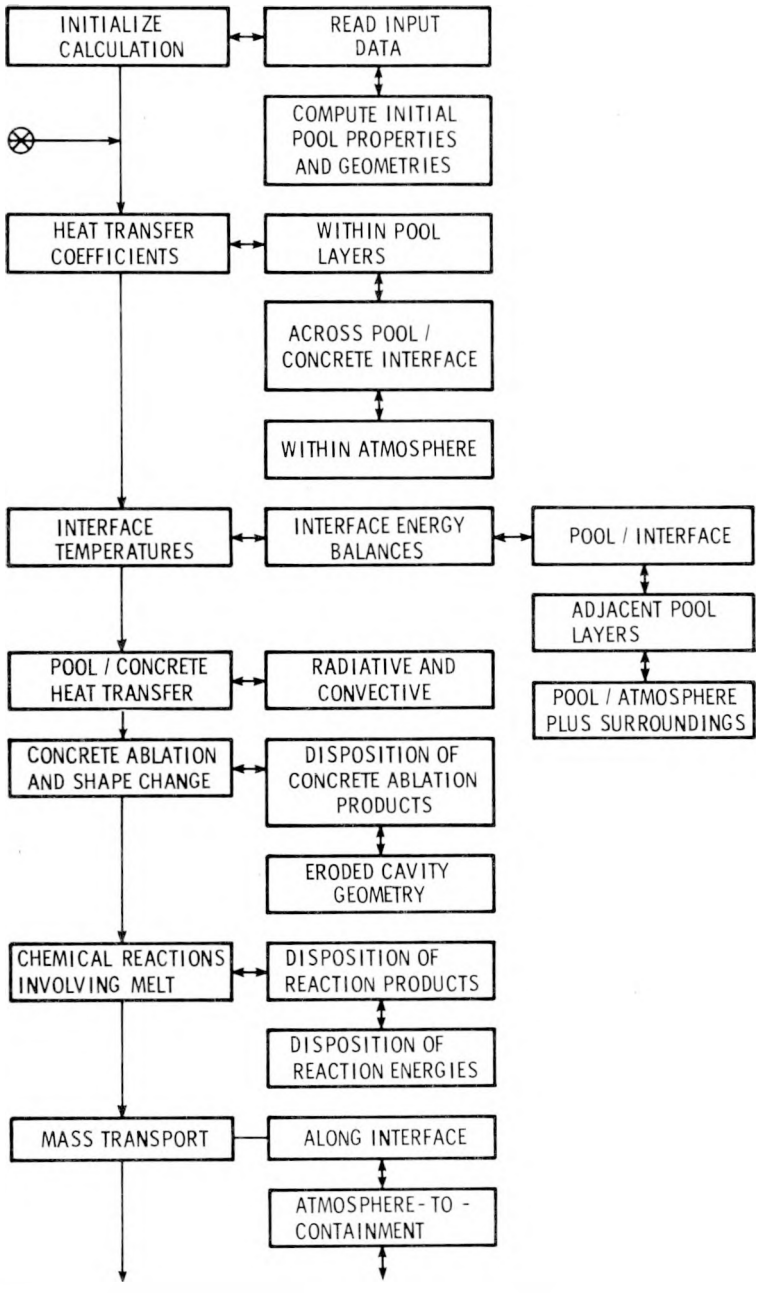

Figure 1-13. Computation Sequence

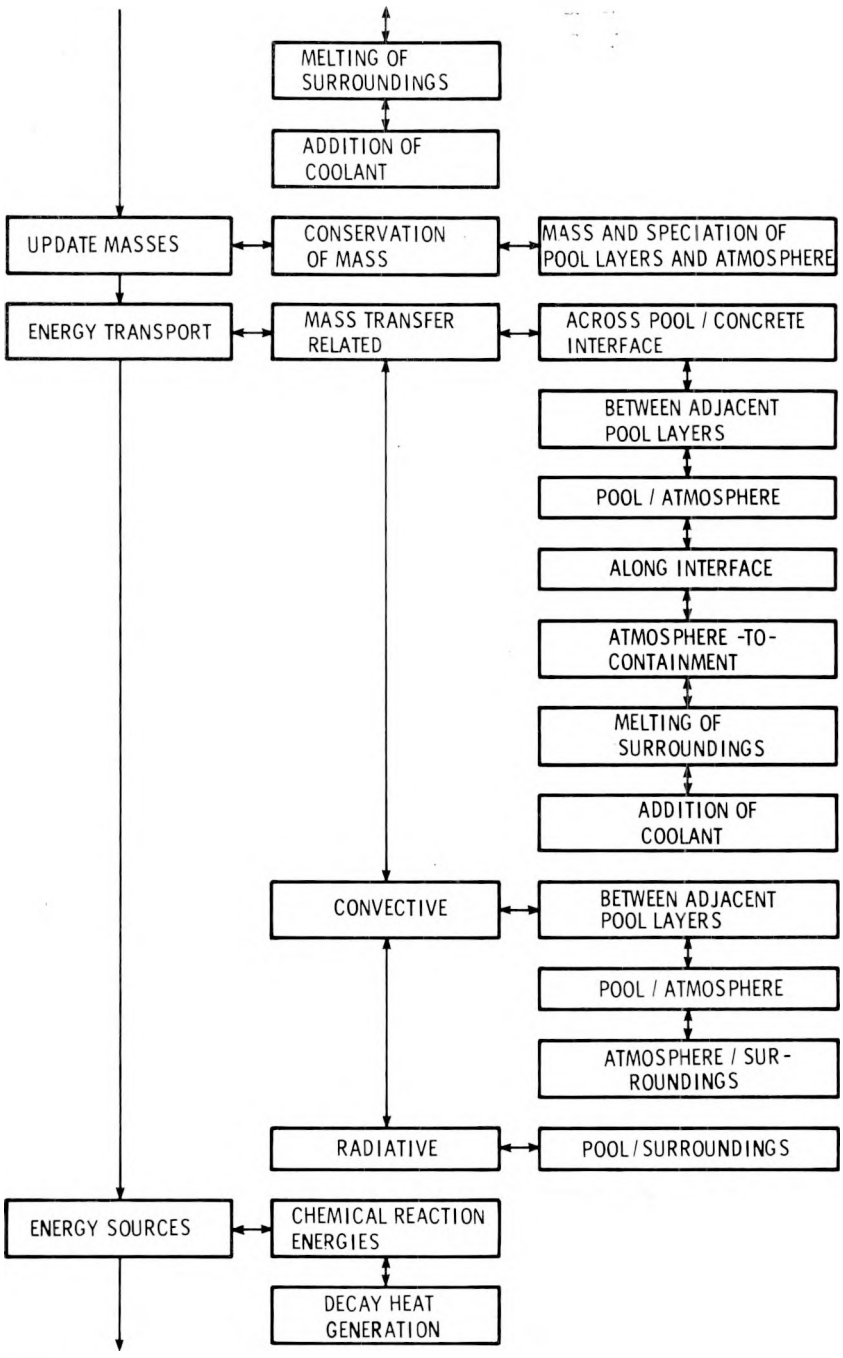

Figure 1-13. (cont)

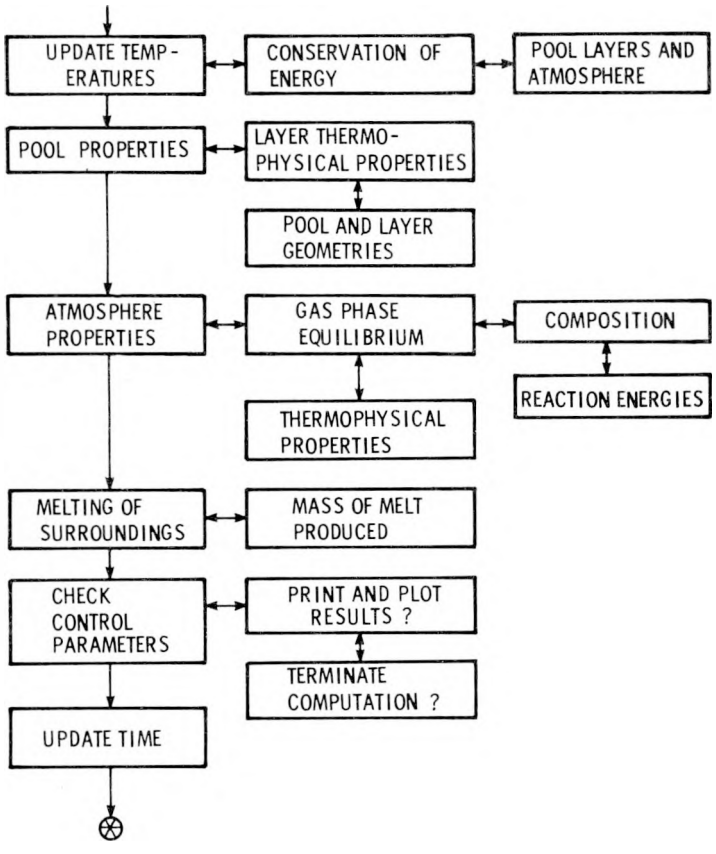

Figure 1-13. (concluded)

Programming was initiated and concentrated on routines for entering input data and plotting results. Two types of computer plot routines were developed and debugged using the INTER code. The first enables parameters of interest to be plotted versus time. Although presently configured for providing temporal variations in the most important parameters, (e.g., horizontal and vertical erosion, metallic and oxidic layer temperatures, and volumes of H_2O, CO_2, H_2, and CO gas generated), it can be readily modified to plot the time history of almost any parameter of the problem. A sample plot is presented in Figure 1-14.

The second routine plots the shape of the concrete cavity at specified times. This illustrates the two-dimensional character of the cavity growth as the concrete is eroded by the core melt. A sample plot is shown in Figure 1-15. Although this example depicts the cylindrical-hemispherical segment cavity geometry employed in INTER, the routine has the capability of plotting any axisymmetric shape defined in terms of n points with interconnecting line segments (currently n = 60). Another feature of this plot routine is that it can be used to make computer

movies of the cavity growth with time. Trial movies have been made for several INTER calculations including the case illustrated in Figure 1-15. This form of presentation provides the viewer with a very graphic impression of the change in cavity shape as it erodes and also of variations in the local erosion rates which produce these shape changes. It also offers the possibility of combining computed results with experimental observations obtained using the pulsed X-ray system (described in Section 1.2.2) by superimposing computed cavity contours on the experimental X-ray movie to provide a pictorial comparison of predicted and observed cavity erosion.

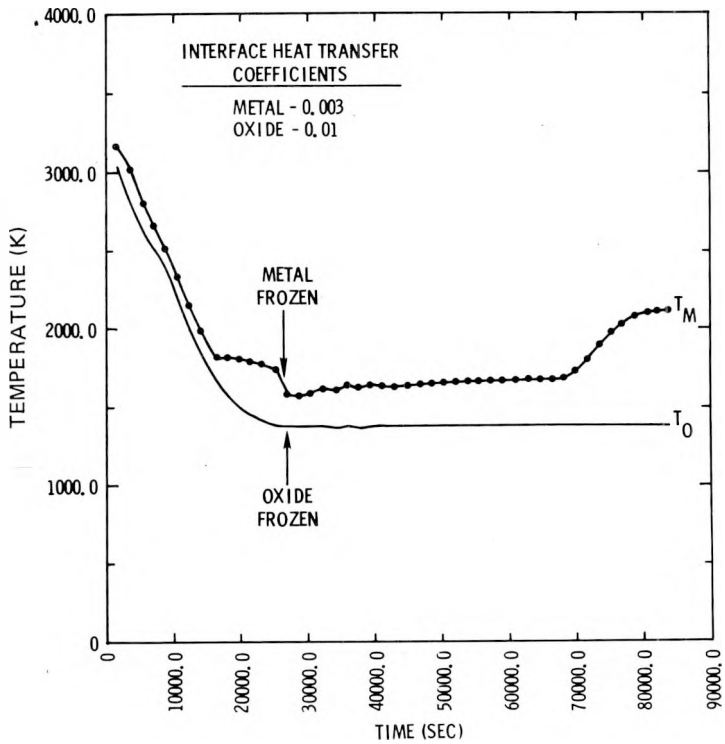

Figure 1-14. Sample Plot Showing Metal and Oxide Temperature Variations with Time for a Sample Reactor Problem Computation

Finally, work continued on the development of phenomenological models for fission product decay heat generation and core/concrete interface heat transfer. The latter is discussed in the next section.

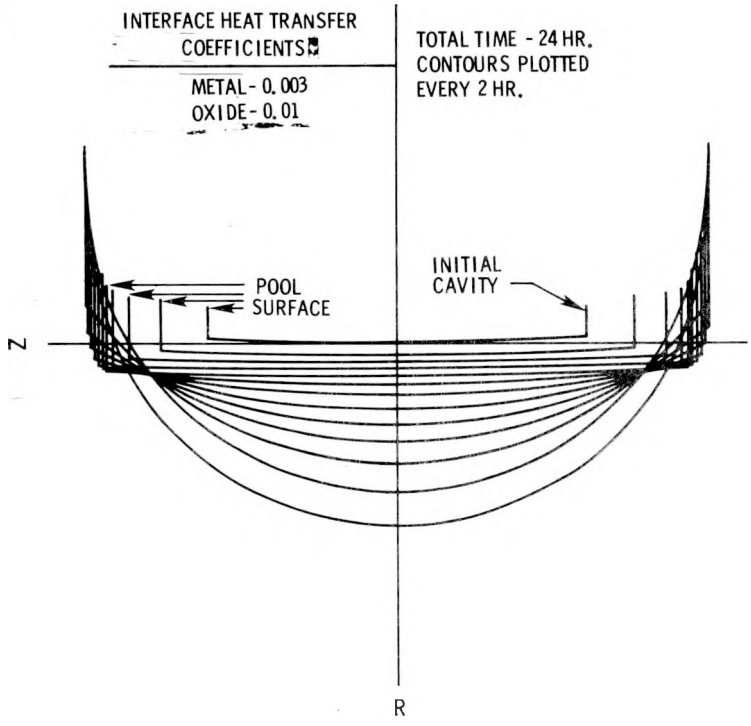

Figure 1-15. Sample Plot Showing Concrete Cavity Growth with Time Due to Concrete Erosion for a Sample Reactor Problem Computation

1.3.2 Interface Thermal-Hydraulics Study (R. D. Boyd, B. M. Bulmer, and D. O. Lee)

This study includes both analytical and experimental efforts and has the following objectives:

- To define the flow configurations at the melt/concrete interface, the conditions under which they exist, and the necessary transition criteria.
- To determine local heat and mass transfer across and along the interface as a function of interface configuration and local inclination angle, melt and concrete material properties, mass flux out of the concrete, and circulation with the melt.
- To provide results suitable for inclusion in CORCON.

Activities during the present quarter concentrated on the experimental portion of the study. Design drawings of the apparatus for the liquid-pool/vapor-film experiments were completed. Construction of the apparatus is presently scheduled to begin in mid-August.

The feasibility of investigating the interaction between an internally heated, boiling-liquid pool and a decomposing solid using simulant materials was explored. A preliminary experiment was performed in which a pool of ethyl alcohol in a dry ice crucible was heated internally to boiling using a microwave oven. Since the primary purpose of the test was a demonstration of the

feasibility of the experimental technique, experimental measurements were limited to pretest and posttest observations of the cavity shape. Qualitatively it appears that, for the conditions of the test, an internally heated, boiling liquid contained in a subliming solid crucible causes an initially cylindrical cavity to erode somewhat more in the radial (horizontal) direction than in the vertical direction (see Figure 1-16).

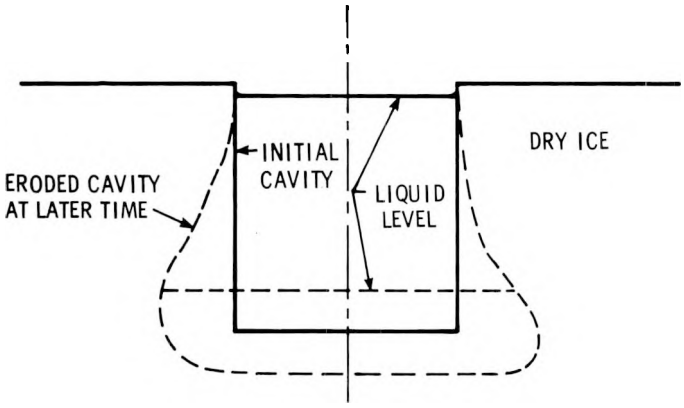

Figure 1-16. Schematic of Eroded Cavity Geometry Produced by the Interaction of Internally Heated, Boiling Alcohol with Dry Ice

References - Section 1

1. D. A. Powers, Molten Core-Concrete Interactions Project Description, 189 No. A-1019, Sandia Laboratories, Albuquerque, NM, October 1975.

2. D. A. Powers, D. A. Dahlgren, J. F. Muir, and W. B. Murfin, Exploratory Study of Molten Core Material/Concrete Interactions - July 1975 to March 1977, SAND77-2042, Sandia Laboratories, Albuquerque, NM, February 1978.

2. Steam Explosion Phenomena

2.1 Efficiency Scaling Studies (L. D. Buxton and W. B. Benedick)

2.1.1 Summary

The performance of 12 efficiency scaling experiments (alumina/iron) was reported previously.[1,2] Ten additional experiments have been performed this quarter. The important features of these are summarized in Table 2-I. Seven of the ten tests were attempts to eliminate the unknown natural triggering mechanism of the observed explosions while the other three tests were used to investigate the effect of pour rate and water temperature. Explosions were observed in 9 of the 10 tests. Both single and double explosions occurred. The explosions triggered spontaneously at seemingly random delay times from pour initiation. The most efficient explosion happened during a test with cold water using a high pour rate. The bottom of the interaction tank was blown out in that test and the efficiency of converting the thermal content of the melt into work was estimated to be nearly 1%. A very similar experiment but using boiling water was the only experiment to not yield an explosion.

The residue from Thermite test No. 9, which was described last quarter, has recently been subjected to further scanning electron microscopy. The debris appearance is very similar to that of the Corium simulants produced in the laboratory-scale explosions. The debris is quite different from the debris generated in a recent field-scale fragmentation test in which a Thermite-generated melt mixture was poured into sodium instead of water.[3]

2.1.2 Natural Trigger Elimination Tests

Thermite test No. 12, reported on last quarter,[2] was the first in a series of tests being performed to find some method of eliminating the unidentified trigger mechanism of the observed explosions. The natural trigger mechanism needs to be eliminated so that later efficiency scaling tests can use artificial triggers and thus allow control over the melt quantity poured before the explosion, also to allow more accurate explosion diagnostics by properly initializing high-speed recording equipment. Test No. 12 used a sandblasted interaction vessel because the presence of a rusted surface has been shown to enhance the probability of an explosion in large-scale aluminum tests.[4,5] As reported previously, sandblasting alone was not sufficient to inhibit the explosion in test No. 12. Therefore, a surface coating of grease was placed on the inside of the sandblasted tank top used as an interaction vessel in test No. 14. Grease coatings were shown to prevent initiation of explosions in some of the aluminum tests referred to above.[4,5]

TABLE 2-I

Summary of Important Features of Efficiency Scaling Experiments

Experiment Number	Thermite Mix Quantity (kg)	Water Quantity (kg)	Water Temperature (K)	Number of Explosions	Delay to First Explosion (s)	Minimum Efficiency (%)	Test Purpose	Remarks
13	13.6	400	369	2	1.48	0.26	Water temperature	Boiling water
14*	10.2	175	~300	1	0.41	0.08	Trigger elimination	Grease coating
15	13.6	840	~300	1	1.27	0.96	Pour rate	Tank bottom blew out
16*	10.2	175	~300	1	1.31	0.07	Trigger elimination	Epoxy coating
17	13.6	840	~300	2	0.41	0.05	Trigger elimination	Single screen, 6 in. down
18	13.6	840	~300	1	2.78	0.21	Trigger elimination	Dual screens 12 and 18 in. down
19	13.6	840	~300	2	0.55	0.10	Trigger elimination	Single screen, water level
20	13.6	840	~300	2	1.63	0.36	Trigger elimination	Splatter plate
21	13.0	560	~300	2	1.27	0.18	Trigger elimination	1/2 in. thick melt plug
22	12.5	780	366	0	-	-	Pour rate, water temperature	Long heaters, boiling water

*Used inverted tank top as interaction vessel.

The physical setup for test No. 14 was essentially the same as the one used for No. 12, with the inverted tank top being suspended by bolts above the regular interaction tank and the melt generator suspended above that. About 175 kg of water were in the inverted lid for test No. 14 and 10.2 kg of the standard aluminum/iron-oxide mixture were put in the melt generator. The melt plug failed about 10 seconds after the Thermite mix was ignited. There was a single explosion about 0.4 second later. The efficiency estimate of 0.08% (of the melt's energy appearing as work) for this explosion was based on the amount of honeycomb crushed and the height which the water and debris were blown into the air. No estimate was made of the energy expended in bending the 19 mm diameter tie bolts, but it was probably negligible.

The surface of the interaction vessel was also altered for test No. 16. For that experiment, the tank cover was sandblasted and the interior was then painted with a heat-cured epoxy paint. The physical setup was identical to that used in No. 14 except a 6.4 mm thick steel plate was used for the generator melt plug instead of the 9.5 mm thick aluminum plate used previously. The diameter of the pour hole which is covered by the melt plug was left at 51 mm. The melt plug materials was changed to eliminate the possibility of molten aluminum (which is known to be highly explosive in water) becoming directly involved in the observed explosions. There was no radical change in the time from reaction ignition to melt plug failure as a result of this modification, but these time intervals have varied considerably without changing the generator design. The higher melting point of the plug was at least partially offset by the use of a thinner plug.

The epoxy paint method of surface preparation also failed to inhibit explosions. There was a single explosion in test No. 16 about 1.31 seconds after the melt plug failed. The estimated efficiency of the explosion was slightly lower than for No. 14, but some of the bolts holding the tank lid to the tank were broken completely in half by the explosion, causing the load to be poorly transmitted to the crushable honeycomb. The molten mixture which fell into the tank top after the explosion had blown the water out did almost no damage to the paint, merely scorching it a little. The surface was still very smooth and the debris slid out easily, without sticking. Consequently, the explosion is not believed to be the result of local failure of the paint coating.

Since the surface preparation techniques similar to those which inhibit aluminum/water explosions were not successful for the Thermite-generated molten aluminum-oxide and iron mixtures, a different approach was tried, based on the assumption that slower pour rates would be less conducive to explosions. The idea was suggested by the results of aluminum/water studies[4,5] and also by the fact that only fragmentation was seen for the first four experiments in the current efficiency scaling test series.[1,2] The pour rates were lower for those experiments than for the later experiments.

Test No. 17 was the first trial of methods to break up the melt stream. A screen made from two overlapping pieces of expanded metal mesh was placed in the large interaction tank about

150 mm down from the top of the tank and parallel to the water surface. The mesh configuration yielded a pattern of diamond-shaped holes about 12 mm wide and 25 mm tall. The tank was completely filled with 840 kg of water. The melt generator initially contained 13.6 kg of mixed aluminum and ferrous oxide powders.

Two explosions occurred in test No. 17, both of about the same magnitude. The first one was at 0.41 seconds and the second at 0.98 seconds after plug failure. The pour continued for about 3 more seconds but there were no more explosions even though only about 200 kg of the original 840 kg of water was blown out. The screen (which was not tied down to its supports) was not blown out of the tank, which suggests that the explosions might have taken place above the screen.

Thermite test No. 18 was idential to No.17 except two screen arrays were used, one 300 mm and one 450 mm down from the top of the tank. There was only a single explosion in this experiment, a large one at 2.78 seconds after pour initiation. Only about half of the water was blown out of the tank. Although the explosion was large, with an estimated efficiency of 0.21%, there still was not much damage to the screens. The top screen was bent downward a little in the middle, indicating again that perhaps the explosion occurred above the screen.

Test No. 19 was the final attempt at trigger elimination by using a screen to break up the melt. A single screen was used as in No. 17, but this time it was placed flush with the water surface so that the melt would be forced to go through the screen and be broken up before it could participate in an explosion. Otherwise, the setup was like those used in the previous two tests. There were two explosions this time, one at 0.55 seconds and one at 1.22 seconds after pour initiation. The second explosion was the strongest but together the efficiency was still only 0.10%. The screen was blown out this time, however, apparently by the second explosion.

Since the screen method of breaking up the melt failed to eliminate the spontaneous initiation of explosions in the three previous experiments, a different scheme was tried in test No. 20. A 25 mm thick steel plate about 300 mm square was suspended by wire ropes so that it hung in the water just under the surface and served as a "splatter" plate. This trial method of trigger elimination also failed. Two explosions occurred, a strong one at 1.63 seconds after melt plug failure and a very weak one 1.7 seconds later. The efficiency estimate of 0.36% is based only on the melt estimated to be present at the time of the first explosion. There was some permanent plastic deformation of the 9.5 mm thick interaction vessel wall in this test and the efficiency estimate included the work required to do that damage. It is interesting to note that the final water level was above the major bulge point in the tank wall. The explosion apparently occurred in the bottom of the tank but a lot of the water still was not blown out. Since the bulge is primarily on one side of the tank, perhaps the explosion was on that side and that is the reason some water remained.

The final trigger elimination method attempted during the quarter involved a thicker steel melt plug (12 mm). The intent was to delay the beginning of the pour to give additional time for any excess gas which might be present in the melt to escape before it contacted the water. Gas release from the melt interior is suspected to be intimately involved in the fragmentation process of the explosion propagation and might possibly also be involved in triggering the large-scale explosions.

The interaction tank contained about 560 kg of cold water for test No. 21. Only 13.0 kg of Thermite mix would fit in the generator since the insulation layer was made a little thicker for this test. The thicker melt plug did delay the pour initiation as expected. Failure of the plug did not occur until 31 seconds after ignition of the reaction, about twice the normal holding time. Unfortunately, this had no discernible effect on the experiment. Two explosions occurred, the first at 1.27 seconds and the second at 2.06 seconds after plug failure. Nearly all of the water was blown out of the tank and the estimated efficiency was 0.18%.

2.1.3 Water Temperature Effect Tests

Two experiments in which the melt was poured into warm and hot water were reported last quarter.[2] Two additional tests studying the effect of water temperature were performed this quarter. The first of these, test No. 13, was essentially identical to the hot water experiment No. 11 except the water temperature was even higher. In test No. 11, the heaters were removed from the tank several minutes before igniting the melt. In No. 13 the heaters were sacrificed and left in, with the water visibly boiling just before melt ignition. For safety purposes, the heater current was turned off about 30 seconds before the melt contacted the water. This allowed some slight cooling of the water, but the water could be assumed to be saturated for all practical purposes. The tank initially contained about 400 kg of the boiling water, only slightly more than in test No. 11.

After melt plug failure and melt/water contact occurred, an orange cloud started to form as has been observed in some of the other tests, particularly those with warm and hot water. In this test, however, unlike No. 11, there was a very loud explosion at 1.48 seconds after melt plug failure, followed by a very small one about one-half second later. The heater elements and holding brackets were all blown from the tank. It appears that one of the heaters was severely bent during the explosion and then scraped along the bracket which supports the melt generator. The efficiency estimate of 0.26% was based only on the melt quantity estimated to have poured before the first explosion since the second explosion was very weak. It should be noted that this test produced the second most efficient explosion observed up to that time, which strongly indicates that the use of saturated water instead of highly subcooled water has little if any effect on the efficiency of the explosions.

In the other boiling water test performed this quarter, No. 22, a full tank of water was used instead of half a tank. A set of rod heaters which reached the tank bottom was used to ensure that the water was uniformly heated. As in No. 13, the heaters were left in the tank but had their power shut off about 30 seconds before the melt plug failed. When the pour began there appeared to be a vigorous interaction at the water surface, accompanied by ejection of material, but there was no explosion. The melt did fragment considerably. The fact that no explosion occurred indicates that water temperature may have an effect on the spontaneous initiation of large-scale explosions. No definite statements can be made, however, on the basis of a single test. The test will be repeated as closely as possible to see if it is reproducible.

2.1.4 Pour Rate Effect Tests

Most of the efficiency scaling tests which have produced explosions have had a pour stream diameter of 50 mm. Two of the tests performed this quarter used a 76 mm diameter pour hole to try to increase the rate of contact between the melt and the water from the average 3 kg/s value achieved with the 50 mm hole. Thermite test No. 22, discussed in Section 2.3 above, was one of those tests. As indicated, there was no explosion in that test. The average pour rate for test No. 22 was determined from the films to be about 5 kg/s but the melt plug only opened to an average diameter of about 63 mm.

The other test designed to investigate the effect of pour rate was No. 15. Like test No. 22, it was performed with a full tank of water. This was the first experiment for which the melt plug was 6.4 mm thick steel instead of 9.5 mm aluminum. It covered a pour opening which was about 76 mm in diameter. In this test there was a single explosion 1.27 seconds after the melt plug failed. The explosion appeared to blow the melt remaining in the generator out the top vent pipe of the generator, so the total pour could not be timed to get an average pour rate. Posttest examination showed that the melt plug only opened to an average 56 mm diameter; thus a pour rate of 4 kg/s before the explosion was assumed in the efficiency analysis.

Although the intended very large pour rate was apparently not achieved in test No. 15, this experiment still produced the most efficient explosion observed to date. The estimated thermal energy to work conversion efficiency for this test was 0.96%. The honeycomb pads under the tank were crushed to the maximum extent possible, the generator framework was severely bent, the vertical interaction tank walls were plastically deformed over a height of about 0.5 m with a maximum bulge of 1.25% strain, and the bottom of the tank was cracked open and bent outward. The water and debris were accelerated upward for some time before the bottom blew out since no significant amount of water poured out the bottom. Using the known honeycomb crush strength and the estimated yield and ultimate tensile strengths of the tank walls, it has been determined that the maximum steam pressure inside the tank was most likely between 5 and 10 MPa. Higher pressures would probably have caused catastrophic failure of the tank wall. The tank bottom probably failed first because it was weakened somewhat by the hole for the drain pipe.

2.1.5 Debris Analysis

It was previously reported that the debris from test No. 9 had been examined by scanning electron microscopy in a preliminary fashion.[2] That analysis has been completed, and some other debris produced in a field-scale fragmentation test in which the same type of melt was dropped into liquid sodium has also been studied.[3] Figure 2-1 is a pair of scanning electron micrographs of two representative samples of finely divided debris recovered from test No. 9. The white bar in the lower right corner of each represents 500 microns. Both spheroids and "mossy" material with highly irregular surfaces are seen. One sphere is seen in the middle right side of the left micrograph which has apparently broken and ejected a stream of material. The surface area of the mossy particulate is obviously much higher than would be determined for perfect spheres of equivalent diameter. The debris is seen to be quite similar to the Corium debris pictured in Figure B-32 of Reference 6, especially the debris from 9-102-1.

Figure 2-2 is a pair of scanning electron micrographs of representative debris from the interaction of a Thermite-generated aluminum-oxide/iron melt with liquid sodium. The overall particle sizes of this sample are about the same as for the debris shown in Figure 2-1 but the particle morphology is quite different. Most of the fragmentation test No. 1 debris seems to be either spheroidal or "chunky." The "mossy" type of particle with high surface-area-to-volume ratio seen in the Thermite test No. 9 debris is not seen in the fragmentation test No. 1 debris. This difference is attributed to the fact that there was a large coherent explosion in Thermite test No. 9 and only a few small incoherent pressure generating events in fragmentation experiment No. 1.

Figures 2-3 and 2-4 show cross sections of representative debris from the Thermite No. 9 and fragmentation No. 1 tests, respectively. In each case (A) is a standard scanning electron micrograph, (B) is an elemental scan for iron over the same area, and (C) is an elemental scan for aluminum. In Figure 2-3 it can be seen that the Thermite test particles sometimes contain predominantly iron and sometimes aluminum, yet there are many agglomerates containing both metals. According to X-ray debris analysis results, the iron is probably in the form of iron metal and the aluminum is in the form of an oxide, alumina. The agglomerates seem to be the mossy particulate with the high surface-area-to-volume ratios and are believed to be formed from tiny particles created during the explosion which have stuck together. The smallest particles which make up the agglomerates seem to be only a few microns in diameter.

Almost no agglomerates appear in the fragmentation test No. 1 debris shown in Figure 2-4. Most of the debris seems to be either iron or alumina. Most of the chunky pieces of debris with sharp edges are alumina which probably suffered thermal stress fracture after solidification, but some speroidal alumina debris is also seen which indicates that at least some of the alumina fragmented while it was still molten. Most of the iron apparently fragmented while molten since there do not appear to be any iron particles with sharp edges.

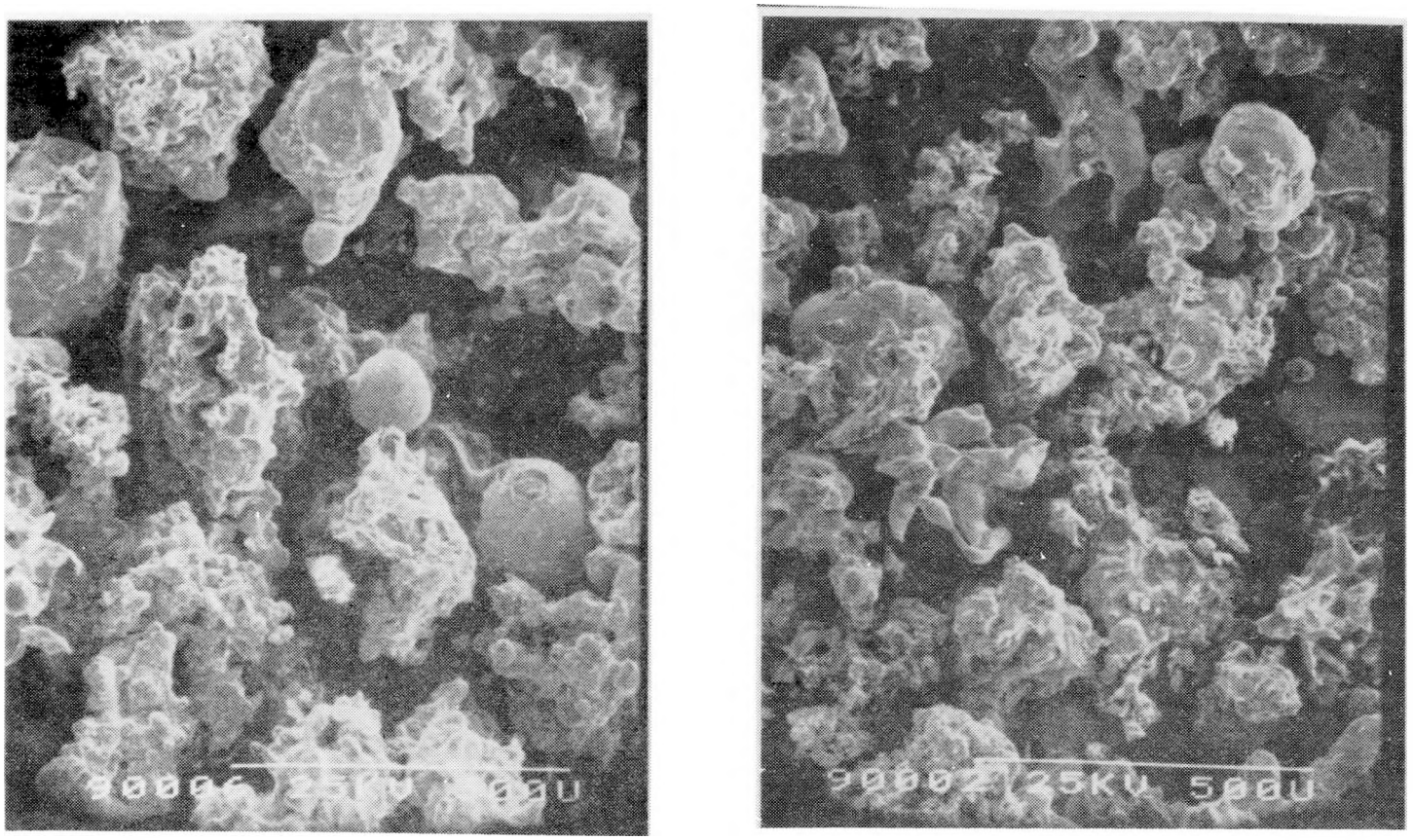

-50, +100 Cut

Figure 2-1. Scanning Electron Micrographs of Debris From Thermite Test No. 9

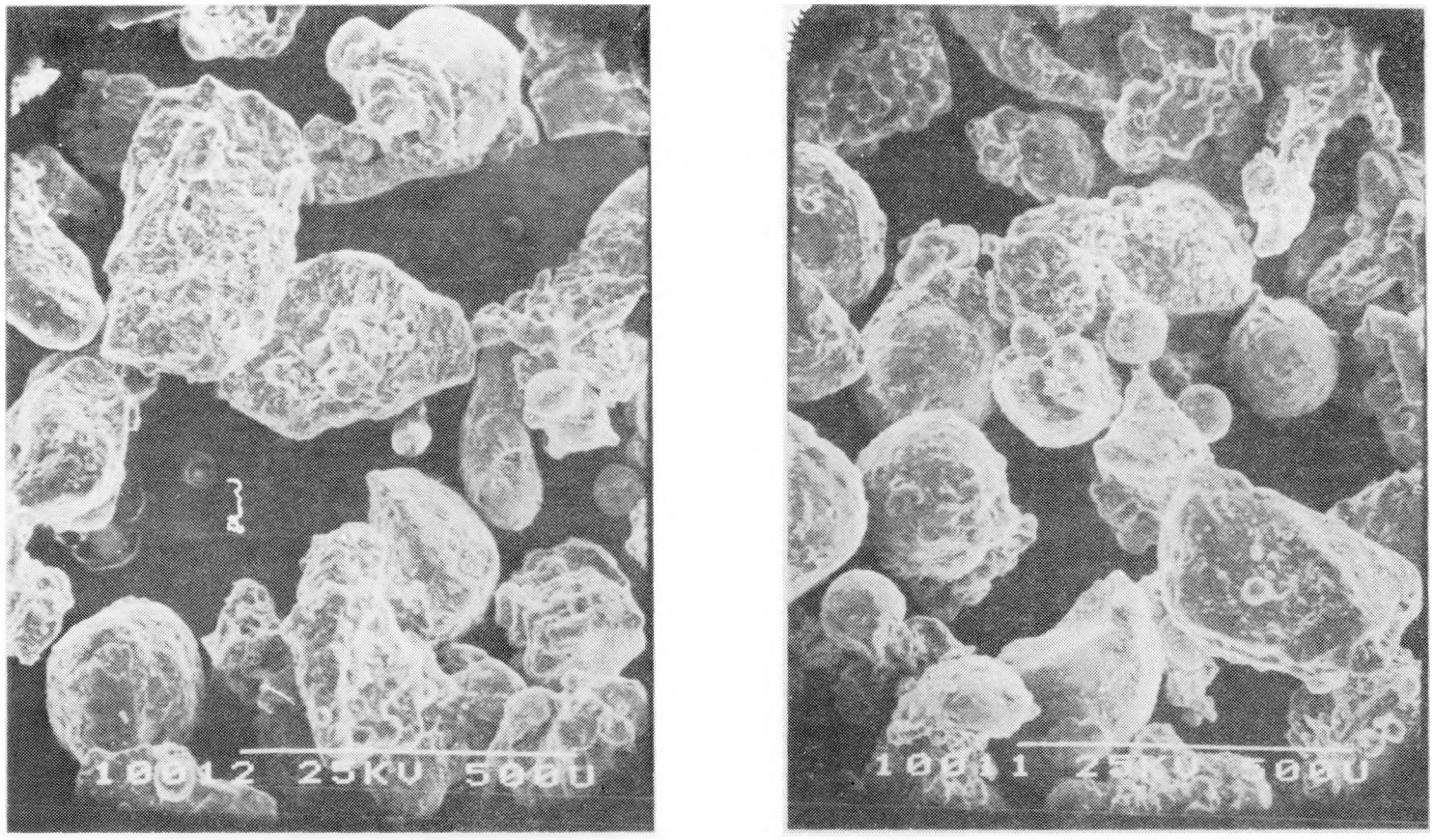

-60, +100 Cut

Figure 2-2. Scanning Electron Micrographs of Debris From Fragmentation Test No. 1

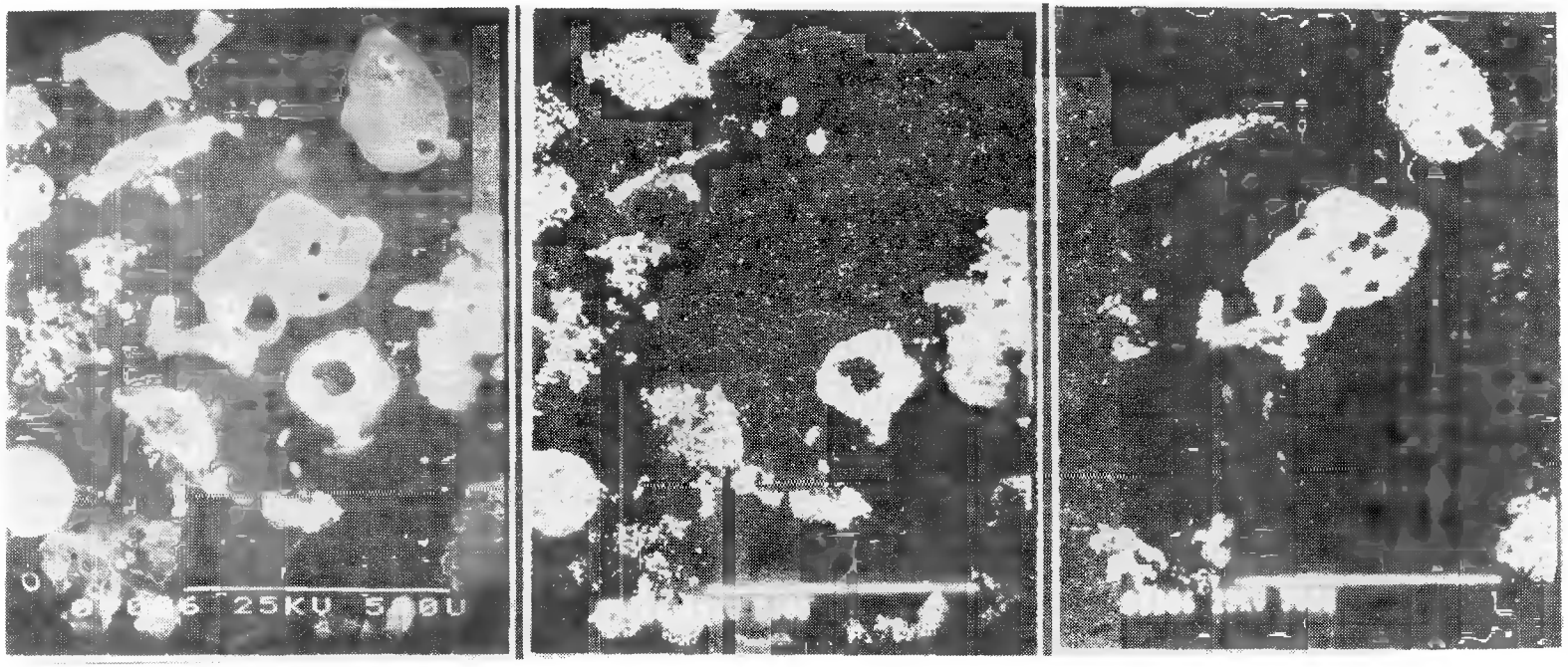

(A)
Scanning Electron
Micrograph

(B)
Iron
Scan

(C)
Aluminum
Scan

Sectioned Debris

Figure 2-3. SEM and Elemental Scans of Cross-Sectioned Debris From Thermite Test No. 9

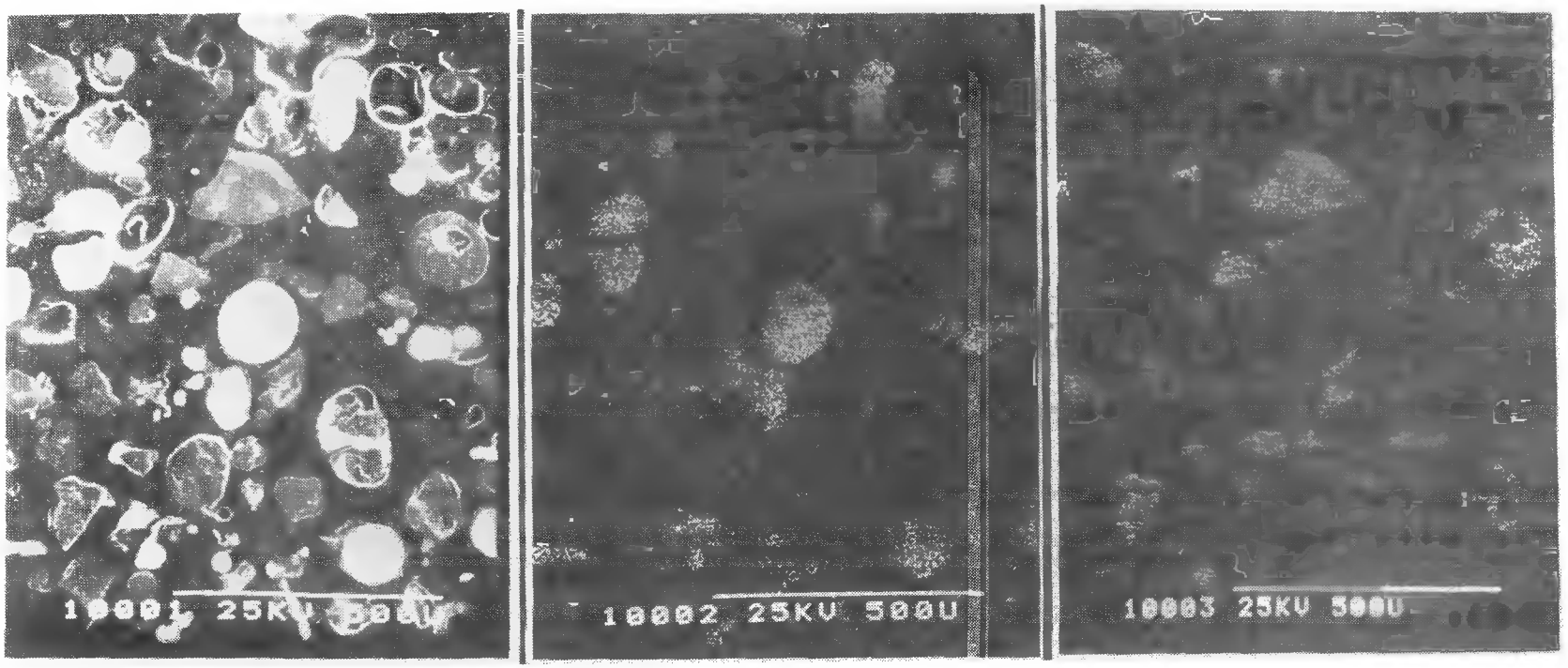

(A)
Scanning Electron
Micrograph

(B)
Iron
Scan

(C)
Aluminum
Scan

Sectioned Debris

Figure 2-4. SEM and Elemental Scans of Cross-Sectioned Debris From Fragmentation Test No. 1

The Thermite test No. 9 debris seems to be more porous than the fragmentation test No. 1 debris. This observation is consistent with gas release being the principal mechanism for the fragmentation during a large coherent explosion. In both debris samples most of the porosity is seen in the alumina particulate. This observation agrees with laboratory observations that more oxidic forms of Corium simulants explode more violently, which is also believed to be explained by the impulse-initiated gas release theory of fragmentation.[6]

2.1.6 Efficiency Scaling Discussion

Although none of the methods which have been tried have been successful in eliminating the natural trigger of the observed explosions, some scaling information is available from the experiments performed. Figure 2-5 is a plot of the explosion efficiency versus the amount of melt estimated to have poured before the spontaneous explosion for all of the efficiency scaling experiment explosions to date. The amounts shown represent between 15 and 70% of the melt actually available in the generator for any given experiment. The quantity estimates were based on the timing obtained from the films, pour rates determined from timing complete pours, and pour hole diameter information. As indicated, the data are quite scattered and no clear correlation exists even if fairly wide error limits are assumed. The trend appears to be toward more efficient explosions as the melt quantity increases but there simply is not a sufficient amount of data for the larger quantities to make a definitive statement. The search for a method of eliminating the natural trigger to allow more large-melt-quantity data will be continued.

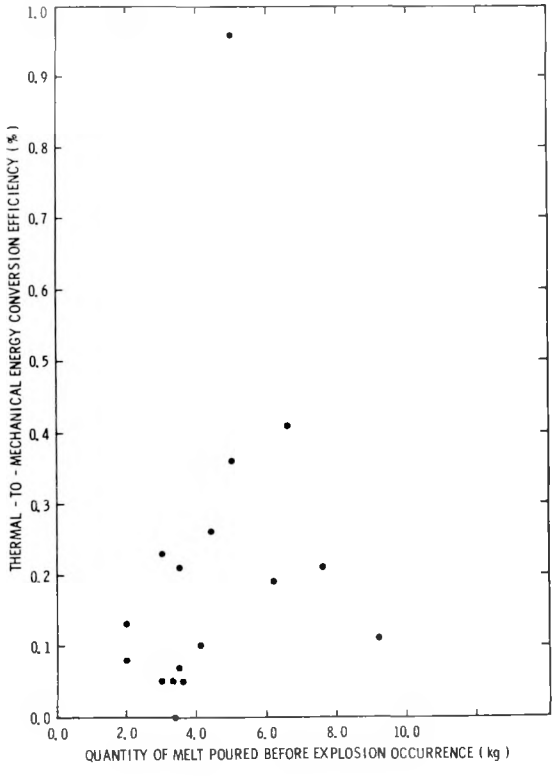

Figure 2-5. Efficiency Scaling Data for Thermite-5 Through Thermite-21

2.2 Triggering Studies (L. S. Nelson)

2.2.1 Summary

Most of the effort this quarter was devoted to investigating the effect of water temperature on fully oxidic Corium-E simulant and hematite (Fe_2O_3) melts. The maximum water temperatures at which fragmentation occurred lay in the range from 318 to 329 K for the Corium-E simulant and 338 to 343 K for the molten hematite.

Several theory-checking experiments were performed using through-the-hearth pulses; also, iron oxides of low initial oxygen content were studied. The experiments performed this quarter are summarized in Table 2-II.

2.2.2 Effect of Water Temperature

During this quarter, a system for controlling water temperature was set into operation. This system uses circulating cold and hot water loops with a proportioning valve to blend the two streams in a constant temperature flow. The system is designed to operate at water temperatures between 273 and 373 K. Initially the water was circulated directly from this conditioning system through the interaction chamber with a portion of this water used for the flooding. With this system, five experiments were performed with fully oxidic Corium-E simulant (61.5 at. % initial oxygen) at water temperatures between 315 and 351 K; explosions could not be induced with bridgewire impulses. With molten hematite 10 experiments were performed using bridgewire initiation at water temperatures between 310 and 364 K and 6 with through-the-hearth induced pressure pulses at water temperatures between 309 and 349 K. As shown in Table 2-II, the reproducibility was poor, but explosions could be induced in hematite with bridgewires at water temperatures up to about 338 K. Explosions could not be induced by the through-the-hearth pulses in the water temperature range studied.

The poor reproducibility with the hematite, and the failure of the fully oxidic Corium-E simulant to explode, was attributed to the presence of many easily visible bubbles ($\approx$ 1 mm in diameter) produced in the flooding water by the direct circulation system. These were probably air bubbles generated by the pumps in the system and could be expected to affect both the boiling phenomena and the transmission of the bridgewire pulses through the water. To remedy the situation, water from the direct circulation system was instead passed through a heat exchanger submerged in the flooding water for the later experiments. This was made of about 4 m of 6.4 mm OD aluminum tubing, bent sinusoidally and introduced into the outer chamber of the interaction vessel. The tubing was placed near the outer wall of the chamber to minimize its effect on flooding and on the transmission and recording of pressure transients. Aluminum tubing was selected because of its transparency to the flash X-ray beams used for imaging of the hot liquid.

TABLE 2-II

Summary of Results of Triggering Experiments

Starting Material	Experiment No.	Sample Weight (g)	Water Temp. (K)	Water Amount (l)	Melt/Atm. Pressure (MPa)	Melt Temp. (K)	Transient Generation	Delay Time (sec)	Flash X-Ray	High Speed Photos	Remarks
FeOx (50 at. % Oxygen)[a]	10-68-1	14.90	298	1.5	Ar/0.083	1893	BW	0.228	None	400-foot	No explosion; some coarse fragmentation.
FeOx (50 at. % Oxygen)[a]	10-71-2	14.89	299	1.5		1862	BW	0.174	None	400-foot	No explosion; some coarse fragmentation.
Fe_2O_3(60 at. % Oxygen)	10-66-3	15.2	311	1.5		- [e]	Through H Undercut	- [b]	None	400-foot	Sleeve did not rise; no flooding.
Fe_2O_3(60 at. % Oxygen)	10-67-1	14.96	309	1.5		- [e]	Through H Undercut	- [b]	None	400-foot	Sleeve did not rise; no flooding.
	10-70-1[c]	15.00	329	Depth[c] 7.5 cm		2103	BW	0.227	Two-pulse	400-foot	Coarse fragmentation. Many bubbles at interaction time.
	10-71-1[c]	14.99	323			2049		0.25	Two-pulse	None	Two-stage explosion; 0.52 MPa peak pressure.
	10-72-1[c]	14.97	332			2156		0.216		400-foot	Very rigorous 2-stage explosion; 3.64 Mpa peak pressure. Many bubbles at interaction time.
	10-73-1[c]	15.01	334			2038		0.193	Three-pulse		Many bubbles in water at interaction time. A few fragments; no explosion.
	10-73-2[c]	15.00	338			2073		0.200			Mild explosion, coarse breakup. Many bubbles in water.
	10-74-1[c]	15.01	364			2054		0.242			No explosion; bubbles in water. A few fragments. Water murky.
	10-74-2[c]	14.97	357			1984		0.252			No explosion; a few coarse fragments.
	10-75-1[c]	15.07	354			2049		0.228			No explosion; a few coarse fragments. Some bubbles in water.
	10-75-2[c]	15.00	340			- [e]		0.243			Many bubbles in water. No explosion; some coarse fragmentation.
	10-76-1[c]	15.10	336			2038		0.223			Same as for 10-75-2.
	10-80-2[c]	15.02	349			- [e]	Through H Flex	0.25		Mostly opaque	Many bubbles in water. Could not detect trigger pulse. No explosion.
	10-81-1[c]	15.01	328			- [e]		0.25		Mostly opaque	Many bubbles in water. Could not detect trigger pulse. No explosion.
	10-82-1[c]	15.04	310			- [e]		0.25	Two-pulse	Clear image No bubbles	Trigger possibly visible. Some coarse fragmentation; no explosion.
	10-82-2[c]	15.01	310			1984		0.224	Three-pulse	Clear image No bubbles	Can see application of trigger. Melt shakes mildly, but does not explode.
	10-84-1[d]	14.97	324	1.5 cm		1929	BW	0.137		Mostly opaque	Many large bubbles in the water. No explosion.
	10-84-2[d]	14.95	298			-		0.25		Opaque then clears	Trigger not detected on film. No explosion.
	10-85-1[d]	15.00	299			2014		0.264		Partly opaque	Moderate one-stage explosion; coarse fragmentation.
	10-85-2[d]	14.98	299			2042		0.282		Partly opaque	Two-stage explosion; peak pressure of 0.3 MPa.
	10-86-1[d]	14.97	317			2068		0.268		Partly opaque	Modest explosion; coarse fragmentation; mostly speroidal.
	10-86-2[d]	14.97	327			- [e]		0.205		Clear image	Modest 1-stage explosion; coarse fragmen
	10-87-1[d]	14.70	336			1965		0.257		Clear image	One-stage explosion producing very coarse speroidal debris.
	10-87-2[d]	14.98	349			2042		0.207		Moderately clear image	No explosion. One-piece sample with single horizontal void.
	10-87-3[d]	12.91	352			2080		0.316		Moderately clear image	No explosion. One-piece sample; no void.
	10-88-1[d]	15.02	364			1995		0.256	None	Moderately clear image	No explosion. One-piece sample with a few globules.
	10-88-2[d]	15.02	330			1948		0.293	Three-pulse	Clear image	One-stage explosion with fairly fine debris
	10-89-1[d]	15.00	340			2073		0.251		Clear image	One-stage explosion with coarse debris.
	10-89-2[d]	14.97	353			1912		0.216		Moderately clear image	No explosion. One-piece sample.
	10-89-3[d]	15.00	343			2007		0.254		Clear image	One-stage explosion with coarse debris.
Corium-E (61.5 at. % Oxygen)	10-77-1[c]	14.84	315	Depth[c] 7.5 cm		1979		(0.25)[c]		Defective exposure	One-piece sample; no sign of explosion.
	10-77-2[c]	14.93	313			2026		0.239		Mostly opaque	No explosion. Many bubbles in water.
	10-78-1[c]	14.92	322			2014		0.225		Mostly opaque	No explosion. Many bubbles in water.
	10-79-1[c]	15.07	331			2007		0.220		Mostly opaque	No explosion. Many bubbles in water.
	10-80-1[c]	14.94	351			- [e]		0.246		Mostly opaque	No explosion. Many bubbles in water.
	10-90-1[d]	14.67	299	1.5 cm		2054		0.232		Clear image	Modest explosion with coarse debris.
	10-90-2[d]	15.05	316			- [e]		0.232		Clear image	Rigorous 2-stage explosion; 2nd stage in 3 parts; 1.12 MPa peak pressure.
	10-91-1[d]	15.05	329			2005		0.214		Clear image	No explosion.
	10-91-2[d]	15.07	318			2005		0.217		Fair image	One-stage explosion; coarse debris.

[a] Made from magnetite (Fe_3O_4) and iron powder.

[b] Sleeve failed to rise properly

[c] Used direct circulation water heating system.

[d] Used aluminum tubing heat exchanger in outer chamber for water heating.

[e] Films were bad; delay time was taken from instrumental setting.

Use of the heat exchanger eliminated the bubbles in the water, and the effect on the experiments was discernible. With the Corium-E simulant, four experiments suggested a maximum water temperature at which fragmentation occurred lying in the range from 318 - 329 K while, in the molten hematite, the maximum temperature reached was between 338 and 343 K. Further experiments are planned with the Corium-E simulant to determine the temperature range more precisely.

2.2.3 Theory-Checking Experiments

As a continuation of the attempts to use projectile-generated, through-the-hearth pulses to initiate interactions as described in previous quarterly reports, two experiments were performed with molten hematite using an undercut hearth constructed as shown in Figure 2-6. The purpose of the undercutting was to obtain a rigid physical contact between the melt and the hearth to ensure transmission of the pressure pulse into the melt. Explosions were not triggered with this configuration, even though the delay times most likely to produce vigorous explosions (0.2 to 0.3 sec) were used.

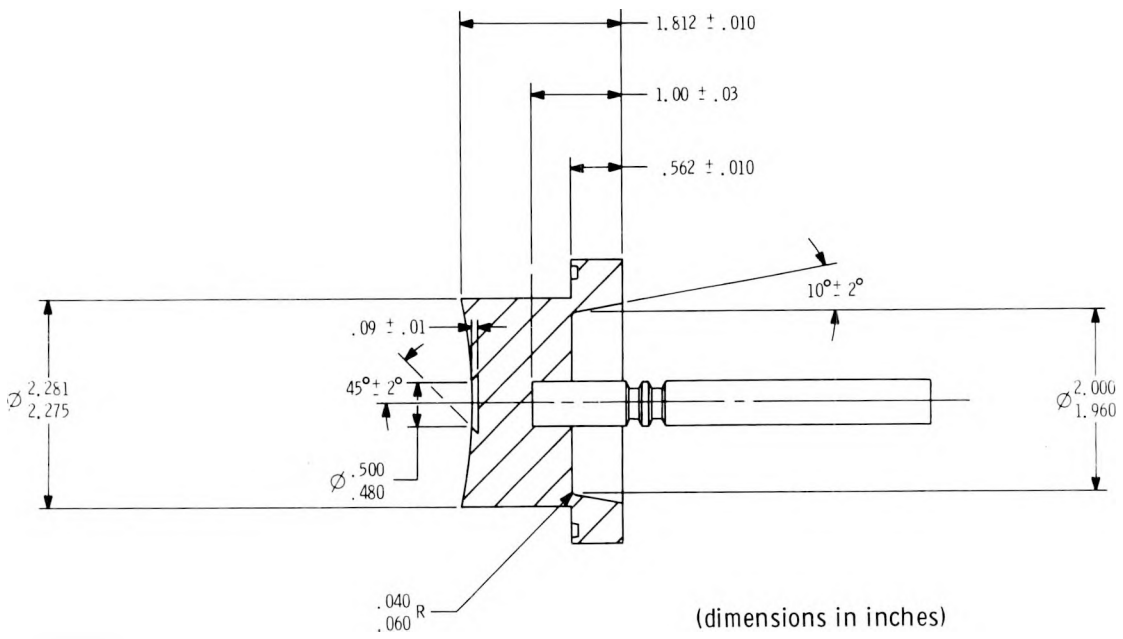

Figure 2-6. Cross Section of Undercut Hearth Designed for Through-the-Hearth Pulse Experiments

Studies of the effect of initial oxygen content on the explosive nature of molten iron oxides were continued. Earlier results were shown in Figure 14 of the previous quarterly report.[2] Two further experiments were performed with the composition FeO, corresponding to 50 at. % initial oxygen. The starting materials were pellets prepared from a mixture of magnetite (Fe_3O_4) and iron powder. The most explosive conditions were used, but no explosive interactions could be

induced. Figure 14 in the last quarterly has been modified to include these two data points at the zero pressure, 50 at. % coordinates (the origin), as shown in Figure 2-7.

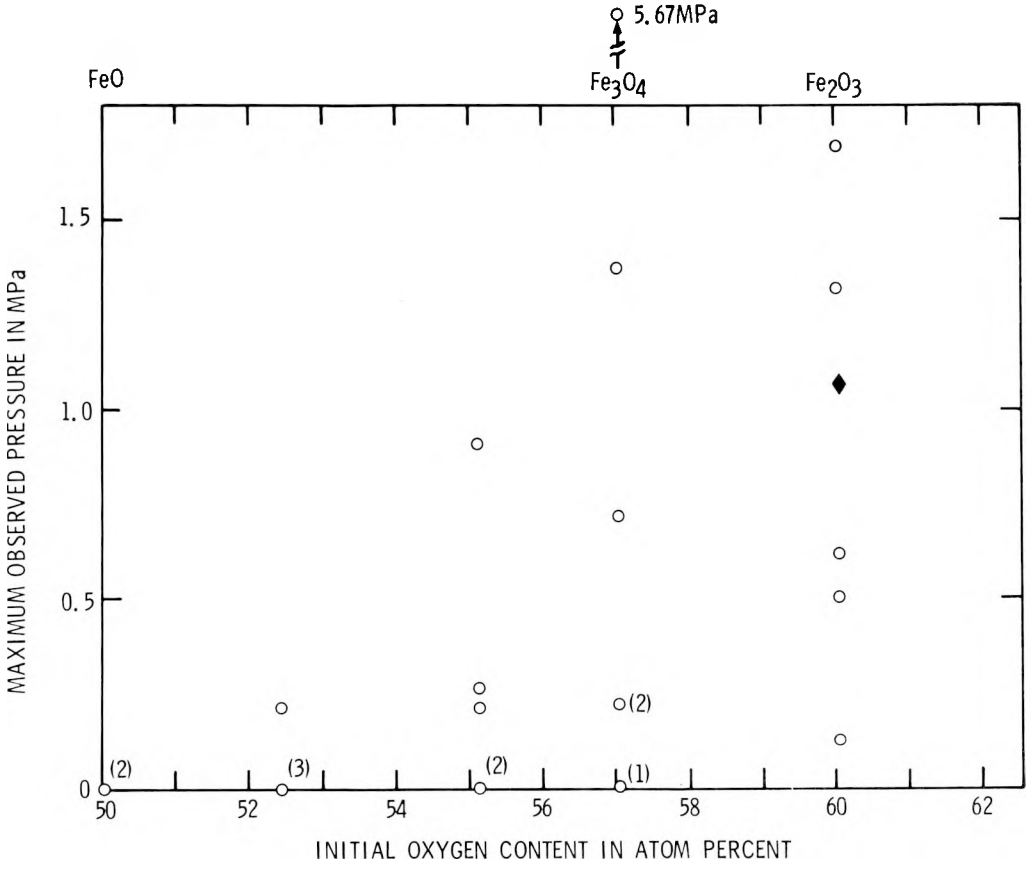

Figure 2-7. Revised Figure 14 From January - March 1978 Quarterly Report. Additions include two points at the origin (new work this quarter) and other points on the abscissa indicating experiments in which explosive interactions did not occur. Numbers in parentheses indicate number of times the experiments were repeated. All experiments were performed at a chamber pressure of 0.083 MPa, except for the shaded diamond which was performed at a chamber pressure of 0.3 MPa.

2.2.4 Debris Analyses

Neutron activation analysis for oxygen content of the debris from steam explosions was begun this quarter. Sieve fractions of exploded Corium-E simulant debris (9-119-1; 10-20-2) were studied. Also, standard samples of hematite and magnetite, and iron oxide compositions which had exploded vigorously (10-40-1; peak pressure, 1.37 MPa) and modestly (9-149-1; peak pressure, 0.14 MPa) were studied as retrieved. Also, two exploded iron oxide samples from this group (10-40-1; 9-149-1) were analyzed by wet chemistry. The results are shown in Table 2-III.

TABLE 2-III

Analyses of Corium-E Simulant and Iron Oxide Debris for Oxygen Content

Analytic Technique	Experiment No.	Starting Material	Initial Oxygen Content (wt %)	Sample Condition	Final Oxygen Content as Analyzed (wt %)	Remarks
Neutron activation*	10-40-1	(Fe_2O_3 + Fe)	27.6	As retrieved	21.9 ± 1.1	
Neutron activation	9-149-1	Fe_2O_3	30.1	As retrieved	21.4 ± 1.1	
Neutron activation	Standard	Fe_3O_4	27.6	Powder	27.4 ± 1.4	
Neutron activation	Standard	Fe_2O_3	30.1	Powder	29.7 ± 1.5	
Neutron activation	10-20-2	1.00 Corium-E	24.59	Sieved, 0-45 μm	21.0 ± 1.1	
Neutron activation	10-20-2	1.00 Corium-E	24.59	Sieved, 45-75 μm	20.9 ± 1.0	
Neutron activation	10-20-2	1.00 Corium-E	24.59	Sieved, 75-150 μm	20.4 ± 1.0	
Neutron activation	10-20-2	1.00 Corium-E	24.59	Sieved, 150-180 μm	19.5 ± 1.0	
Neutron activation	10-20-2	1.00 Corium-E	24.59	Sieved, 180-250 μm	17.9 ± 0.9	
Neutron activation	10-20-2	1.00 Corium-E	24.59	Sieved, 250-425 μm	18.2 ± 0.9	
Neutron activation	10-20-2	1.00 Corium-E	24.59	Sieved, 425-850 μm	18.3 ± 0.9	
Neutron activation	10-20-2	1.00 Corium-E	24.59	Sieved, > 850 μm	19.1 ± 1.0	
Neutron activation	9-119-1	1.00 Corium-E	24.59	Sieved, 750-150 μm	20.2 ± 1.0	
Wet chemistry	10-40-1	(Fe_2O_3 + Fe)	27.6	As retrieved	23.9	Run No. 1
Wet chemistry	10-40-1	(Fe_2O_3 + Fe)	27.6	As retrieved	24.7	Run No. 2
Wet chemistry	9-149-1	Fe_2O_3	30.1	As retrieved	25.5	Run No. 1
Wet chemistry	9-149-1	Fe_2O_3	30.1	As retrieved	25.7	Run No. 2

*Fe_2O_3, Fe_2O_3 - ZrO_2 mixtures and Fe_2O_3 - UO_2 mixtures used for standards. Zr causes low results for oxygen; U high results. Stated uncertainties are 2σ based on scatter of 5 standards: Valid if U < 35 wt % and Zr < 15 wt %.

It should be noted that (a) there is a difference of 2 to 4 wt % between the wet chemical and neutron activation analyses for oxygen in the two comparable iron oxide debris samples (10-40-1 and 9-149-1), and (b) there seems to be a trend toward higher oxygen contents at both the larger and smaller particle sizes in the fully oxidic Corium-E simulant debris. Both effects require further study.

X-ray diffraction was used to study further samples of molten iron oxides which had exploded vigorously or modestly. The X-ray diffraction studies of the debris from iron oxide explosions are summarized in Table 2-IV.

2.2.5 Scientific Interchanges With Other Laboratories

During this quarter Dr. G. Fröhlich, of the Institute for Nuclear Energy, University of Stuttgart, visited Sandia Laboratories. His recent work on vapor film collapse and its relationship to steam explosion triggering phenomena was discussed.

TABLE 2-IV

FeO_x Debris Examined by X-Ray Diffraction

Starting Material	Initial Oxygen (wt %)	Initial Oxygen (at. %)	Expt. No.	ΔP_{max} (MPa)	Line Observed	Remarks
Fe_2O_3	30.1	60.0	10-72-1	3.64	FeO	
			9-149-1	0.13	FeO + Fe_3O_4	
			10-61-1	1.70	FeO + (1 line not identified)	Flexible Hearth
			10-70-1	0.27	FeO + (Fe_3O_4 or δFe_2O_3)	
			10-73-2	0.25	FeO + Fe_3O_4	
(Fe_2O_3 + Fe	27.6	57.1	10-39-1	0.23	FeO	
			10-40-1	1.37	FeO	
			10-39-2	5.67	FeO	
(Fe_3O_4 + Fe)	26.0	55.1	10-55-2	0.22	FeO + (1 line not identified)	
	24.0	52.4	10-54-1	0.22	FeO	

References - Section 2

1. D. A. Dahlgren, ed., Light Water Reactor Safety Research Program Quarterly Report - October to December 1977, SAND78-0600, Sandia Laboratories, Albuquerque, NM, August 1978.

2. D. A. Dahlgren, ed., Light Water Reactor Safety Research Program Quarterly Report - January to March 1978, SAND78-1511, Sandia Laboratories, Albuquerque, NM, September 1978.

3. Debris from Fragmentation Experiment No. 1 furnished by T. Y. Chu, Division 1537, Sandia Laboratories, Albuquerque, NM.

4. G. Long, in Metal Progress 71, pp 107-12, May 1957.

5. P. D. Hess and K. J. Brondyke, in Metal Progress 95, pp 93-100, April 1969.

6. L. S. Nelson and L. D. Buxton, Steam Explosion Triggering Phenonmena: Stainless Steel and Corium-E Simulants Studied With a Floodable Arc Melting Apparatus, SAND77-0998 (NUREG/CR-0122), Sandia Laboratories, Albuquerque, NM, May 1978.

3. Statistical Analysis

3.1 Summary (M. Berman, H. C. Monteith, G. P. Steck, and J. Orman)

The goal of this program is to develop and apply statistical methods for studying the peak clad temperature (PCT) probability distribution as calculated by RELAP4 for a loss-of-coolant accident (LOCA). Past research has indicated that the response-surface method would be one of the best approaches, given the constraints of a limited number of expensive runs.

This year, work will concentrate on the production of response surfaces for the blowdown and reflood parts of the LOCA using the RELAP4/MOD6/UPD4 code. Results for this quarter follow.

Investigation of the steady-state capability of RELAP continued. An acceptable steady state was achieved for the nominal 100% power case. It was not possible to calculate a steady-state situation, however, when the off-nominal powers of 106 and 94% were used. Differences of up to 50 °F in PCT were observed, depending on the duration of the prebreak transient (or pseudo-steady) calculation. Work is continuing on the initialization question.

The list of blowdown variables and ranges was completed during the quarter. Coding to implement these variables into the RELAP code has been written and checked out. Sensitivity studies will be performed to determine the fuel state (fresh or once-burned) to be used for the study.

3.2 Steady State and Problem Initialization (M. Berman, H. C. Monteith, and J. Orman)

In the previous quarterly it was shown that, for certain time steps, oscillations of large amplitude occurred in many parts of the system during steady-state runs. These oscillations were found to be due to anomalous choking. The unphysical choking was caused by excessively high flow estimates made by the explicit flow predictor, WIEST, in subroutine FLOSRH. This estimate was improved by including frictional terms as discussed in detail in Section 4. Figures 3-2 and 3-3 illustrate the significant improvement resulting from the new flow estimator in some typical junction flows. (A nodalization diagram for Zion is shown in Figure 3-1.)

It is now clear that an adequate steady-state calculation can be made by RELAP for the nominal case of 100% power, if the time steps are chosen judiciously and a pressurizer simulator is employed. This steady state (i.e., no break initiation) is not significantly affected if the reactor kinetics calculation is disabled. Runs with and without reactivity feedback are compared in Figures 3-4 through 3-8. Normalized power (constant unity for no reactivity feedback), fuel stored energy, and core coolant temperature are almost identical, although some flows show

slight differences. These calculations indicated that a mild transient occurred at early times but was essentially damped by about 15 seconds. Several runs were made to investigate whether these mild departures from steady state had any effect on the transient calculations. The three runs delayed the break for 0.01, 20.1 and 80.1 seconds.

The transient part of the runs (with the various steady-state relaxation times suppressed) are overlayed in Figures 3-9 through 3-12. Most parameters were nearly identical (cf. normalized power and fuel-stored energy). The PCT calculated with a 0.01 second delay, however, was 15°F higher than with a 20.01 second relaxation period. The fact that there was no further change in PCT from 20 to 80 seconds delay indicates that steady-state convergence had been achieved by 20 seconds or earlier.

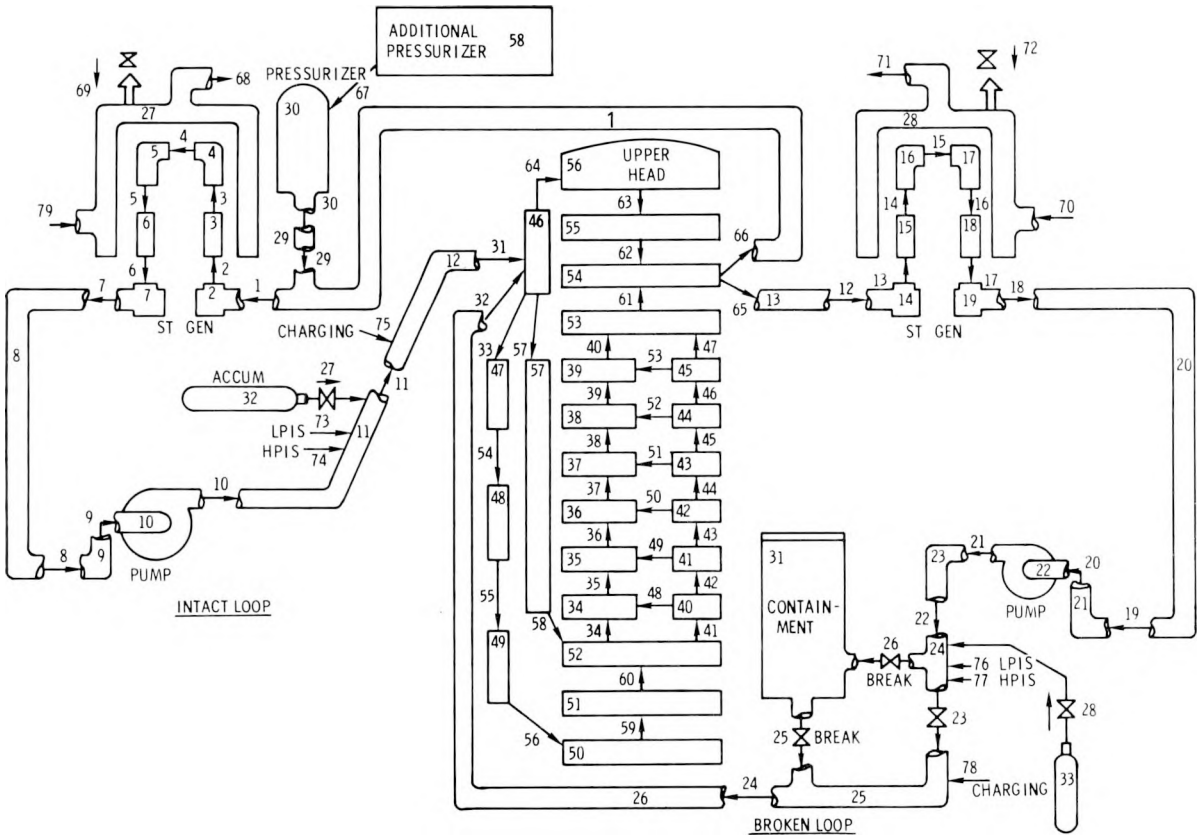

Figure 3-1. RELAP4 Nodalization for Statistical Study

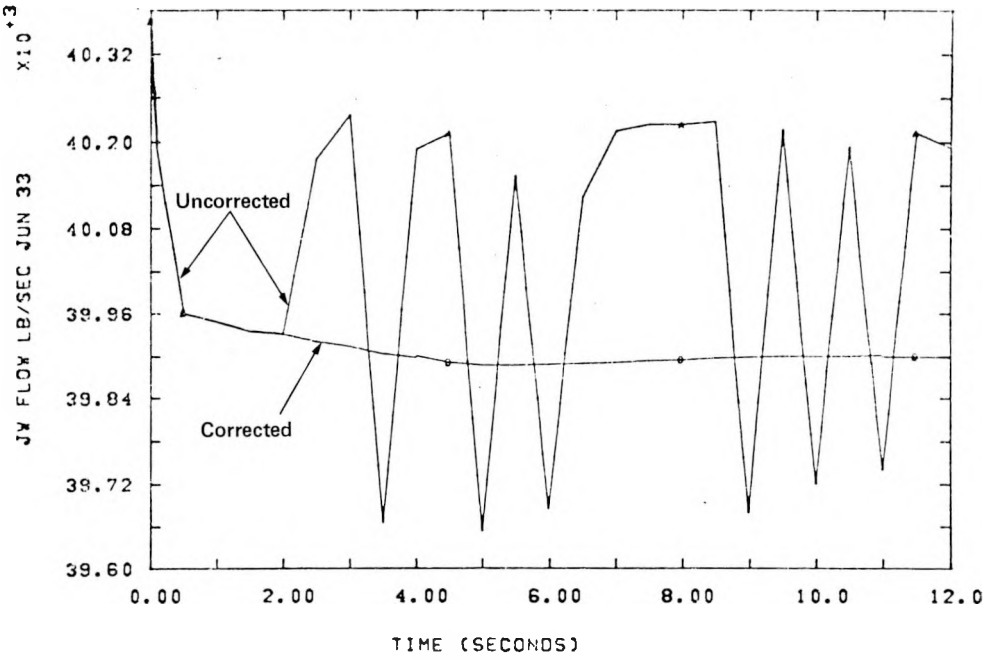

Figure 3-2. Downcomer Flow, Uncorrected vs Corrected Inertial Estimator, 100% Power

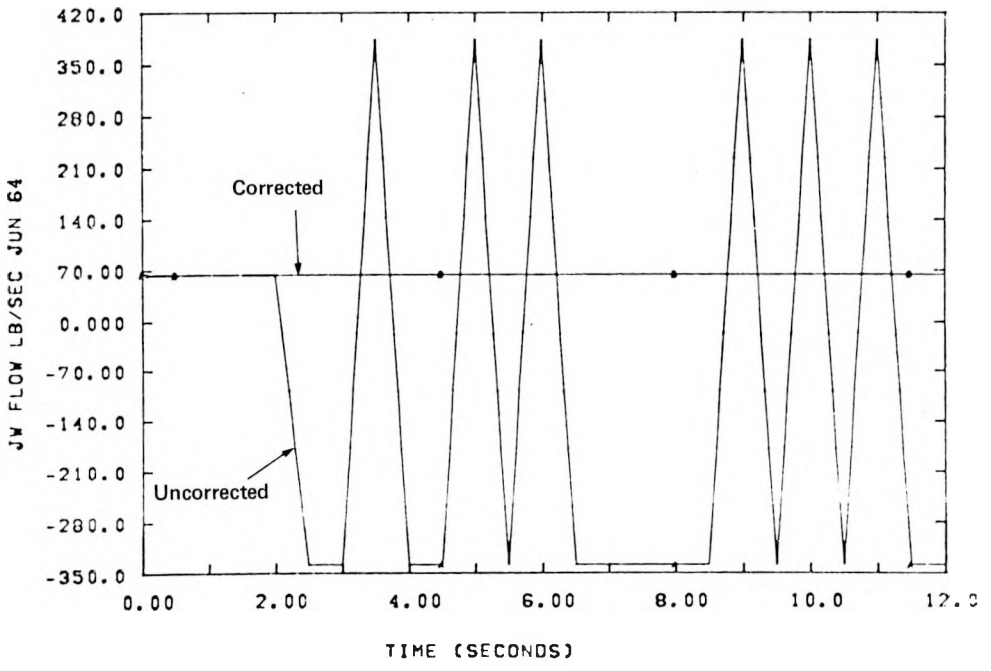

Figure 3-3. Flow From Inlet Annulus to Upper Head, Uncorrected vs Corrected Inertial Estimator, 100% Power

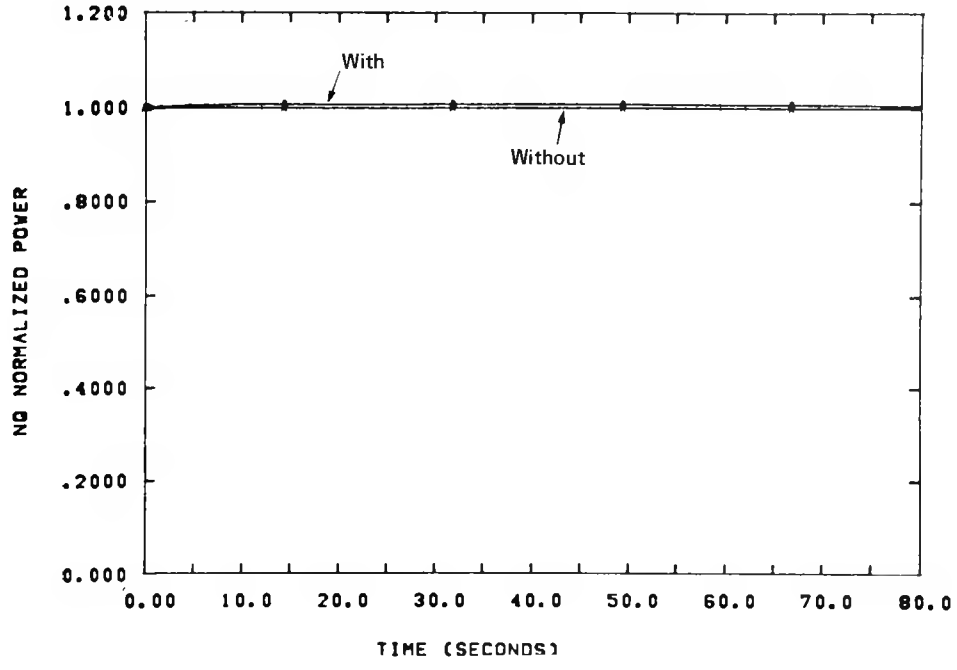

Figure 3-4. Normalized Power, With and Without Reactivity Feedback, 100% Power

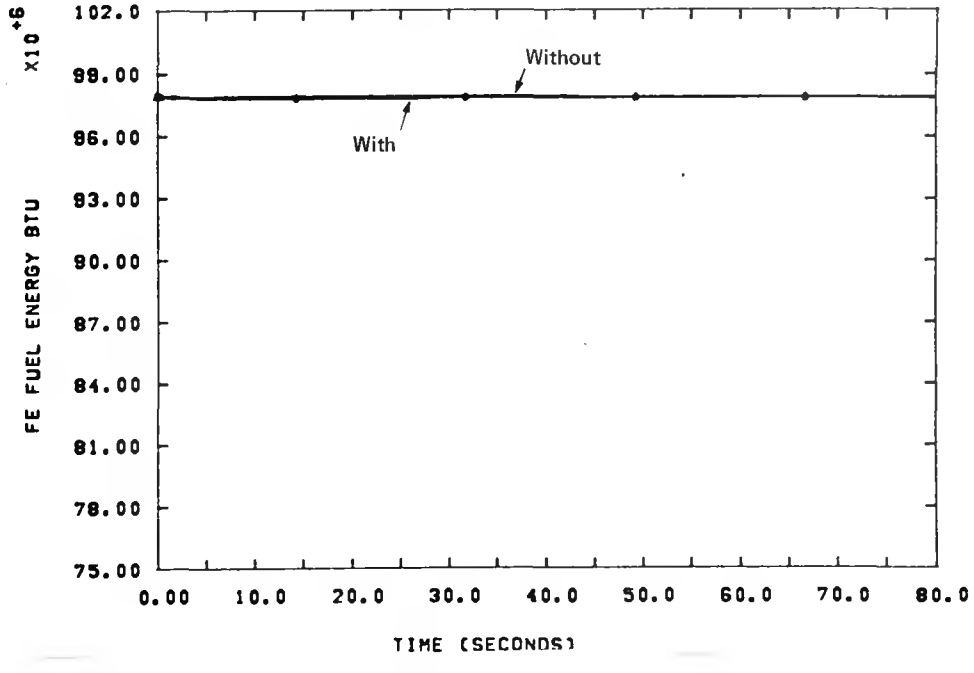

Figure 3-5. Fuel Stored Energy, With and Without Reactivity Feedback, 100% Power

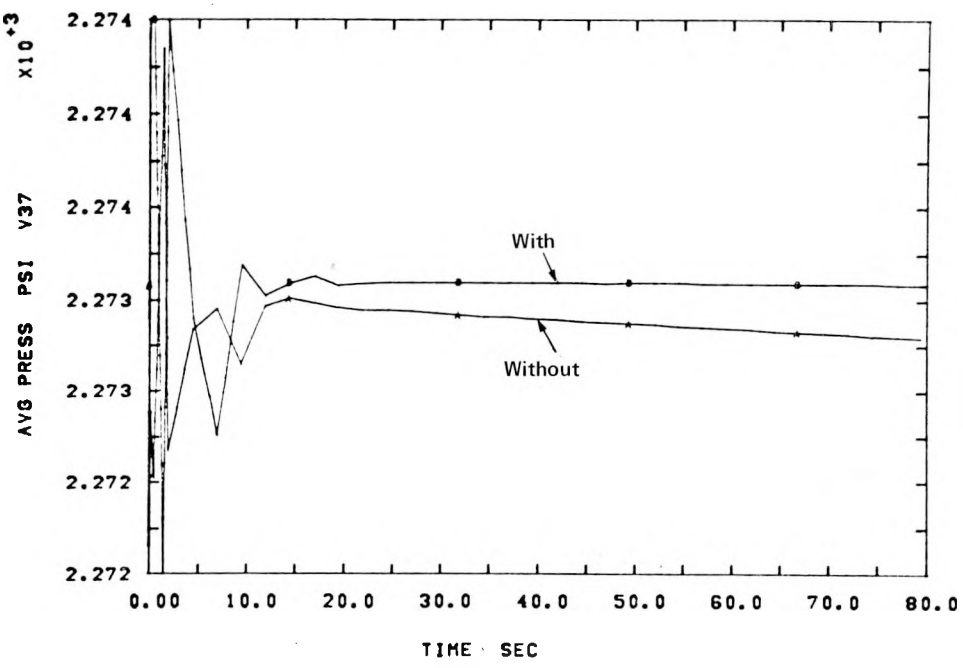

Figure 3-6. Average Core Pressure, With and Without Reactivity Feedback, 100% Power

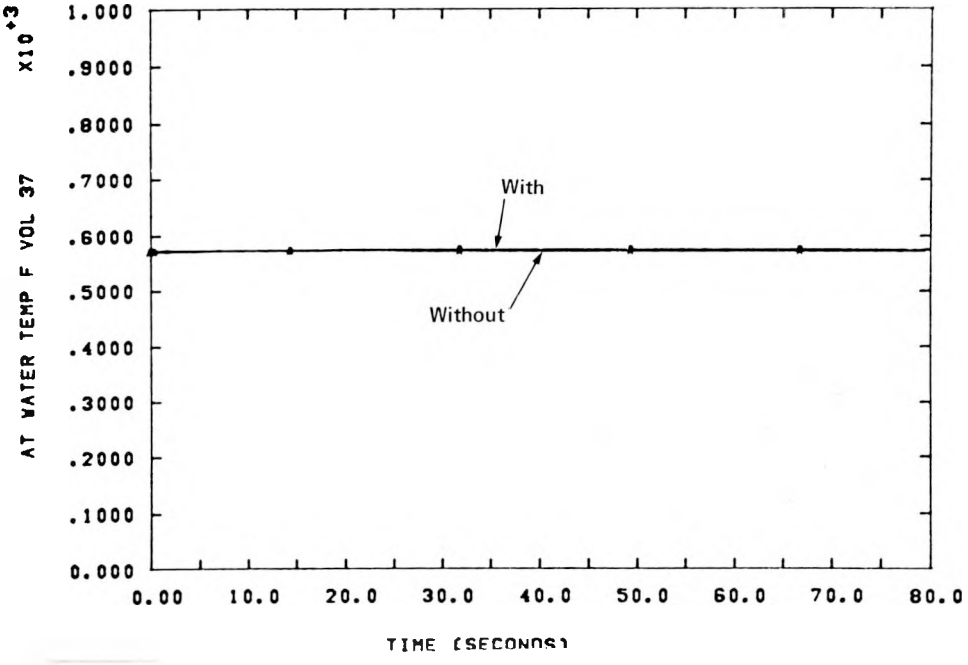

Figure 3-7. Core Coolant Temperature, With and Without Reactivity Feedback, 100% Power

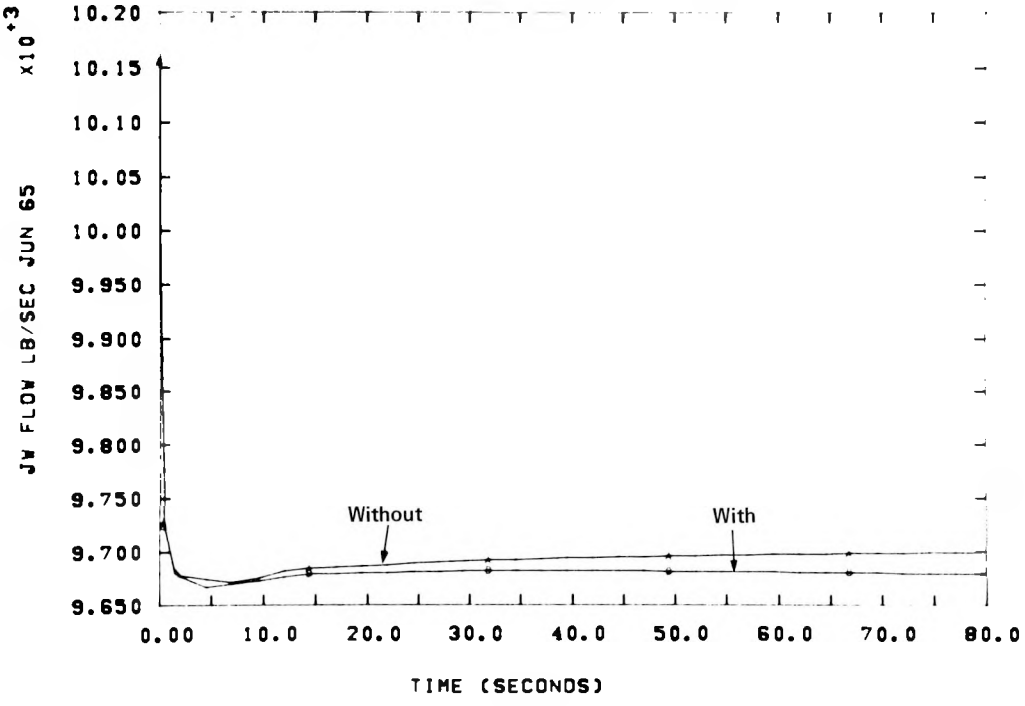

Figure 3-8. Flow at Junction 65, With and Without Reactivity Feedback, 100% Power

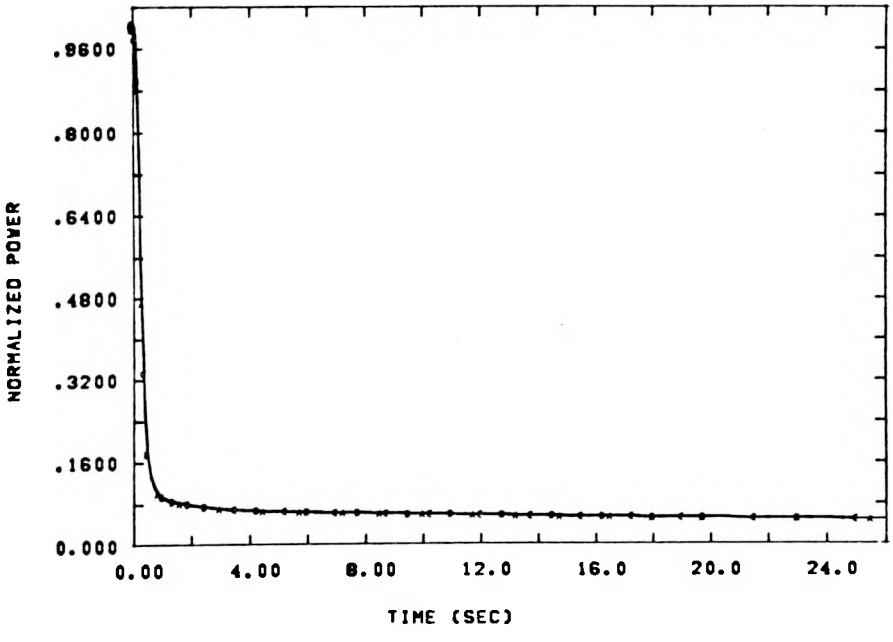

Figure 3-9. Normalized Power, Break Initiation Delayed by 0.01, 20.01, and 80.01 Seconds, 100% Power

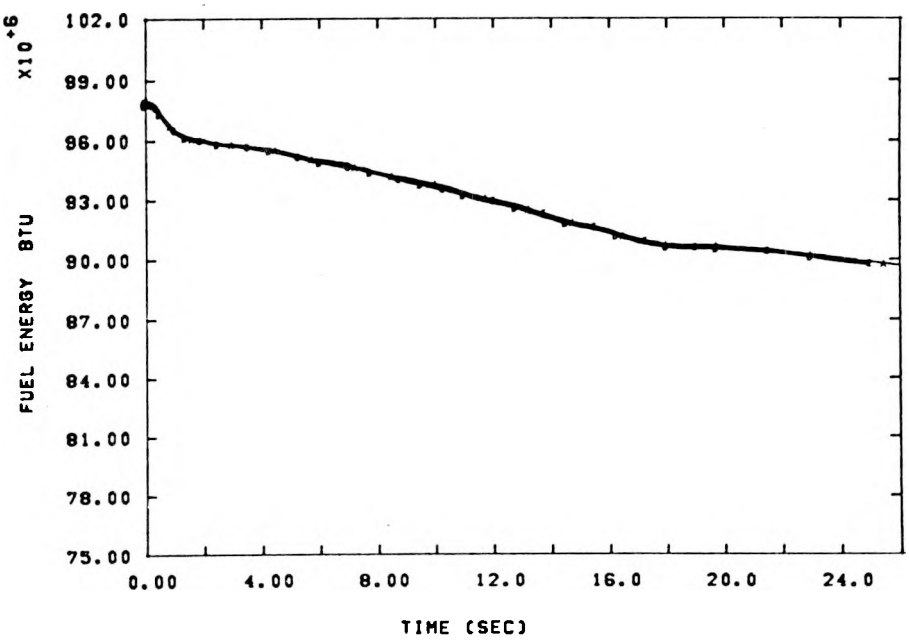

Figure 3-10. Fuel Stored Energy, Break Initiation Delayed by 0.01, 20.01, and 80.01 Seconds, 100% Power

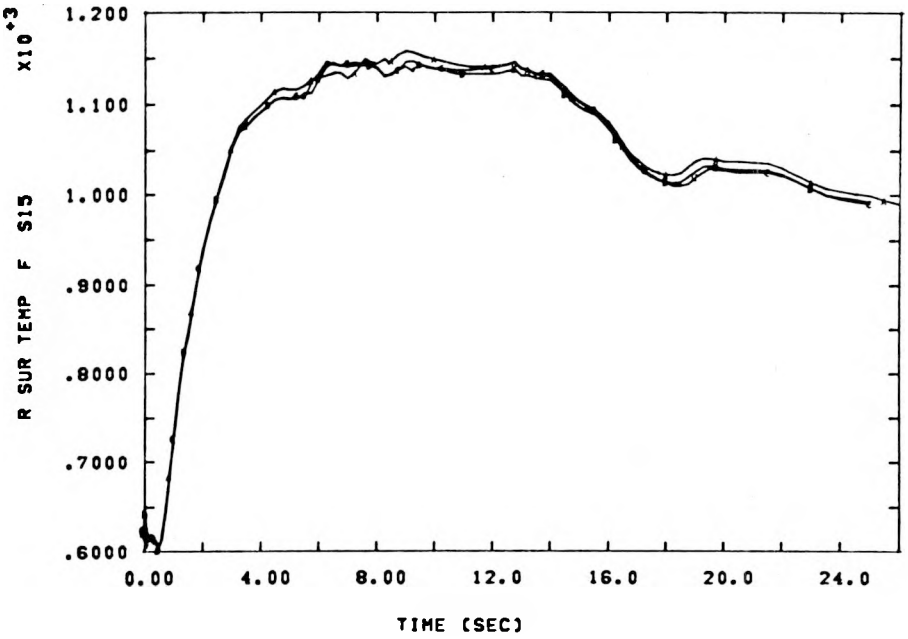

Figure 3-11. Clad Temperature in Slab 15, Break Initiation Delayed by 0.01, 20.01, and 80.01 Seconds, 100% Power

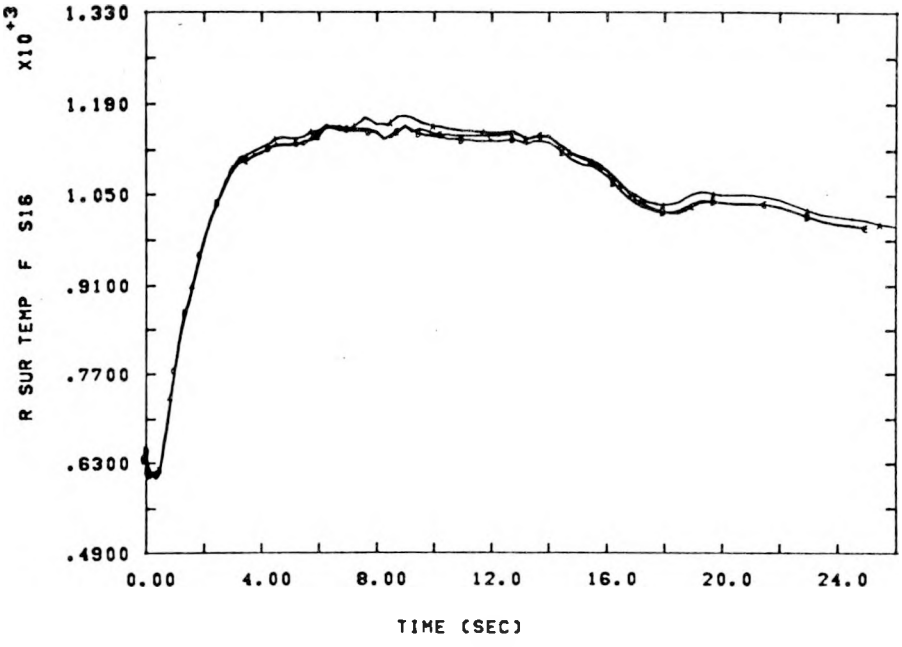

Figure 3-12. Clad Temperature in Slab 16, Break Initiation Delayed by 0.01, 20.01, and 80.01 Seconds

Since it was demonstrated that RELAP itself could converge to a steady state in about 15 seconds reactor time, it might then be possible for runs begun at off-nominal powers to be initialized by simply running the code for some "relaxation period" before initiating the break. These pseudo-steady runs (in reality, transient runs with no pipe break) were made at 106 and 94% power levels, both with and without the reactivity feedback options (Figures 3-13 through 3-24). Figure 3-13 shows the gradual decrease in power with reactor kinetics on and the constant power without reactivity feedback (RB). Core stored energy rises more rapidly without RB, Figure 3-14. The reverse occurs at the low power level of 94%, Figures 3-21 and 3-22. Rod temperatures (Figures 3-16 and 3-24), core pressures and temperatures (Figures 3-17 and 3-18, respectively), and steam generator primary (Figure 3-19) and secondary (Figure 3-20) temperatures showed almost no dependence on the reactivity feedback calculation. For the high-power case, however, temperatures showed a slowly increasing trend while, for low power, a gradual decrease was evident. These trends represented a small fraction of the nominal values and might prove to be inconsequential in a blowdown calculation. To investigate this, combined pseudo-steady and transient runs were made as before. Figures 3-25 through 3-28 are overlays of the transient parts of four calculations at 106% power run for relaxation periods of 0.01, 20.01, 80.01, and 200.01 seconds before break initiation. Little difference is observed in power decay (Figure 3-25) or fuel stored energy (Figure 3-26). Clad temperatures (Figures 3-27 and 3-28) ranged from a low of 1185°F after a 200 second relaxation period to a high of 1242°F after 80 seconds. More importantly, there was no evidence of convergence with increasing relaxation times. The times of PCT occurrence after the break ranged from 9 to 13.8 seconds.

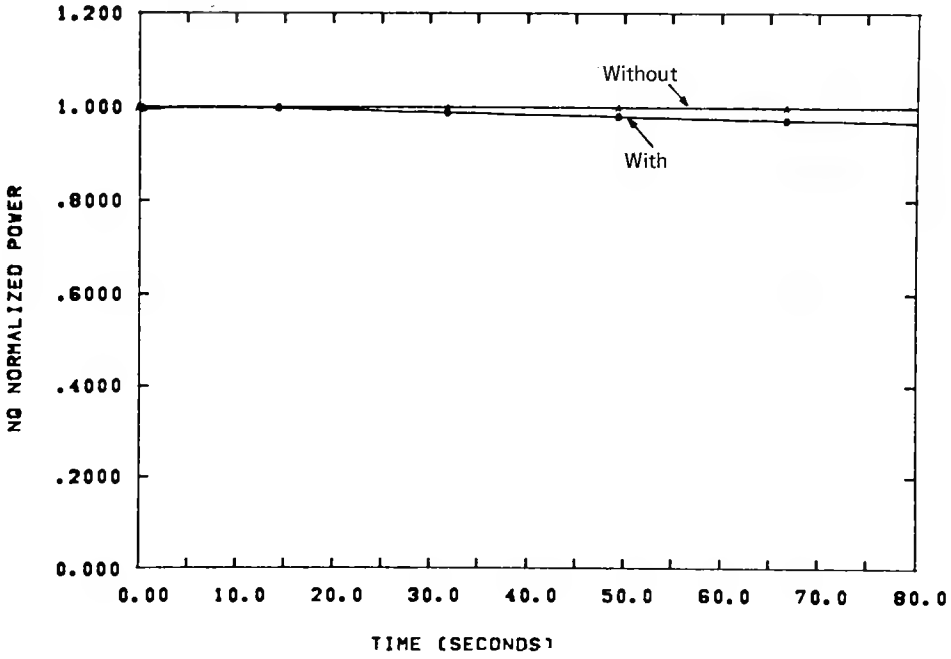

Figure 3-13. Normalized Power (106% Level), With and Without Reactivity Feedback

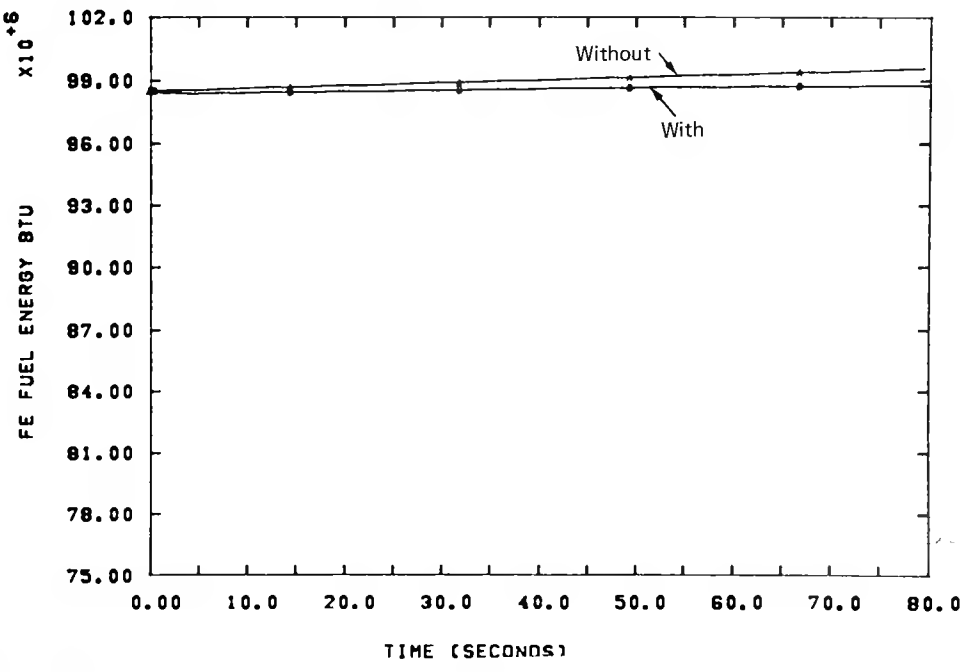

Figure 3-14. Fuel Stored Energy at 106% Power With and Without Reactivity Feedback

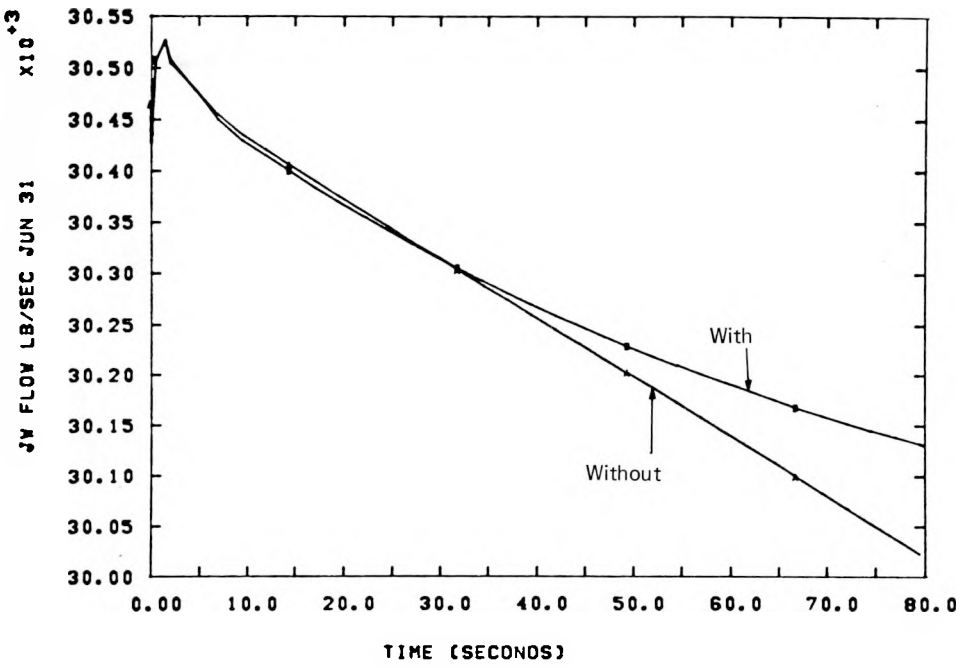

Figure 3-15. Flow at Junction 31, 106% Power Level, With and Without Reactivity Feedback

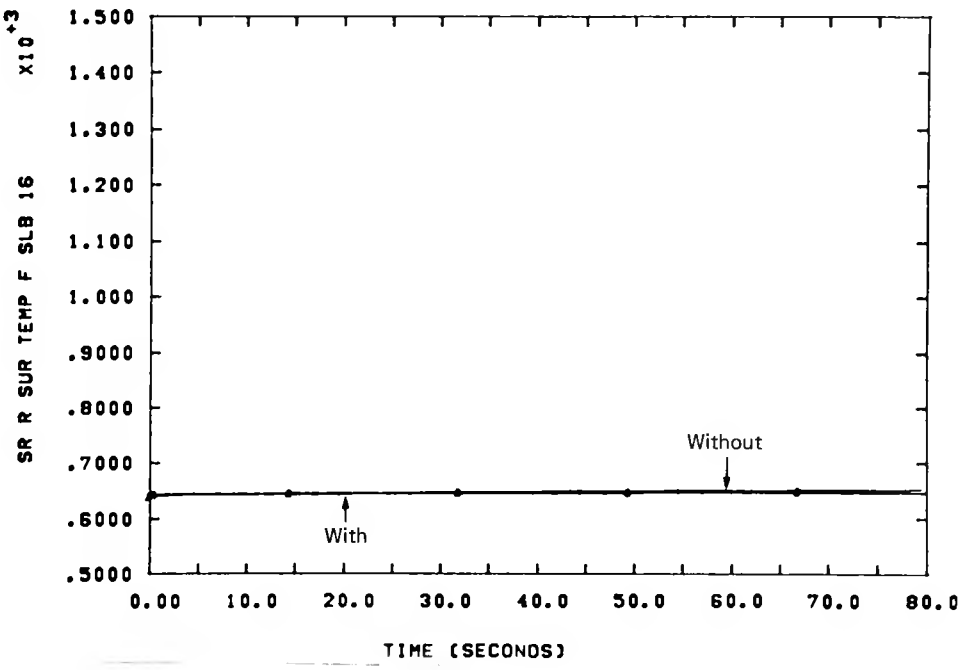

Figure 3-16. Rod Temperature, 106% Power, With and Without Reactivity Feedback

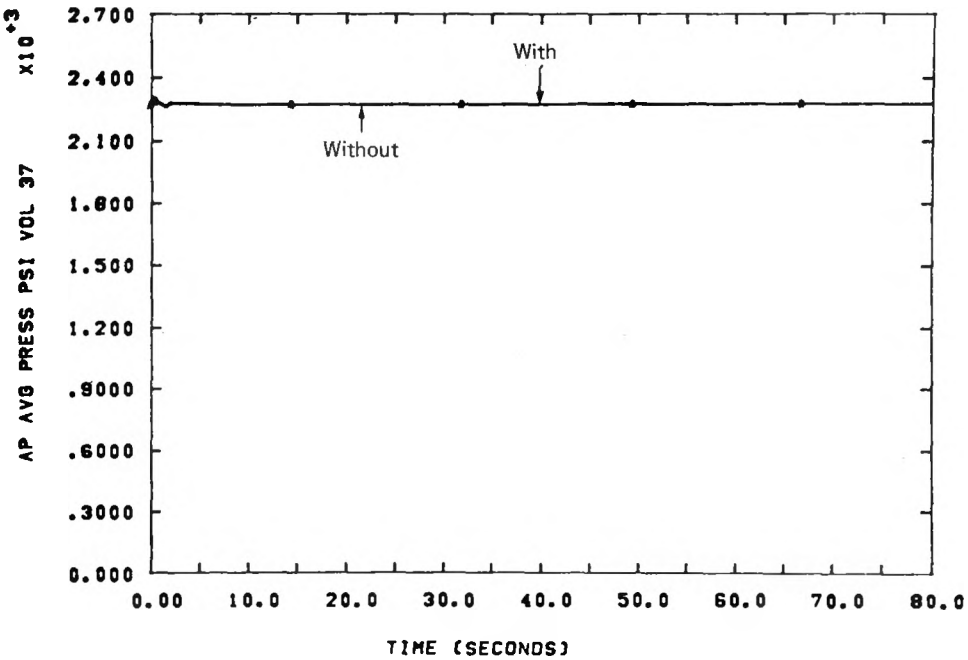

Figure 3-17. Average Core Pressure, 106% Power, With and Without Reactivity Feedback

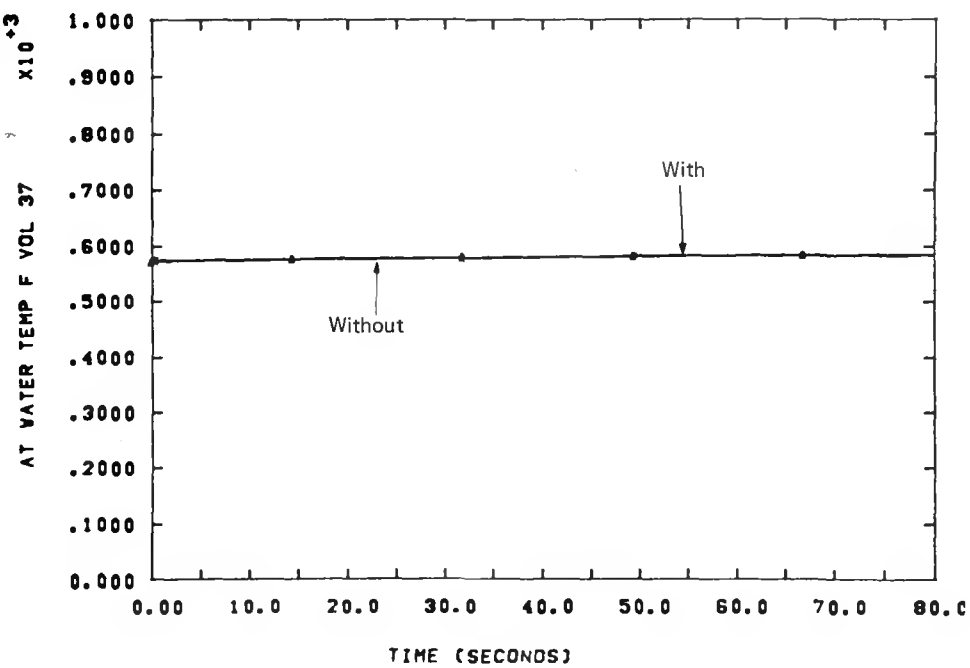

Figure 3-18. Core Coolant Temperature, 106% Power, With and Without Reactivity Feedback

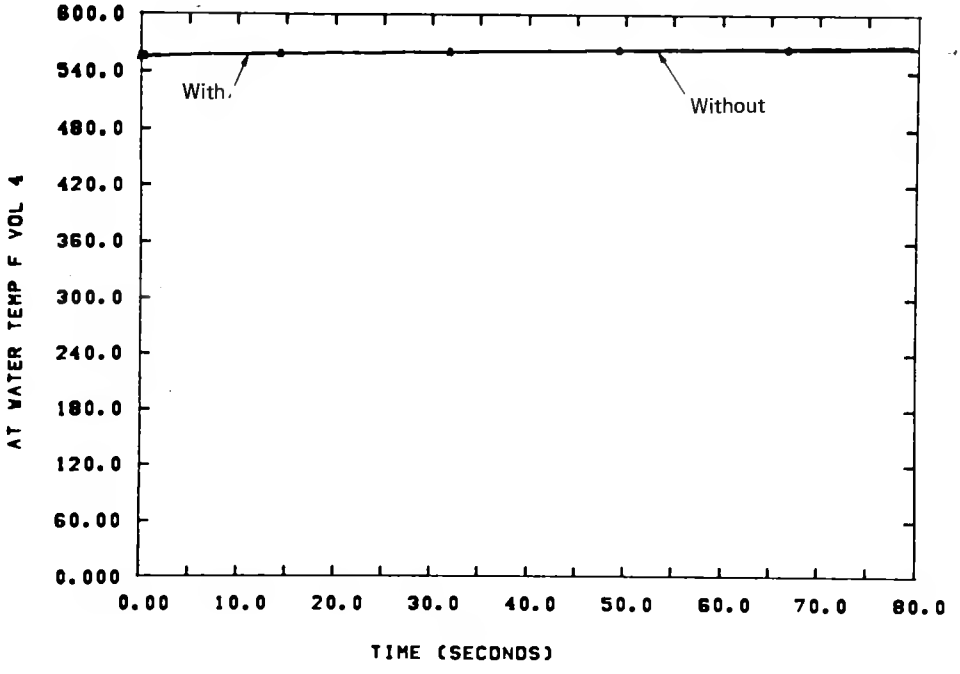

Figure 3-19. Temperature of Steam Generator Primary, 106% Power, With and Without Reactivity Feedback

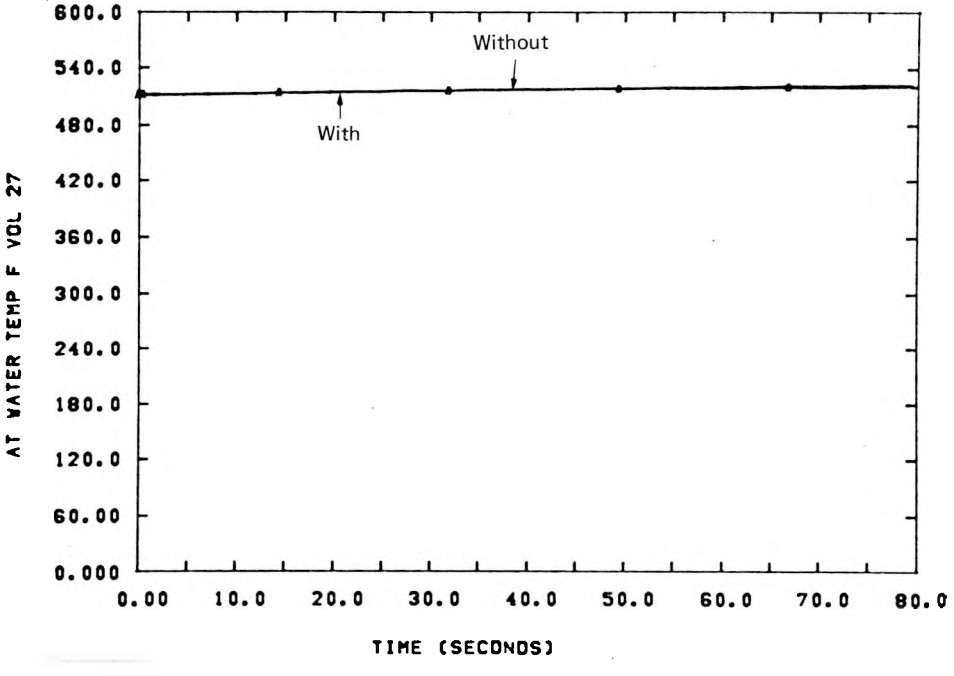

Figure 3-20. Temperature of Steam Generator Secondary, 106% Power, With and Without Reactivity Feedback

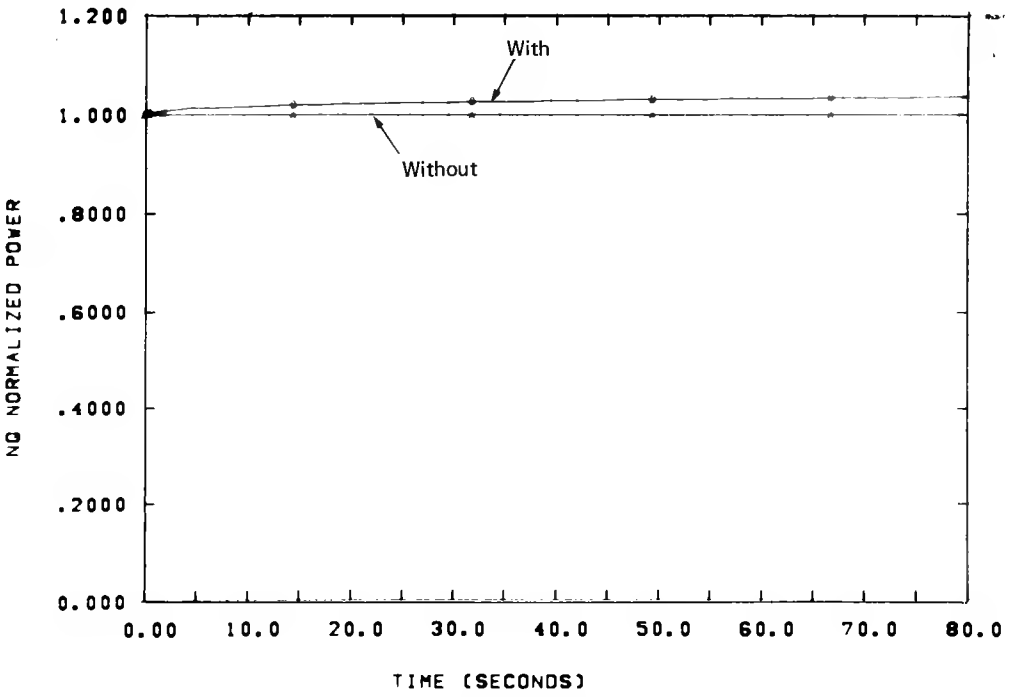

Figure 3-21. Normalized Power (94% Level) With and Without Reactivity Feedback

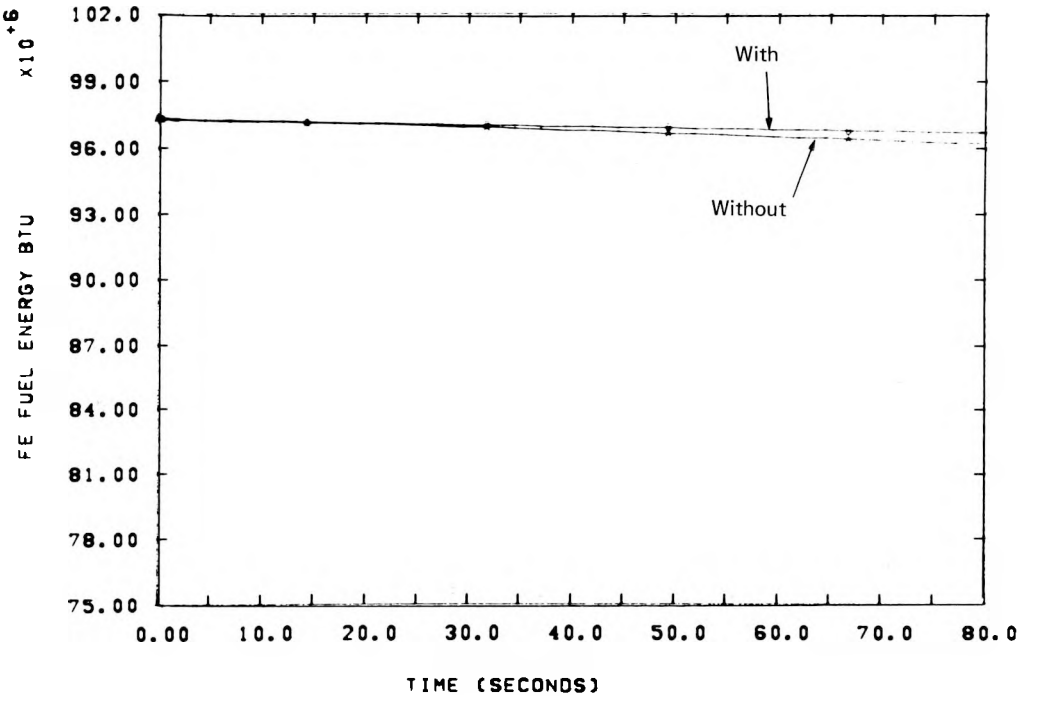

Figure 3-22. Fuel Stored Energy at 94% Power, With and Without Reactivity Feedback

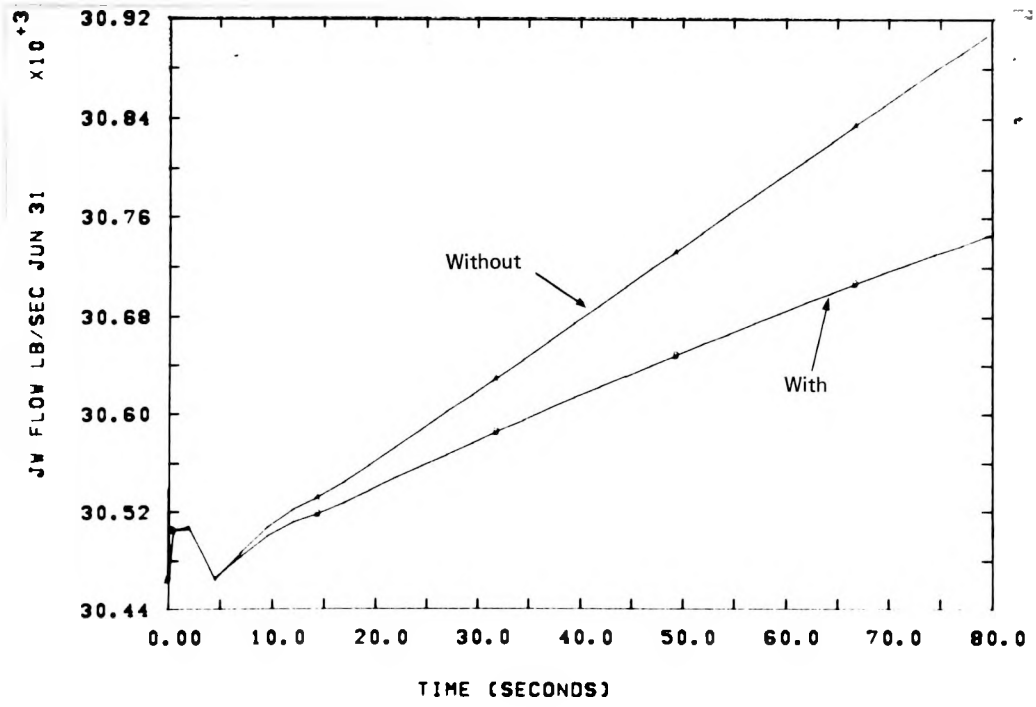

Figure 3-23. Flow at Junction 31, 94% Power Level, With and Without Reactivity Feedback

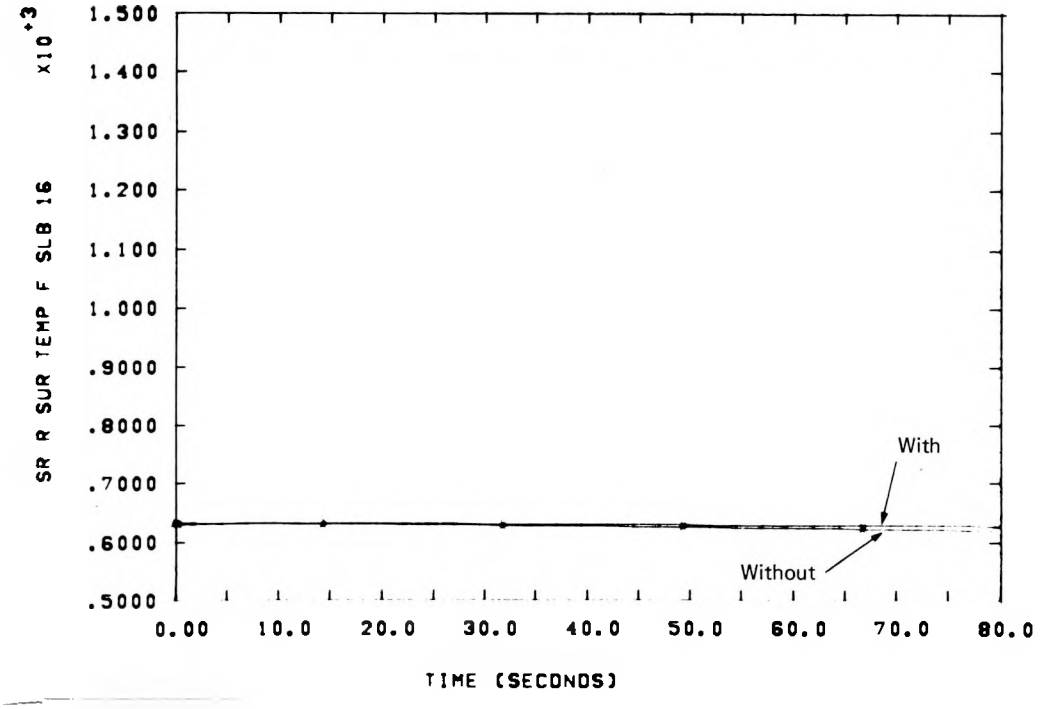

Figure 3-24. Rod Temperature, 94% Power, With and Without Reactivity Feedback

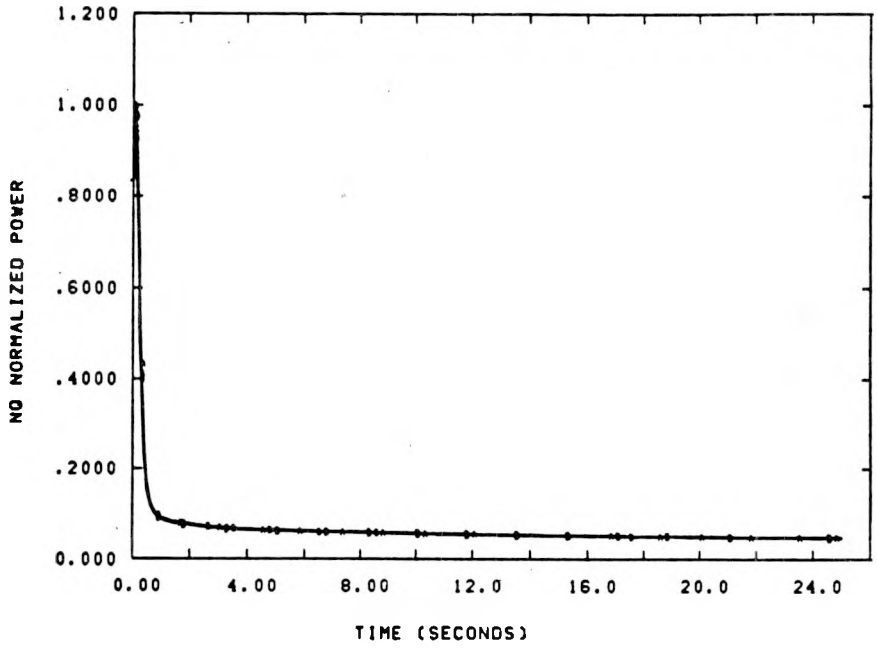

Figure 3-25. Normalized Power (106% Level), Break Initiation Delayed by 0.01, 20.01, 80.01, and 200.01 Seconds

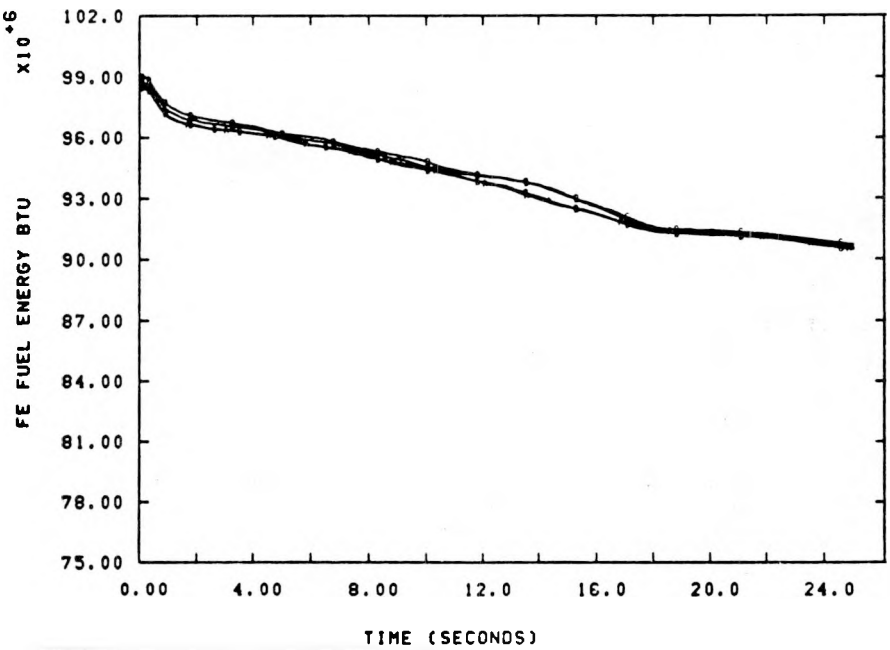

Figure 3-26. Fuel Stored Energy at 106% Power, Break Initiation Delayed by 0.01, 20.01, 80.01, and 200.01 Seconds

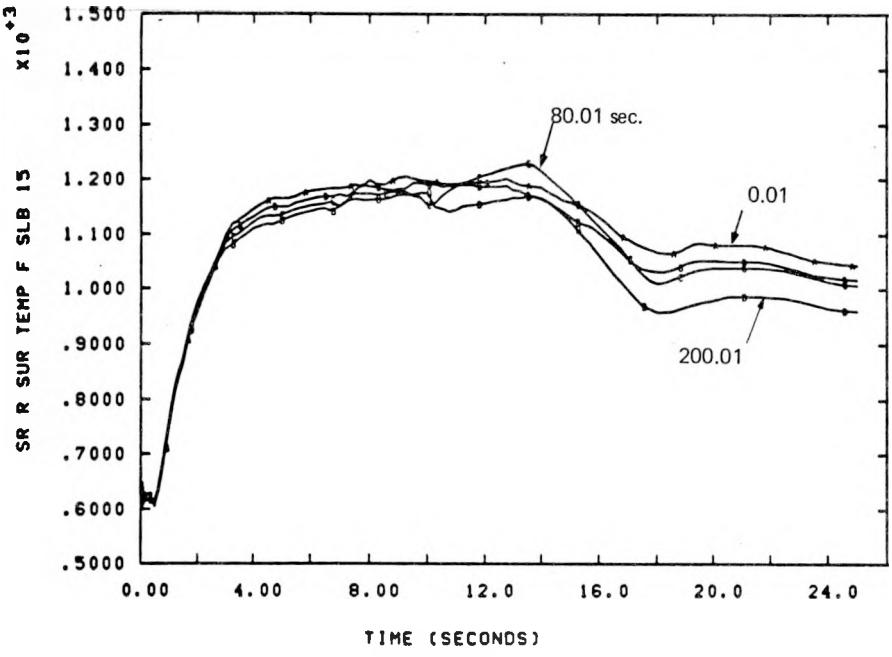

Figure 3-27. Clad Temperature in Slab 15, 106% Power, Break Initiation Delayed by 0.01, 20.01, 80.01, and 200.1 Seconds

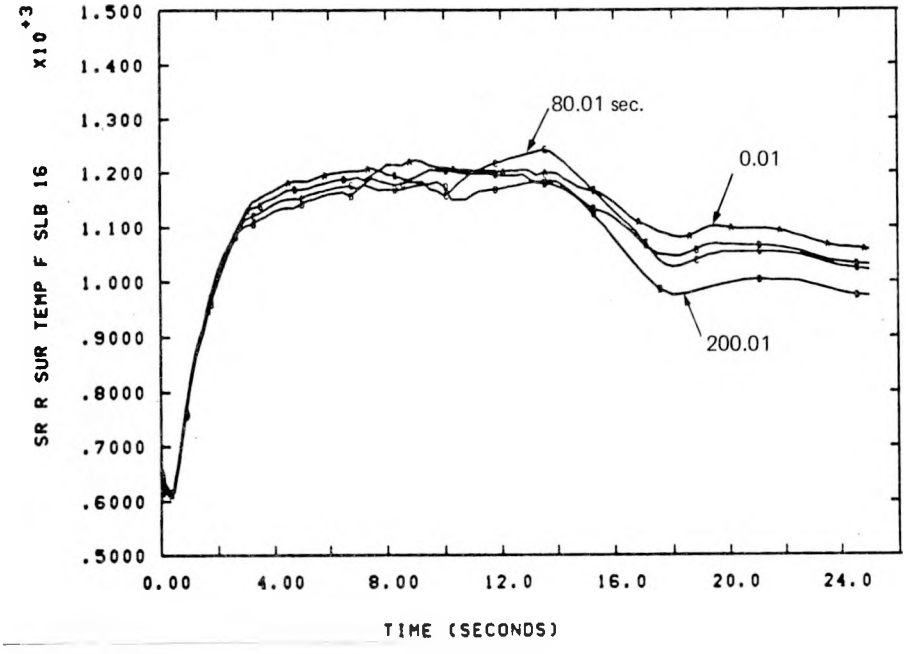

Figure 3-28. Clad Temperature in Slab 16, 106% Power, Break Initiation Delayed by 0.01, 20.01, 80.01, and 200.01 Seconds

For the equivalent low-power runs, power decay was essentially unaffected as it was for high power, Figure 3-29. Core-stored energy at 94% power, however, demonstrated (Figure 3-30) a more marked dependence on relaxation time than the comparable runs at 106% power (cf. Figure 3-26). The effect of this stored energy difference shows up in clad temperature primarily after the peak has occurred, as can be seen in Figures 3-31 and 3-32. Peak clad temperatures differed by 49°F (1069° to 1118°F) and times of PCT ranged from 6.3 to 8.5 seconds. As before, the transient results do not appear to converge with increasing relaxation times.

Based on these calculations, the achievement of a steady state by running RELAP in a pseudo-steady (or pretransient relaxation) mode does not seem to be a practical approach to problem initialization, with or without the reactivity feedback options. The pseudo-transient relaxes to the steady state too slowly because of the large thermal inertia of the reactor, although mechanical balance, in terms of volume pressures, can usually be achieved in a few primary loop transits. It should be noted, however, that the differences in computed PCT may not be significant compared to other uncertainties in the study. This will be investigated in the next few quarters.

3.3 Blowdown Variable Selection and Input (M. Berman, H. C. Monteith, and J. Orman)

In References 1 and 2, the input parameters for the statistical study were selected for the initial development of a response surface for peak clad temperature in the blowdown phase of a PWR LOCA. A large number of diverse sources were employed in parameter selection, range determination, and in the actual methods by which this information would be implemented in the RELAP4/MOD6 code. We have collected all the appropriate data and have selected the methods for implementing the nominal values and ranges of the variables. Some quantities will be varied by means of simple multiplicative "dials." Others may require extensive precalculations external to RELAP, e.g., the translation of time-in-life (as a parameter) into axial and radial peaking factors and thence into RELAP4 heat slab input data, using the information presented in Reference 3.

Some of the dials which will be used are part of the normal RELAP4 input. Others were specially programmed by INEL or Sandia. The INEL updates are discussed in Reference 4.

A preprocessor program has been written by Sandia. Input to this program consists of 21 "statistical variables" which are transmuted by the program into output physical variables acceptable as normal RELAP4 input data. The relationships between these two types of variables will be discussed in detail.

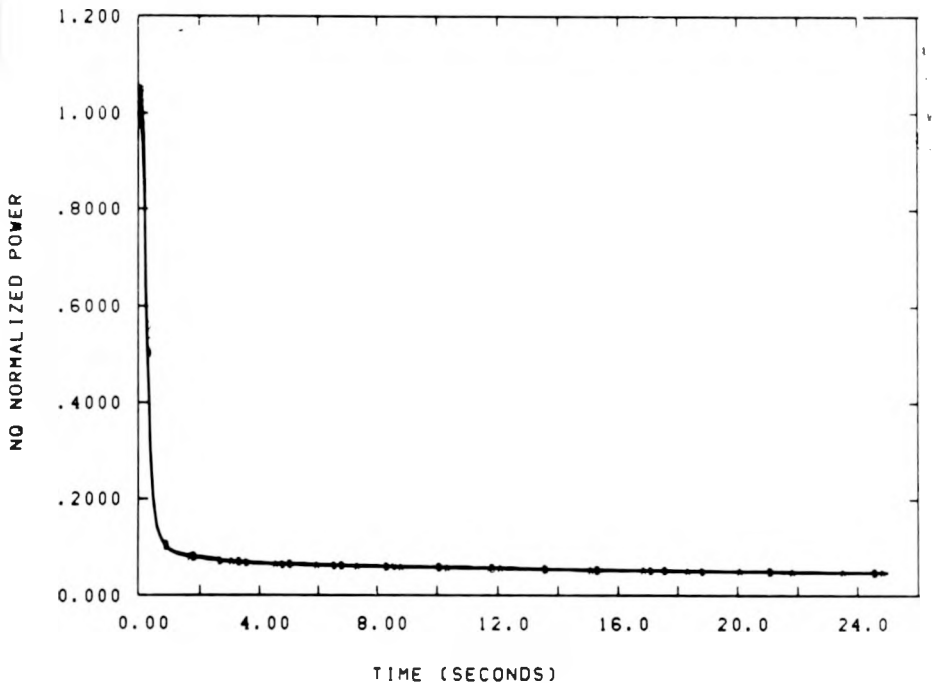

Figure 3-29. Normalized Power (94% Level), Break Initiation Delayed by 0.01, 20.01, and 200.01 Seconds

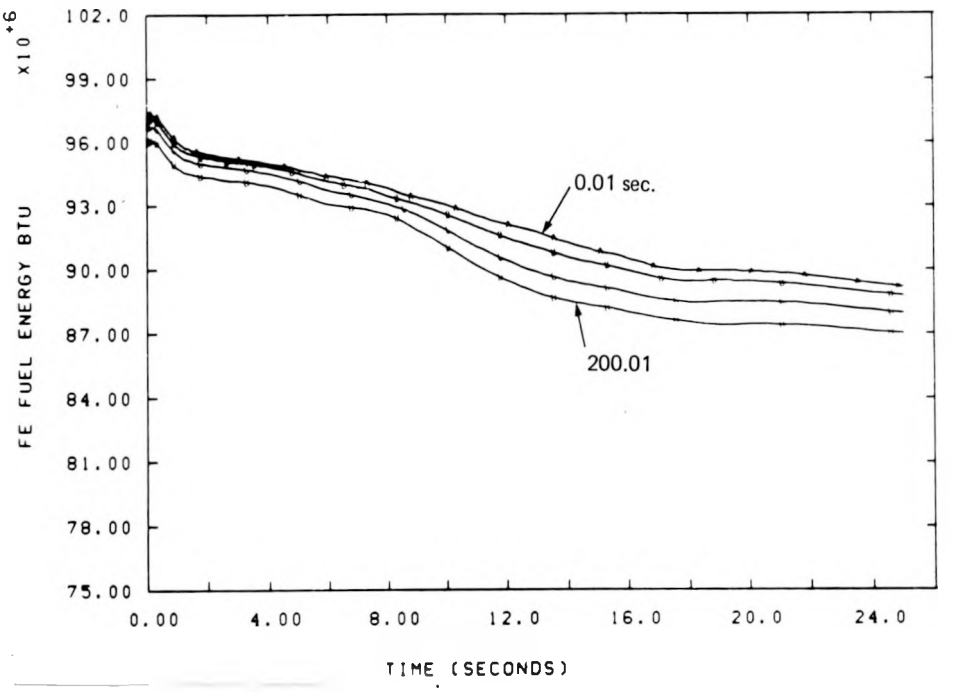

Figure 3-30. Fuel Stored Energy at 94% Power, Break Initiation Delayed by 0.01, 20.01, 80.01 and 200.01 Seconds

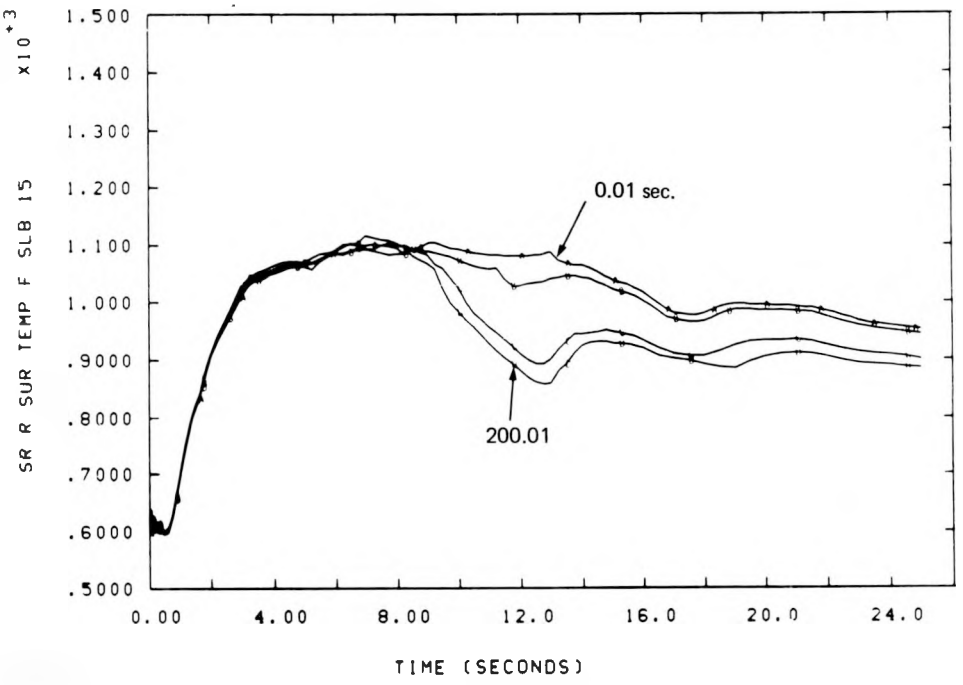

Figure 3-31. Clad Temperature in Slab 15, 94% Power, Break Initiation Delayed by 0.01, 20.01, 80.01, and 200.01 Seconds

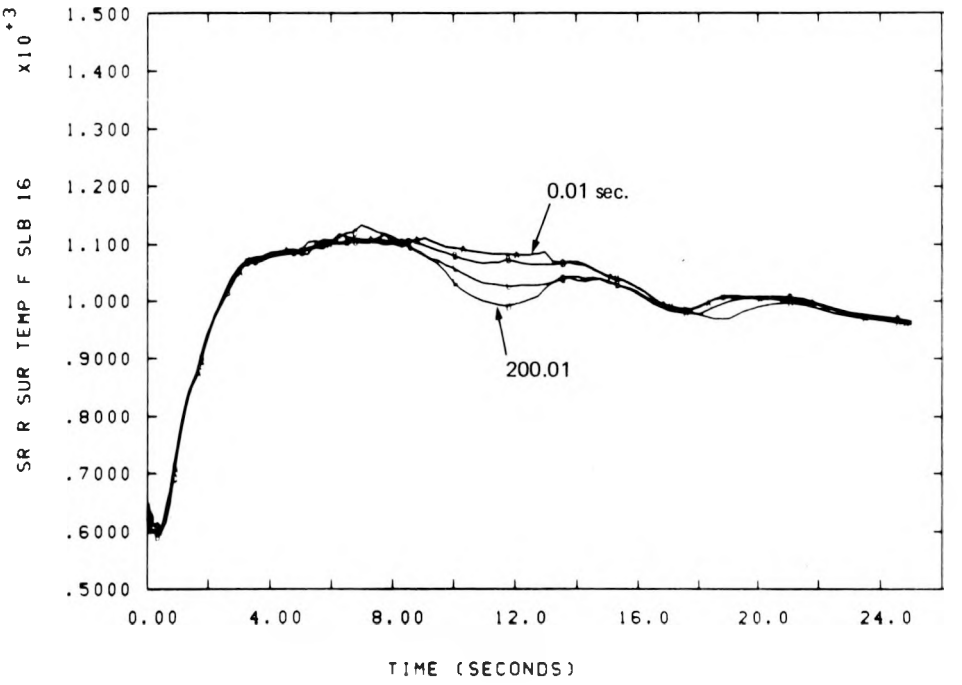

Figure 3-32. Clad Temperature in Slab 16, 94% Power, Break Initiation Delayed by 0.01, 20.01, 80.01, and 200.01 Seconds

3.3.1 Preprocessor Input Data

1. Discharge Coefficient, C_D, for Break Flow (Subcooled) -- Name of the dial used is DLEHRY, range: 0.7 to 1.2, nominal 0.9. This dial is input directly without any processing and is placed on card 082003, word 3. DLEHRY is the flow rate multiplier for subcooled (extended) Henry critical flow. (Default = 1.)

2. Discharge Coefficient, C_D, for Break Flow (Saturated) -- Name of the dial used is DLHEM, actual range: 0.75 to calculated maximum of $(C_D)_{max} = 1. + 1.5\ e^{-10.986\ X}$, nominal 1.0. DLHEM is the flow rate multiplier for HEM. (Default = 1.) The actual range will be changed for use in the preprocessor to -0.25 to 1., nominal 0.; i.e., an interpolation between the nominal curve and the maximum and minimum curves will be based on DLHEM. Place this dial on card 082003, word 1. The dial must be processed in the RELAP4 as follows:

In FUNCTION LEAK, delete RELAP 40527 and insert the following.

```
      IF (DLHEM.GT.O.) GO TO 331
      DLXX = 1. + DLHEM
      GO TO 332
  331 DLXX = 1.0 + DLHEM*(1.5*EXP(-10.986*X)
  332 CONTINUE
```

Here, "X" is the source quality.

3. SLIP -- Name for parameter input to preprocessor is SLIP, range -1.0 to 1.0, nominal 0. Name of dial used is DLVSLP, range: 0.3 to calculated value, nominal 1.0. This dial will have several values because it is a function of the void fraction α.

$$\text{DLVSLP}(\alpha) = 1.0 + \text{SLIP}*0.7, \quad \text{For SLIP} \leq 0.0$$

$$\text{DLVSLP}(\alpha) = 1.0 + \text{SLIP}*2.0, \quad \text{For SLIP} > 0.0 \text{ and } 0.0 \leq \alpha \leq 0.8$$

$$\text{DLVSLP}(\alpha) = 3.0*(1.0 + (\alpha - 0.8)/0.195) \text{ for SLIP} > 0.0 \text{ and } \alpha > 0.8$$

The parameter DLVSLP is used as a multiplier on the churn-turbulent relative velocity correlation. The data cards for this dial require ten input pairs of values for α and DLVSLP. These values will be specified by means of a data statement and are

Void Fraction Values: 0.0, 0.15, 0.3, 0.45, 0.6, 0.7, 0.8, 0.9, 0.95, and 0.995

These values of the void fractions and the above formulas determine the dial quantities which are placed on cards 082097 - 082099.

4. Two-Phase Form Loss and Friction Loss Pressure Drop --

a. The two-phase form loss pressure drop is changed by use of the dial DLTFJ, range: 0.4 to 1.6, nominal = 1.0. This quantity is placed in word 1 of card 082096.

b. The two-phase friction loss pressure drop is changed by means of the dial DLTFFM, range 0.4 to 1.6, nominal = 1.0. Its value is the same as that of DLTFJ above. This quantity is placed in word 1 of card 082020.

5. DNB Correlation -- Name of the dial used is DCHF, range: 0.3 to 3.0, nominal = 1.0. This dial is placed in word 1 of card 082030.

6. High Flow Film Boiling Mode 6 -- Name of the dial used is DHTC6, range 0.5 to 2.0, nominal = 1.0. Place this dial in word 5 of card 082031.

7. Low Flow, High Void Fraction, Free Convection and Radiation (Mode 7) -- Name of dial used is DHTC7, range: 0.6 to 1.5, nominal = 1.0. Place this quantity in word 6 of dial card 082031.

8. Forced Convection to Vapor: Dittus-Boelter (Mode 8) -- Name of dial used is DHTC8, range: 0.5 to 2.0, nominal = 1.0. This quantity is placed in word 7 of card 082031.

9. Low Flow, Low Void Fraction: Modified HSU and Bromley-Pomeranz (Mode 9) -- Name of dial used is DHTC9, range: 0.7 to 1.5, nominal = 1.0. This quantity is placed in word 8 of card 082031.

10. Flow Blockage -- Name of dial used is DLBLK, range: 0.4 to 1.6, nominal = 1.0. This quantity is placed in word 1 of card 082095.

11. Zr - H_2O Reaction -- Name of dial used is DLMWR, range 0.85 to 1.15, nominal = 1.0. This dial is placed in word 1 of card 082021.

12. Power Level -- Name of input parameter - DLPWR, range: 0.94 to 1.06, nominal = 1.0. Calculate the power level with the equation:

POWER = DLPWR*3238.0.

Place this quantity in word 1 of card 010002.

13. Containment Pressure -- The nominal containment pressures are given in the following table:

Nominal Containment Pressures

Time After Break, T (sec)	Containment Pressure, P(T) (psia)
0	14.7
10	39.0
16	44.0
20	44.0
40	38.0
80	36.0
120	34.0
160	33.0
200 and beyond	32.0

The name of the preprocessor input quantity is DLCPR, range: -5.0 to 10.0 psia, nominal = 0. For times, $T \geq 10$ seconds, containment pressures, PRES(T) and temperatures, TEMP(T) are changed to

$$\text{PRES}(T) = P(T) + \text{DLCPR}$$

$$\text{TEMP}(T) = \text{saturation temperature corresponding to PRES}(T)$$

Saturation temperatures are interpolated from the steam tables. The initial state (14.7 psia, 68°F) is unchanged by DLCPR. The altered pressures and temperatures are placed in the appropriate positions on cards 07XXYY.

14. Pump Degradation -- The preprocessor is given three sets of data points: one for high values of head multiplier, one for low values and a set of nominal values.

High Curve		Nominal Curve		Low Curve	
α	MH(α)	α	MN(α)	α	ML(α)
0.0	0.0	0.0	0.0	0.0	0.0
0.05	1.0	0.1	0.0	0.15	0.0
0.95	1.0	0.15	0.05	0.5	0.6
1.0	0.0	0.24	0.8	0.9	0.6
		0.3	0.96	1.0	0.0
		0.4	0.98		
		0.6	0.97		
		0.8	0.90		
		0.9	0.80		
		0.96	0.50		
		1.0	0.0		

Name of the parameter input into the preprocessor is DLPUMP, range: -1.0 to 1.0, nominal = 0.0 The dial determines how far above or below the nominal curve to go in interpolating between the maximum and minimum functions. The new head multiplier is, therefore, given by

$$M(\alpha) = MN(\alpha) + DLPUMP*(MN(\alpha) - ML(\alpha)), \text{ for } DLPUMP \leq 0.$$

$$M(\alpha) = MN(\alpha) + DLPUMP*(MH(\alpha) - MN(\alpha)), \text{ for } DLPUMP > 0.$$

Place these values on the pump head multiplier cards 0910YY.

15. ECC Temperature -- ECCTMP is the name for the ECC Temperature. Range of ECCTMP is 40 degrees to 140 degrees, nominal = 90.0. This value is placed in the 8th position of the following data cards: 130300, 130400, 130500, 130600, 130700, 130800, and also on cards 050321, and 050331.

16. Accumulator Pressure -- Name of input parameter to preprocessor is DLACC. Range is 593.2 to 693.2 psia, nominal 643.2 psia. Place the new accumulator pressure in the third position of the data cards 050321, and 050331.

17 & 18. Radial and Axial Peaking Factors and Time-In-Life of Fuel -- To analyze this parameter, it is necessary to give tables of peaking factor data from which interpolations will be made. All of these data can be input to the preprocessor by means of data statements. The data are given as peaking factors versus time-in-life, TLF, in months, see Reference 3.

Given TLF, the appropriate cycle (NC) and time into the cycle (TIC) are determined as follows:

IF $0 \leq TLF \leq 11.$, NC = 1 and TIC = TLF

IF $11 \leq TLF \leq 22$, NC = 2 and TIC = TLF - 11

IF TLF > 22, NC = Equilibrium cycle and
TIC = AMOD (TLF, 11)

Axial Peaking Factors
Cycle 1

Time in Months	Axial Peaking Factor, P_Z
0	1.41
3	1.35
6	1.26
9	1.20
12	1.17

Total Peaking Factors
Cycle 1

Time in Months	Total Peaking Factors, P_T
0	2.0
3	1.9
6	1.71
9	1.56
12	1.48

Axial Peaking Factors Cycle 2	
Time in Months	Axial Peaking Factor, P_Z
0	1.15
1.33	1.15
2.67	1.15
4.0	1.15
5.33	1.15
6.67	1.15
8.0	1.15
9.0	1.15
9.33	1.15
12.0	1.15

Total Peaking Factors Cycle 2	
Time in Months	Total Peaking Factors, P_T
0	1.7
1.33	1.68
2.67	1.66
4.0	1.64
5.33	1.645
6.67	1.665
8.0	1.67
9.0	1.675
9.33	1.68
12.0	1.68

For the equilibrium cycle the curve of Axial Peaking Factor versus time in months is a straight line and can be obtained from the equation:

$$P_Z = \text{AXIAL PEAKING FACTOR} = -0.0055*\text{TIME} + 1.19.$$

For the equilibrium cycle the curve of Total Peaking Factor is also a straight line and can be obtained from the equation:

$$P_T = \text{TOTAL PEAKING FACTOR} = -0.01667*\text{TIME} + 1.675.$$

There is now a need for several curves which give Normalized Power versus P_Z. First, data for these curves will be given for cycle 1:

Axial Node 1 (Bottom of the Core)	
Normalized Power	Axial Peaking Factor
0.993	1.16
0.847	1.17
0.75	1.20
0.689	1.25
0.725	1.325
0.818	1.39

Axial Node 2	
Normalized Power	Axial Peaking Factor
1.07	1.16
1.13	1.17
1.117	1.25
1.12	1.30
1.119	1.35
1.26	1.39

Axial Node 3	
Normalized Power	Axial Peaking Factor
1.02	1.16
1.11	1.17
1.207	1.25
1.34	1.39

Axial Node 4	
Normalized Power	Axial Peaking Factor
0.99	1.16
1.11	1.17
1.214	1.25
1.24	1.39

Axial Node 5		Axial Node 6	
Normalized Power	Axial Peaking Factor	Normalized Power	Axial Peaking Factor
1.07	1.16	0.887	1.16
1.09	1.17	0.679	1.17
1.112	1.25	0.581	1.25
0.895	1.39	0.52	1.30
		0.38	1.39

Cycle 2
Axial Peaking Factor = Constant = 1.15

Node	Normalized Power
1	0.848
2	1.11
3	1.117
4	1.12
5	1.082
6	0.7154

For the equilibrium cycle the Normalized Power versus Axial Peaking Factor are all straight lines and can be obtained with the following formulas:

Axial Node 1, Bottom of Core:

$$P(1) = -1.12*P_Z + 2.207$$

Axial Node 2:

$$P(2) = 1.48*P_Z - 0.587$$

Axial Node 3:

$$P(3) = 1.76*P_Z - 0.9139$$

Axial Node 4:

$$P(4) = 0.72*P_Z + 0.28$$

Axial Node 5:

$$P(5) = -0.064*P_Z + 1.797$$

Axial Node 6:

$$P(6) = -0.2*P_Z + 0.9634$$

We have assumed that these powers are based on the assumption of 6 equal axial nodes. In the Zion nodalization, however, the 5 lower nodes are equal, while the top node has only 49.6167% of the volume and surface area of the others. To account for this, the above powers are adjusted as follows:

$$C = 0.09166667$$

$$P'(1) = P(1) + CP(2)$$

$$P'(2) = (1-C)\ P(2) + 2CP(3)$$

$$P'(3) = (1-2C)\ P(3) + 3CP(4)$$

$$P'(4) = (1-3C)\ P(4) + 4CP(5)$$

$$P'(5) = (1-4C)\ P(5) + 5CP(6)$$

$$P'(6) = (1-5C)\ P(6)$$

The peaking factor uncertainty, (PFUNC-1. = ± 16%), is assumed to reside wholly in the radial component. The new total peaking factor, P'_T, becomes

$$P'_T = PFUNC*P_T = P_Z*P_R$$

where $P_R = PFUNC*P_T/P_Z$ is defined as the ratio of power in the hottest rod to average rod power. The hot channel peaking factor is arbitrarily defined by

$$PKFHC = P_R/1.15, \quad \text{if } P_R \geq 1.15$$

$$= 1., \qquad \text{if } P_R < 1.15$$

These quantities are now used to modify the axial and total peaking factors.

$$\text{Define PNORM} = \sum_{I=1}^{6} P'(I)$$

$$\text{and DEN} = (192. + PKFHC)*PNORM.$$

Normalizing factors for the 3 core sections can then be written:

FAC1 = 192./DEN for average core

FAC3 = PR/(204.*DEN) for hot pin

and FAC2 = (PKFHC/DEN) - FAC3, for hot channel

The power fractions in all of the nodes are determined from the equations:

$$PN(I) = FAC1*P'(I),\ I = 1, 6$$

$$PN(I+6) = FAC2*P'(I),\ I = 1, 6$$

$$PN(I+12) = FAC3*P'(I),\ I = 1, 6$$

$$\text{and} \sum_{I=1}^{18} PN(I) = 1$$

Place these values in the sixth position of the core cards, 160010 to 160180.

19. UO_2 Thermal Conductivity -- A dial, DLECON, has been provided by Ken Katsma on card 082076, Reference 4. The purpose of this dial is to multiply the code calculated UO_2 thermal conductivity. Range is 0.6 to 1.3; nominal 1.

20. Gap Size -- The BEB09 deck received contained fuel (FW_o) and gap (GW_o) cold radial widths of

$$FW_o = 1.52458 \times 10^{-2} \text{ ft}$$

$$GW_o = 3.54167 \times 10^{-4} \text{ ft}$$

Fuel width will be preserved but gap width will be redefined.
The unirradiated cold radial gap is defined to be

$$GW_o = 3.16667 \times 10^{-4} \text{ ft}$$

The width of fuel plus gap will be treated as constant:

$$W_o = FW_o + GW_o = 1.55625 \times 10^{-2} \text{ ft}$$

For purposes of this study, the fuel will be treated as equilibrium cycle, fresh or once burned.
For fresh fuel,

$$GW_T = GW_o * \left\{0.3 + 0.7 * \left(\frac{15-T}{15}\right)\right\}, \quad T \leq 11 .$$

For once burned fuel,

$$GW_T = GW_o * \left\{0.3 + 0.7 * \left(\frac{15-T'}{15}\right)\right\}, \quad 11 < T' \leq 15$$

$$= 0.3 * GW_o, \quad 15 < T' \leq 22$$

T = AMOD (TLF, 11., where TLF is time-in-life defined as parameter 17 and T′ = T + 11. Also,

NOB = 0 → fresh fuel
= 1 → once burned fuel

An uncertainty band around GW_T will be defined by an additive dial, DLGAP, with a range -1.5 to +1.5 mils ($\pm 0.125 \times 10^{-3}$ ft), nominal 0.

$$GW = GW_T + DLGAP \geq 0$$

i.e., DLGAP is not permitted to produce a negative GW. The new fuel width, FW, becomes

$$FW = W_o - GW$$

FW is word 6 on 170101.

GW is word 4 on 170102.

21. Decay Heat -- INEL has sent us modifications to MOD6 which convert old ANS rates to the new revised ANS standard, Reference 5. This is accomplished with a table of time dependent multipliers, AMULTP(T); T = reactor time (in seconds) after problem start (T = 0). A constant multiplier of these values is also available. NRC, however, has requested a multiplier which would be a function of both time-in-life, TLF, and reactor time, T.

For fresh fuel, we will adopt the following approach. Given $F(T, \infty)$ as the decay heat power in MeV/fission (Reference 6), a normalized multiplier, $F(T,TL)$, can be defined as follows:

$$F(T,TL) = \left[F(T,\infty) - F(T+TL,\infty)\right]/F(T,\infty)$$

where TL is the time-in-life measured in seconds (assuming 2.628×10^6 seconds/month).

$$TL = 2.628 \times 10^6 * AMOD(TLF, 11.)$$

For once burned fuel, the normalized multiplier is given by

$$F(T,TL) = \Big\{F(T,\infty) - F(T+TL,\infty) + F(T+TL+2.628\times10^6,\infty) - F(T+TL+3.1536\times10^7,\infty)\Big\}/F(T,\infty)$$

This expression assumes the reactor has been operated at full power for 11 months and then shut down 1 month for refueling.

This function, $F(T,TL)$, can be further adjusted by an uncertainty dial, DLDEC, as follows:

$$F(T,TL) = (1. + DLDEC)*F(T,TL), \quad \text{if } -.06 \leq DLDEC \leq 0$$

$$F(T,TL) = F(T,TL) + DLDEC*(1.2 - F(T,TL)), \quad \text{if } 0 < DLDEC \leq 1.$$

A negative value of DLDEC reduces the nominal $F(T,TL)$ by 0. to 6%. A positive value for DLDEC results in an interpolation between the nominal $F(T,TL)$ and a maximum determined by 20% above the infinite irradiation value of 1.0. Note that the EM values do not represent the upper bound; 1.2 times the revised ANS is the final maximum. This set of numbers $F_i(T_i, TL)$ is then entered in RELAP as multipliers of the $(AMULTP, T_i)$ in subroutine RKENER.

We should note that the use of the previous prescriptions implies that the nominal base case Zion calculation now has distinct differences from the original BEB09 data deck supplied by INEL. The most important differences occur in the containment pressure history, the peaking factors as determined by the core heat slab power fractions, the gap and cladding widths and the computation of decay heat.

The following table summarizes the "statistical variables" and their ranges and nominal values.

TABLE 3-I

Preprocessor Input Parameters - Summary

	Parameter	Range	Nominal Value
1.	DLEHRY = subcooled discharge coefficient	0.7 → 1.2	0.9
2.	DLHEM = saturated discharge coefficient	-0.25 → 1.0	0.
3.	SLIP = slip correlation dial	-1. → 1.	0.
4.	DLTF = 2-phase form loss dial DLTFFM = 2-phase Fanning friction loss dial These dials are assumed to be equal, and a single variable	0.4 → 1.6	1.
5.	DCHF = critical heat flux dial	0.3 → 3.0	1.
6.	DHTC6 = Condie-Bengston dial	0.5 → 2.0	1.
7.	DHTC7 = free convection and radiation dial	0.6 → 1.5	1.
8.	DHTC8 = Dittus-Boelter dial	0.5 → 2.0	1.
9.	DHTC9 = Hsu and Bromley-Pomeranz dial	0.7 → 1.5	1.
10.	DLBLK = flow blockage dial multiplier	0.4 → 1.6	1.
11.	DLMWR = multiplier of Cathcart-Pawel reaction rates	0.85 → 1.15	1.
12.	DLPWR = power level multiplier	0.94 → 1.06	1.
13.	DLCPR = increment to be added to containment pressure	-5. → 10. psia	0.
14.	DLPUMP = dial for 2-phase pump head multiplier	-1. → 1.	0.
15.	ECCTMP = temperature of accumulator and safety injection system water	40° → 140°F	90°F
16.	DLACC = accumulator pressure	593.2 → 693.2 psia	643.2 psia
17.	TLF = time in life	0 → 440 months	226 months
18.	PFUNC = peaking factor uncertainty multiplier	0.84 → 1.16	1.
19.	DLECON = thermal conductivity dial multiplier	0.6 → 1.3	1.
20.	DLGAP = additive uncertainty in radial gap size NOB = 0 → fresh fuel = 1 → once burned fuel	±1.5 mils	0.
21.	DLDEC = decay heat multiplier	-0.06 → 1.0	0.

References - Section 3

1. Letter, C. Johnson, NRC, to D. A. Dahlgren, Sandia Laboratories, dtd 3/31/78, subject: Ranges of Parameters for Work Under FIN A-1205.

2. Letter, C. Johnson, NRC, to M. Berman, Sandia Laboratories, dtd 5/3/78, subject: Information Supplement to Letter of March 21, 1978.

3. Memo, B. W. Sheron, NRC, to C. Johnson, Sandia Laboratories, dtd 3/24/78, subject: The Treatment of an Uncertainty Distributions for Peaking Factors to be Used in Statistical LOCA Study.

4. Memo, K. R. Katsma, EG&G Idaho, to L. H. Sullivan, EG&G Idaho, dtd 12/29/77, subject: Parameters for Uncertainty Evaluation of PWR - KAT-38-77.

5. Letter, H. Chow, EG&G Idaho, to M. Berman, Sandia Laboratories, dtd 4/4/78, subject: Approximation to the New ANS Decay Heat Standard by Time-Dependent Multiplier - CHOW-1-78.

6. Proposed Revised ANS Standard (ANS5.1), Table 4, in letter from R. W. Peele, Oak Ridge National Laboratory.

4. UHI RELAP Model Development

4.1 Summary (M. Berman, R. K. Byers, R. K. Cole, Jr., R. R. Eaton, and J. Orman)

Upper head injection (UHI) describes a new emergency core cooling system developed by Westinghouse for pressurized water reactors using ice condenser containment systems. Analytic tools (predominantly RELAP4) presently available for studying loss-of-coolant accidents (LOCA) are considered inadequate in treating several phenomena whose import has increased with UHI. These include, among others:

- Increased importance of two-phase flow with slip
- Occurrence of top quench in the core
- Upper head draining during refill.

Sandia has embarked on a model development and testing program to improve the treatment of these phenomena in the RELAP4 code. Following are the results for this quarter.

A new nodalization scheme has been developed which appears to be a significant improvement over earlier models. The changes led to more realistic piping and downcomer flows and corrected some errors in core modeling. Using this nodalization, calculations were performed with the generic versions of RELAP4/MOD5 and MOD6 and Sandia-modified versions of MOD5. The results differed significantly in calculated flows, coolant and clad temperatures, and lower plenum fill behavior. An error in the potential energy term in RELAP was discovered and corrected. An improved flow estimator (used in critical flow modeling) was also coded. Neither of these changes corrected the unrealistic flow oscillations observed in the downcomer when the new slip and quench models were employed. There is strong evidence that the problem is due to the form of the slip correlations themselves, which appear to generate instabilities when combined with the RELAP difference equations. Work is continuing on this problem.

The FRAPT4 code was obtained from INEL and has been made operational on Sandia's CDC 7600 computer. A quench model has been incorporated into the code. Early results indicate that rod temperatures are sensitive to the time at which reflood is assumed to begin.

4.2 UHI RELAP Calculational Progress (M. Berman, R. K. Byers, R. K. Cole, Jr., R. R. Eaton, and J. Orman)

During the last quarter, a new plant model was developed for use in UHI blowdown calculations. This model, termed "UHI," differs from the next most recent, "UHK", as follows (Figure 4-1):

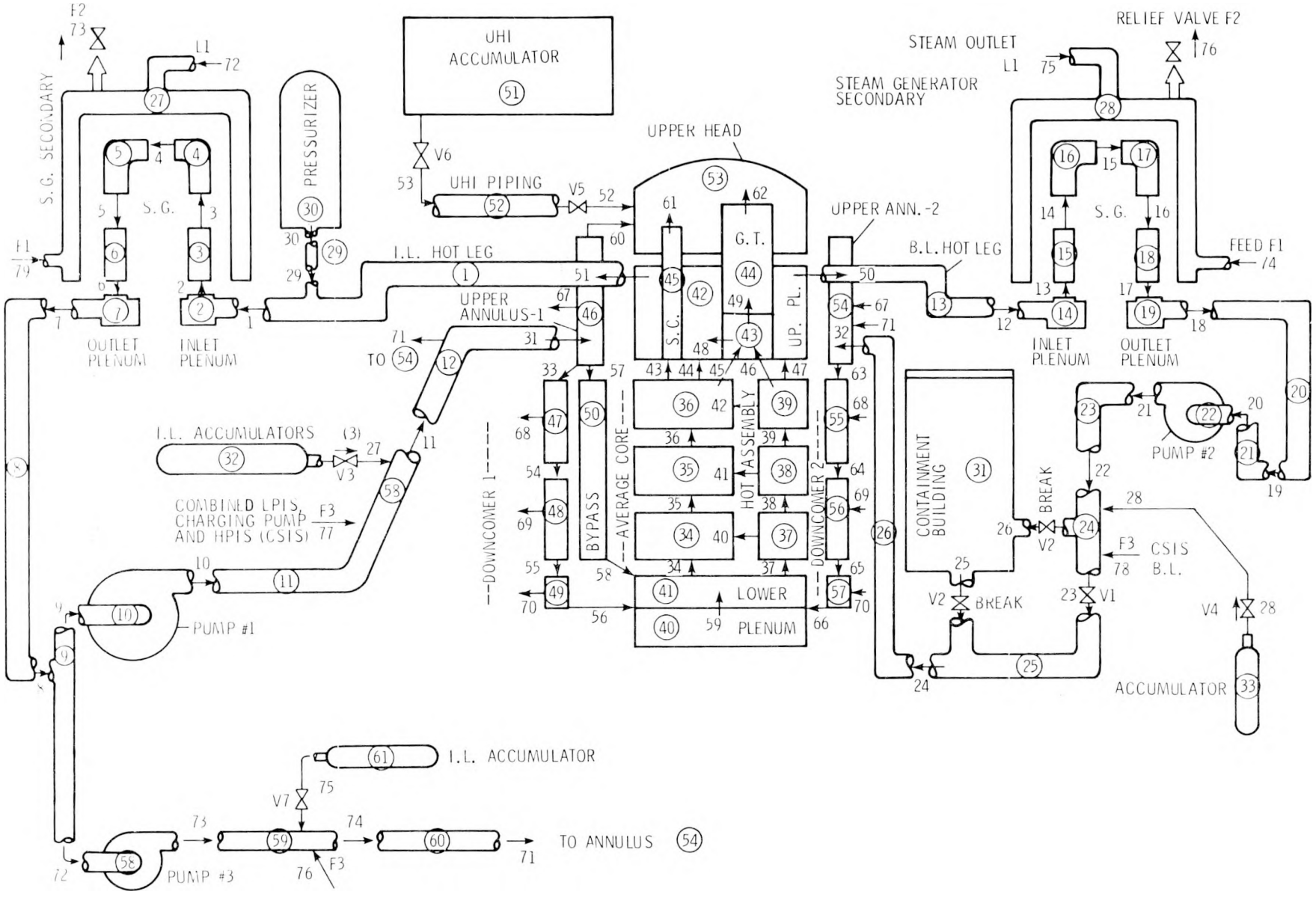

Figure 4-1. UHI, an Upper Head Injection Nodalization Scheme With Azimuthally Noded Downcomer

- Intact loop piping to the "right" upper annulus was connected to an additional pump, which in turn connects with the volume upstream of the original pump. This alteration was made to improve modeling of flows in the intact loop cold leg.

- Form loss friction factors in the cross flow junctions were changed from 0. to a more realistic value of 2., as recommended by Westinghouse.

- Various parameters in the description of the core fuel rods were revised.

The UHL nodalization was also employed in attempts to discover the sources of some suspect results observed in previous RELAP runs. The problem called UHL1 was run with RELAP4/MOD5 as described above: UHL1C is UHL1 with the water-packing option eliminated, and UHL1D is UHL1 with the potential energy correction described in Section 4.3 (the so-called "quick PE fix"). Addition of the Westinghouse slip and quench models, and modifications (connected with the treatment of flow reversal) to the RELAP solution method embodied in subroutine NIFTE, resulted in the calculation called UHL2. This problem was also run without the water-packing option (UHL2C). To provide more information on possible sources of unrealistic flow oscillations, two calculations (UHL2D and UHL2E) were run without the NIFTE modifications, with and without the potential energy correction. Finally, calculations with and without the water-packing option (UHL6 and UHL6C) were run with RELAP/MOD6 using the polytropic accumulator model. Table 4-I summarizes the distinguishing features of these calculations.

TABLE 4-I

UHI Calculations

Generic RELAP4/MOD5 Calculations:

UHL1:	Water-packing, new nodalization
UHL1C:	Water-packing correction off
UHL1D:	UHL1 with potential energy correction

Sandia-Modified MOD5 Calculations:

UHL2:	UHL1 with slip, quench, and NIFTE modifications
UHL2C:	UHL2 with water-packing correction off
UHL2D:	UHL2 without NIFTE modifications
UHL2E:	UHL2D with potential energy correction

RELAP4/MOD6 Calculations:

UHL6:	UHL1 with polytropic accumulators
UHL6C:	UHL6 with water-packing correction off

In the following, we will examine some of the results of these variations.

4.2.1 UHK1 vs UHL1

The UHK nodalization had the intact loop cold leg split downstream of the pump, with flow to both sides of the upper annulus (see last quarterly). By moving this split upstream of the pump, and inserting an additional pump, this closely coupled flow path was sufficiently disrupted that virtually all oscillations in flows to the upper annulus disappeared (Figures 4-2 and 4-3). The added flow resistance produced by the friction form loss factor changes reduced the magnitudes of cross-flows in both the upper annulus and the downcomer, as seen in Figures 4-4 through 4-7. Other aspects of this caluclation, not intimately connected with downcomer flow patterns (such as peak clad temperature and upper head draining), were not significantly affected by the changes in the plant model. We conclude that the changes made in the nodalization have been beneficial, in terms of reducing flow oscillations in the intact loop cold leg and downcomer regions.

4.2.2 UHL1 vs UHL1C and UHL1D

When we compared the results of calculations with and without the water-packing option in force, there seemed to be no significant trend to the differences, other than those that would obviously be expected; i.e., in areas where a large amount of water-packing occurred in UHL1, average qualities and liquid mass flows were different. However, both calculations produced flow and pressure oscillations at varying times and places, and neither set of results seemed clearly more believable.

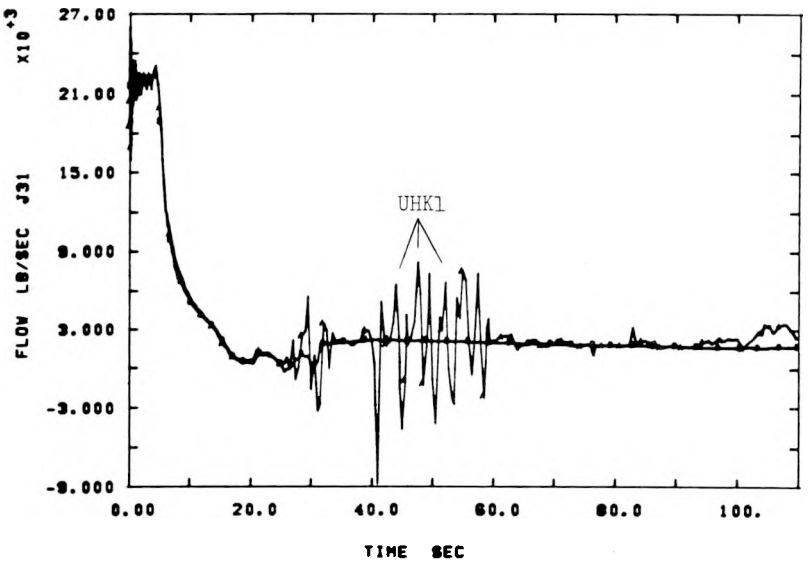

Figure 4-2. Cold Leg Flow (J31), Old (UHK1) vs New Nodalizations

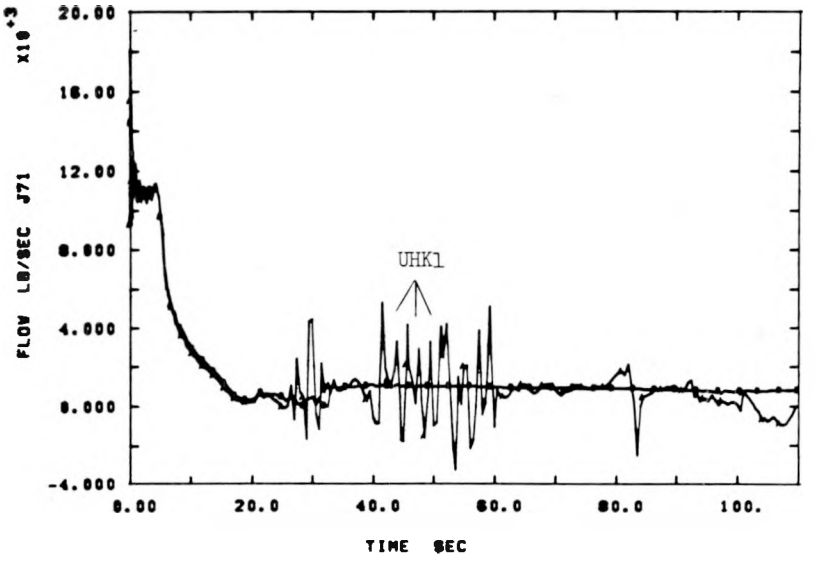

Figure 4-3. Cold Leg Flow (J71), Old (UHK1) vs New Nodalizations

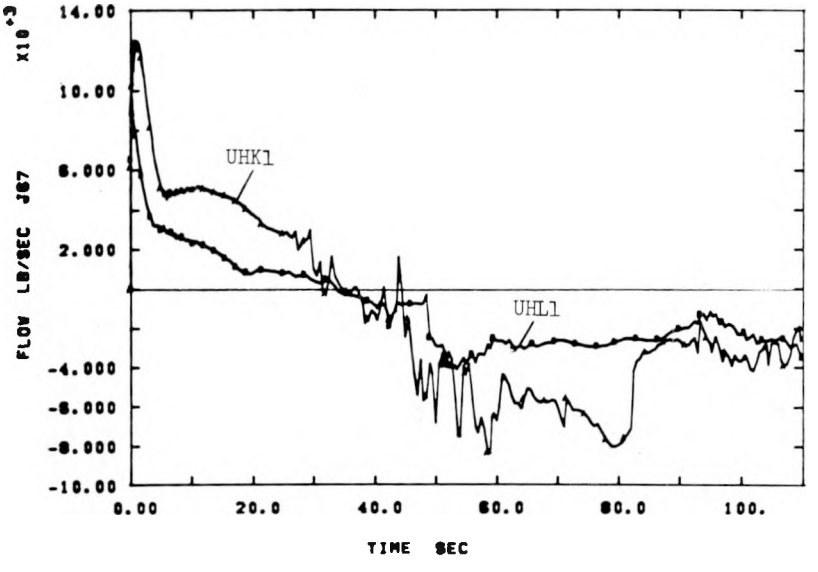

Figure 4-4. Upper Annulus Crossflow (J67), Old (UHK1) vs New Nodalizations

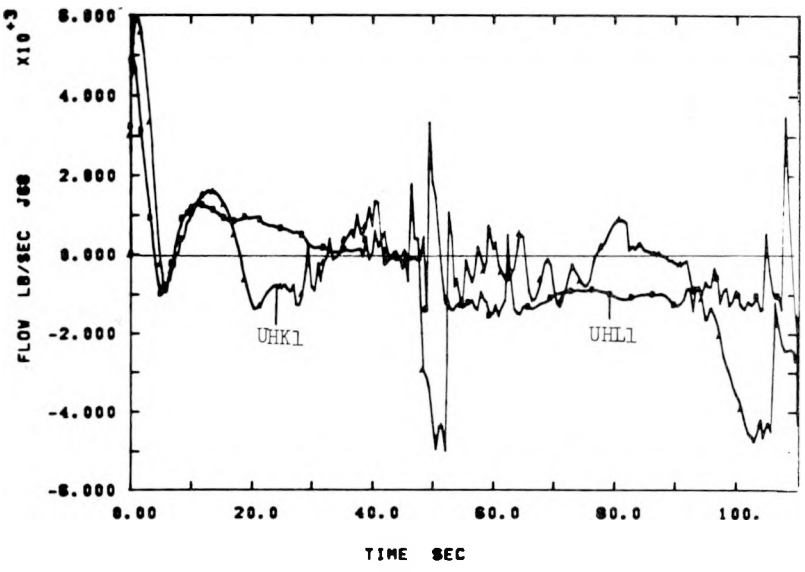

Figure 4-5. Downcomer Crossflow (J68), Old (UHK1) vs New Nodalizations

01

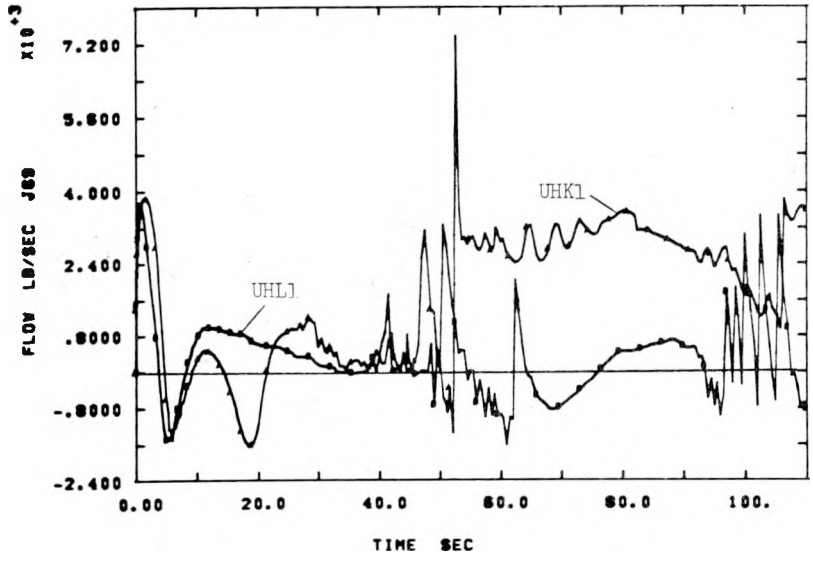

Figure 4-6. Downcomer Crossflow (J69), Old (UHK1) vs New Nodalizations

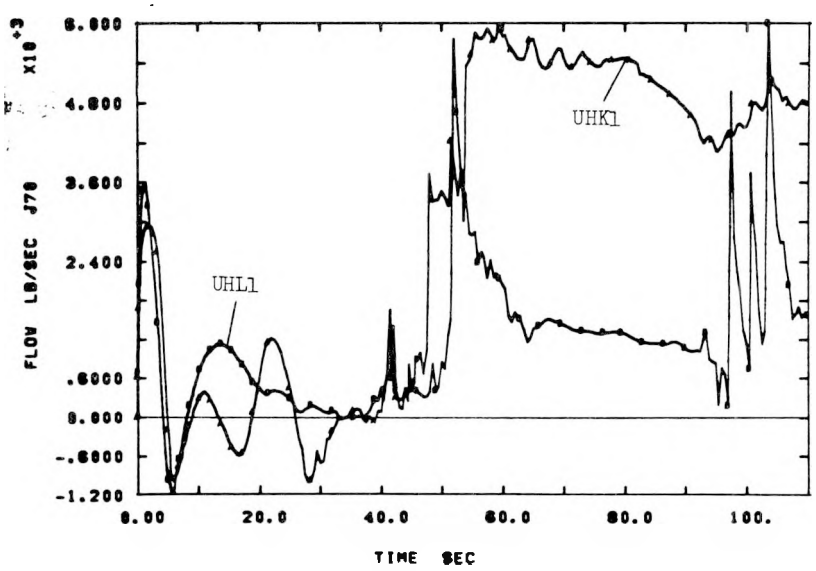

Figure 4-7. Downcomer Crossflow (J70), Old (UHK1) vs New Nodalizations

The effect of the potential energy correction on the UHL1 calculation was also quite localized in nature. Virtually the only significant differences occurred in the amount of liquid suspended in the primary volumes of the steam generators: see, for example, Figures 4-8 and 4-9.

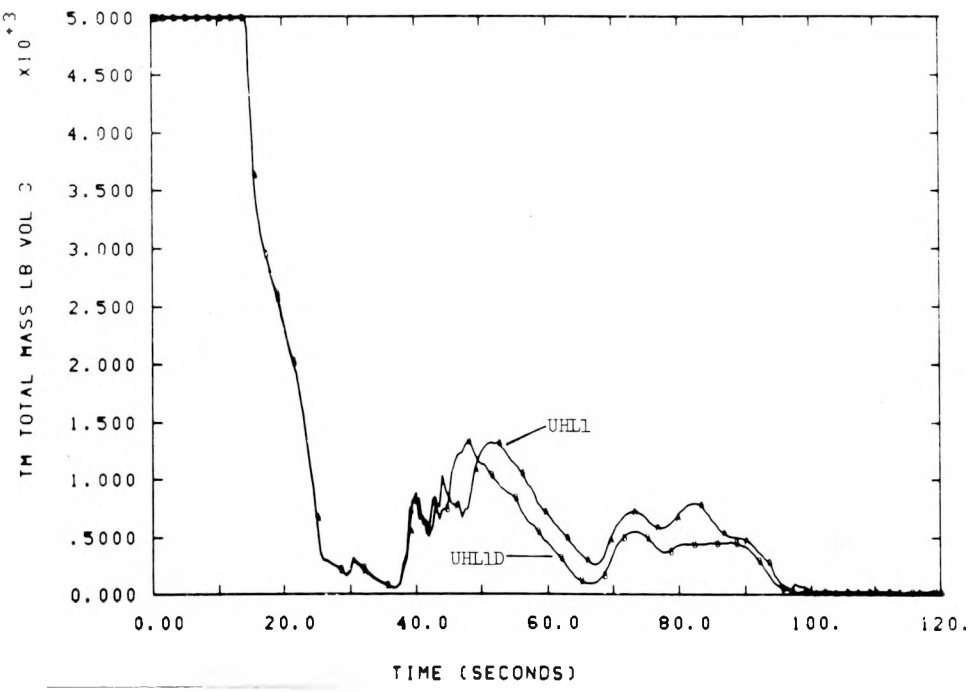

Figure 4-8. Total Mass in Steam Generator Primary, With (UHL1D) and Without Quick PE Fix

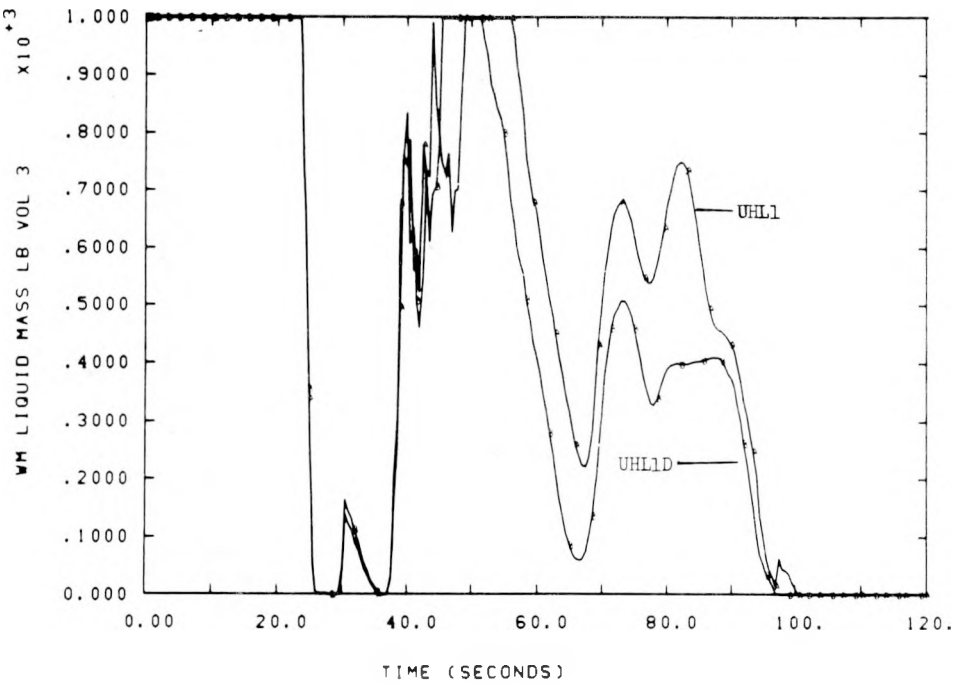

Figure 4-9. Liquid Mass in Steam Generator Primary, With (UHL1D) and Without Quick PE Fix

4.2.3 UHL1 vs UHL2

The addition of the new slip and quench models to RELAP/MOD5 had striking effects, only some of which were salutary. The differences in the slip and quench models produced significant changes in clad temperatures and fuel energy (Figures 4-10 through 4-13), and draining of the upper head proceeded at a higher rate in UHL2 (Figures 4-14 and 4-15). Pressure and temperature in the lowest average core volume were affected to a much smaller degree (Figures 4-16 and 4-17).

However, the new slip model has introduced problems of unrealistic flow oscillations, this time in downcomer junctions (Figures 4-18 and 4-19). One effect of these changes in the flows may be seen in Figures 4-20 and 4-21, showing the behavior during lower plenum refill. The refilling of the lower volume of the lower plenum, in particular, is considerably more oscillatory, and significantly delayed.

4.2.4 UHL2 vs UHL2C

Figure 4-22 demonstrates one of the poorly understood effects of the water-packing correction, and the way in which it interacts with the new slip and quench models. The phenomenon of increased mass in the steam generator primaries was noticed in the corresponding UHL1 calculations, but the difference was much smaller than with the new models. For example, in UHL1 the total mass in Volume 3 (at times later than 50 sec) was calculated to be about 1.5 times the

corresponding value in UHL1C, as opposed to the ratio of 3:1 shown in Figure 4-22. Figures 4-23 and 4-24, when compared with corresponding plots from UHL1 and UHL1C, also demonstrate that the new slip and quench models accentuate the effects of the water-packing correction. The difference between volume 40 refill times in UHL1 and UHL1C was approximately 5.7 seconds, in contrast to about 10 seconds for the UHL2 vs UHL2C comparison.

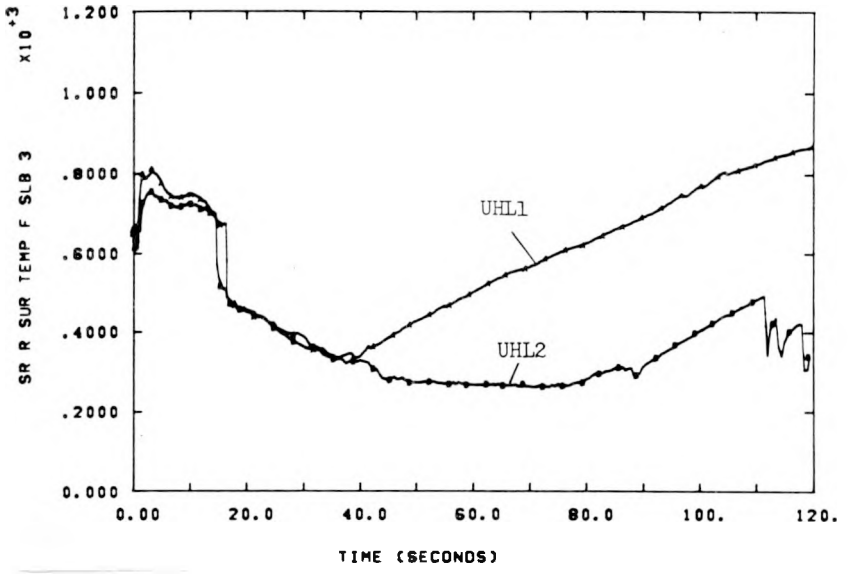

Figure 4-10. Temperature (at Slab 3), With and Without (UHL1) Slip and Quench Modifications

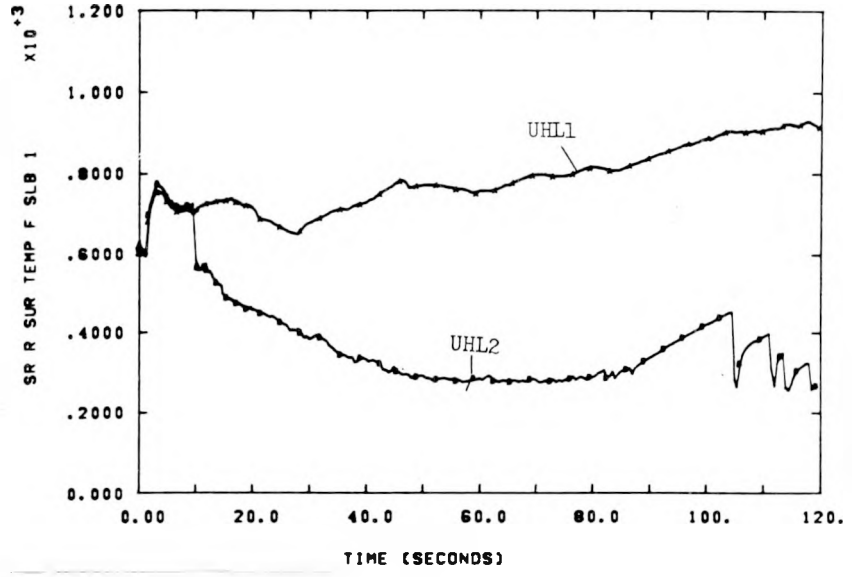

Figure 4-11. Temperature (at Slab 1), With and Without (UHL1) Slip and Quench Modifications

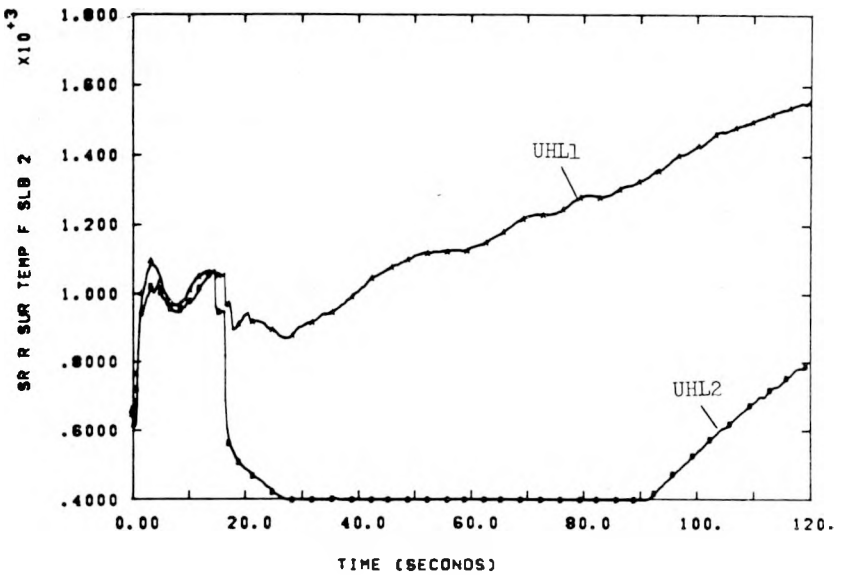

Figure 4-12. Temperature (at Slab 2), With and Without (UHL1) Slip and Quench Modifications

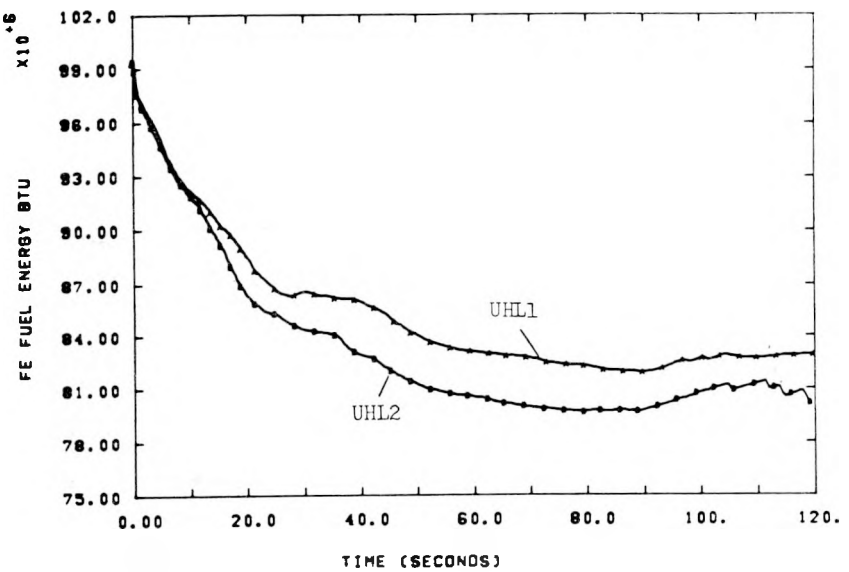

Figure 4-13. Fuel Stored Energy, With and Without (UHL1) Slip and Quench Modifications

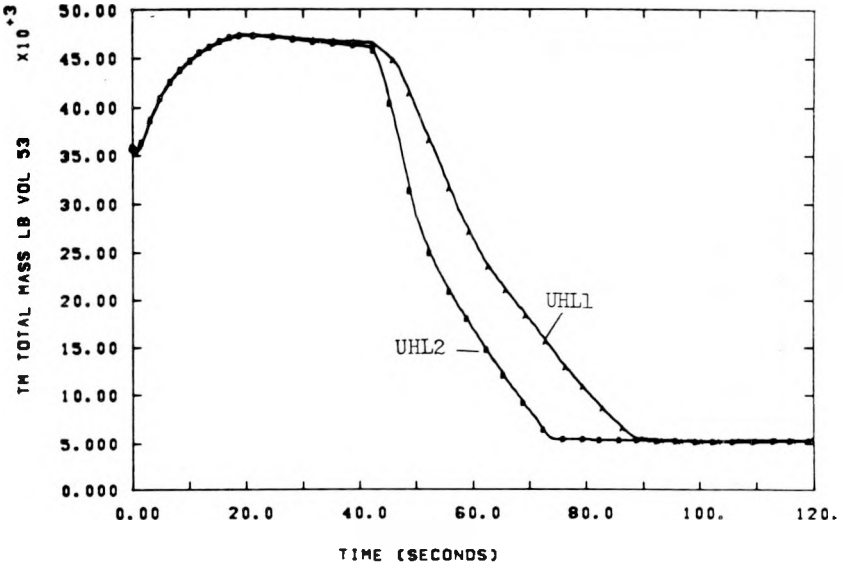

Figure 4-14. Total Mass in Upper Head With and Without (UHL1) Slip and Quench Modifications

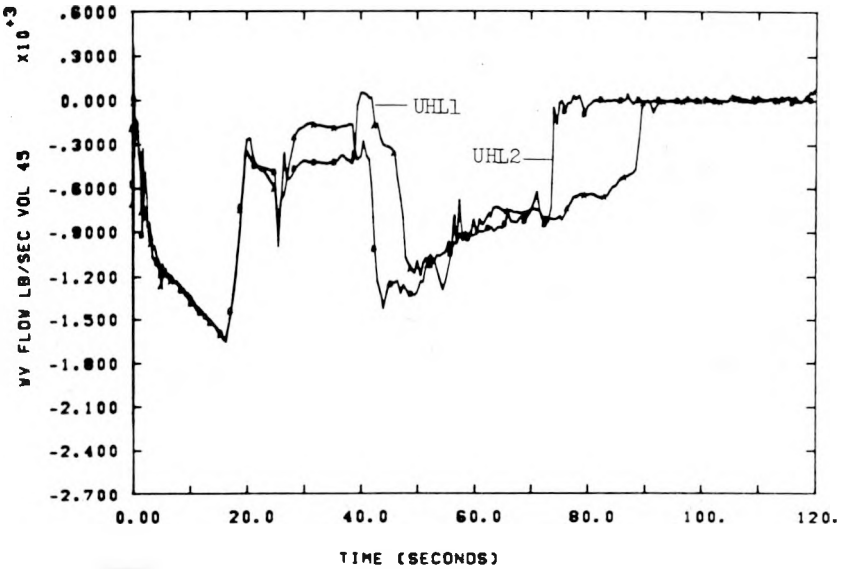

Figure 4-15. Upper Head Draining With and With (UHL1) Slip and Quench Modifications

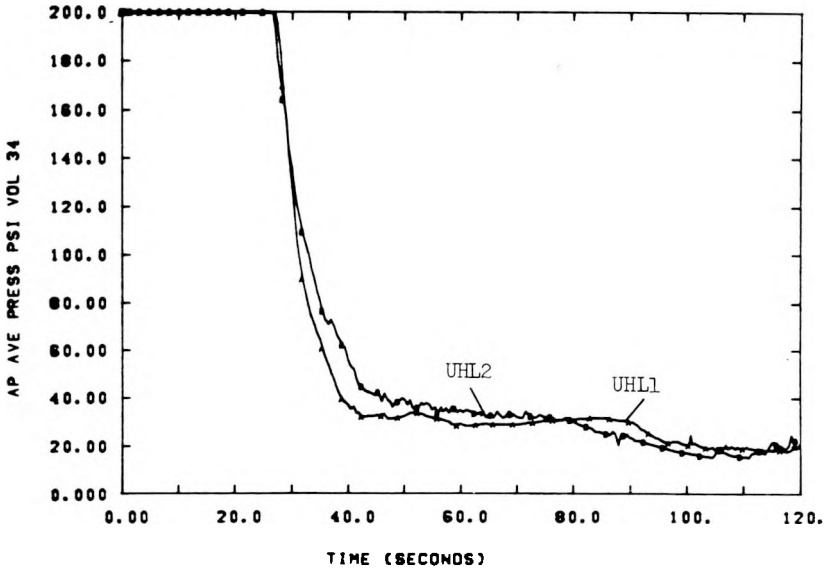

Figure 4-16. Average Pressure at Lowest Core Volume, With and Without (UHL1) Slip and Quench Modifications

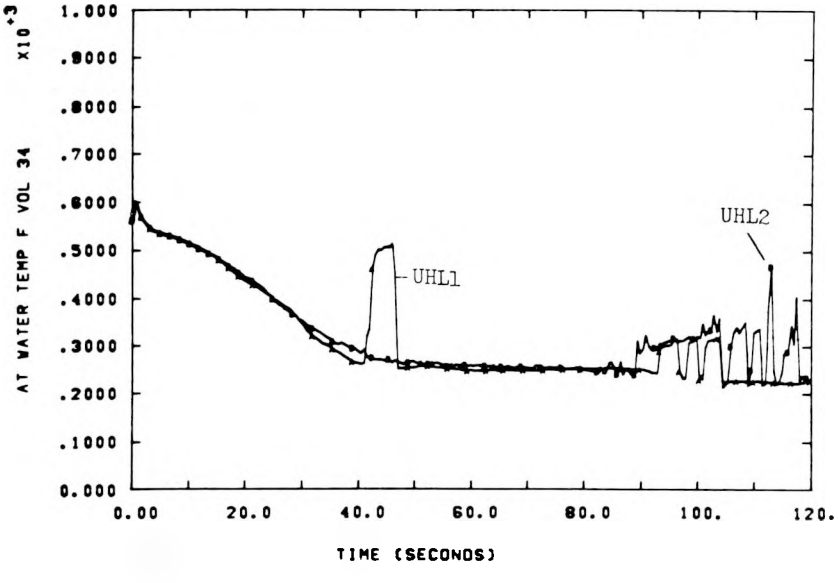

Figure 4-17. Water Temperature at Lowest Core Volume, With and Without (UHL1) Slip and Quench Modifications

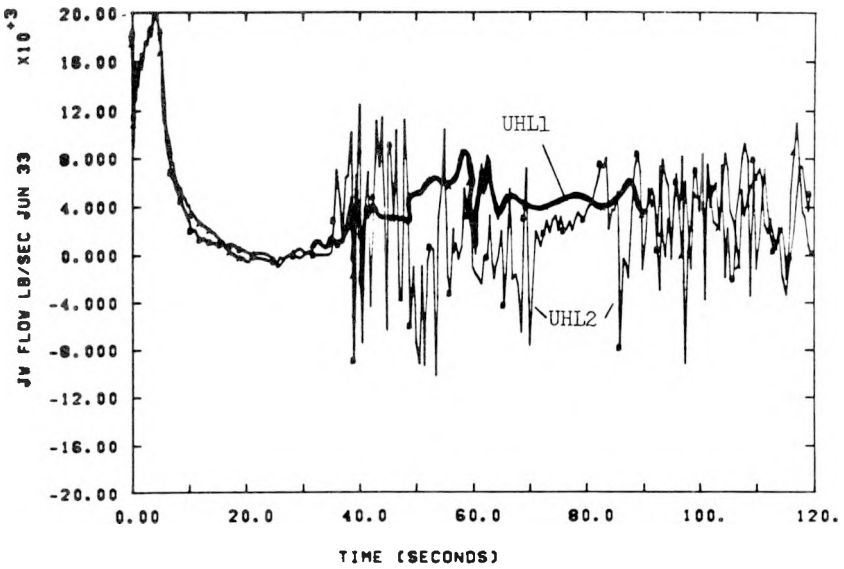

Figure 4-18. Downcomer Flow (J33), With and Without (UHL1) Slip and Quench Modifications

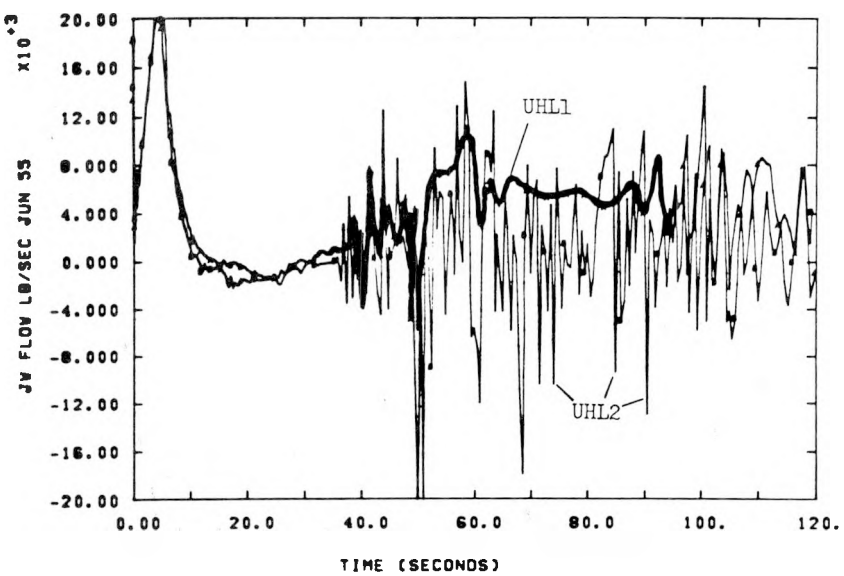

Figure 4-19. Downcomer Flow (J55), With and Without (UHL1) Slip and Quench Modifications

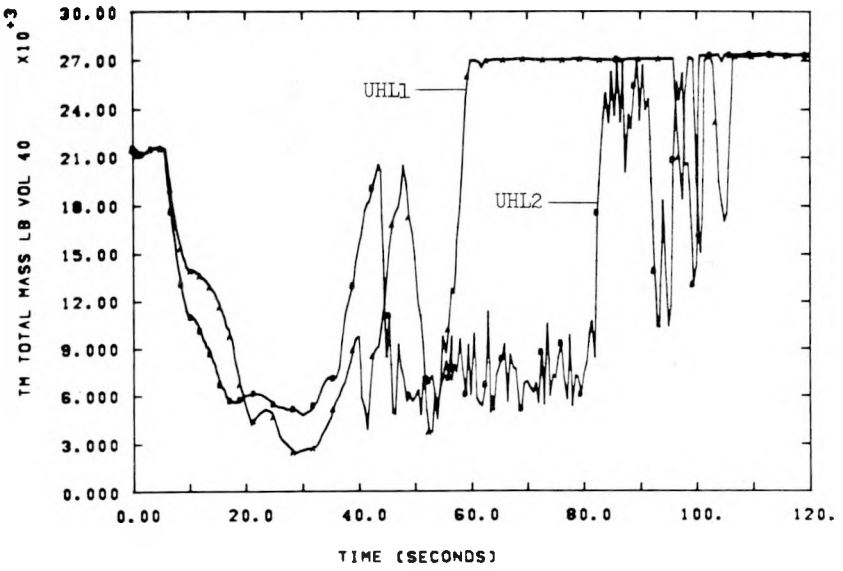

Figure 4-20. Refilling of Lower Lower Plenum, With and Without (UHL1) Slip and Quench Modifications

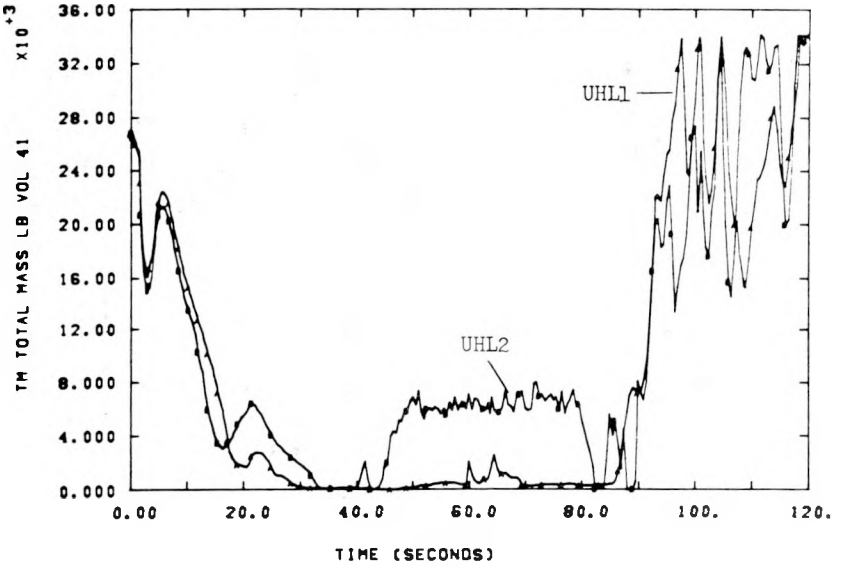

Figure 4-21. Refilling of Upper Lower Plenum, With and Without (UHL1) Slip and Quench Modifications

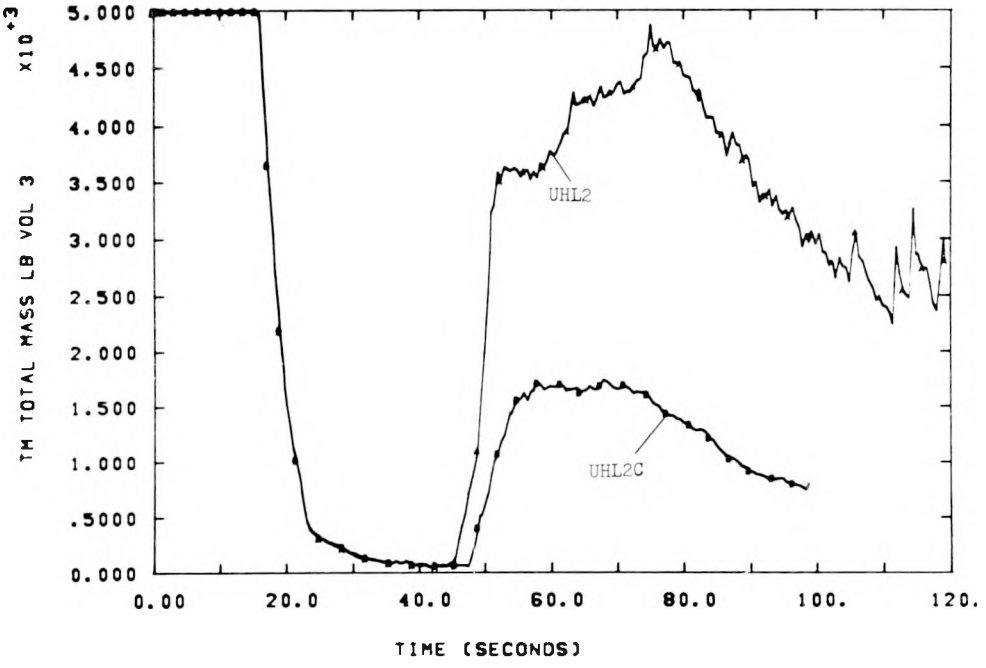

Figure 4-22. Total Mass (Vol 3) With Slip and Quench Modifications, With and Without (UHL2C) Water-Packing Correction

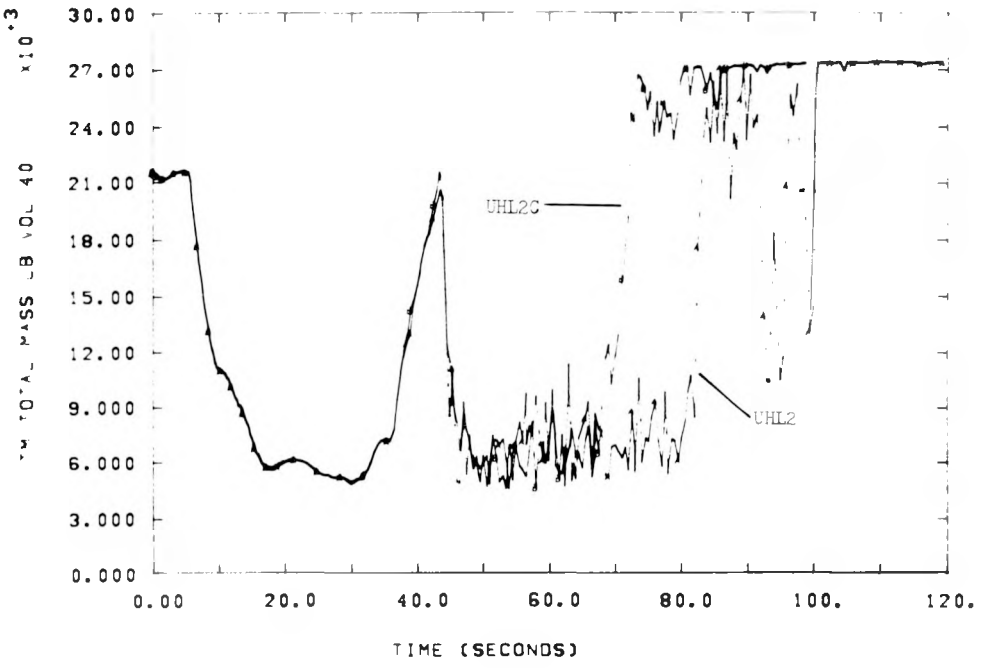

Figure 4-23. Total Mass in Lower Lower Plenum, With Slip and Quench Modifications, With and Without (UHL2C) Water-Packing Correction

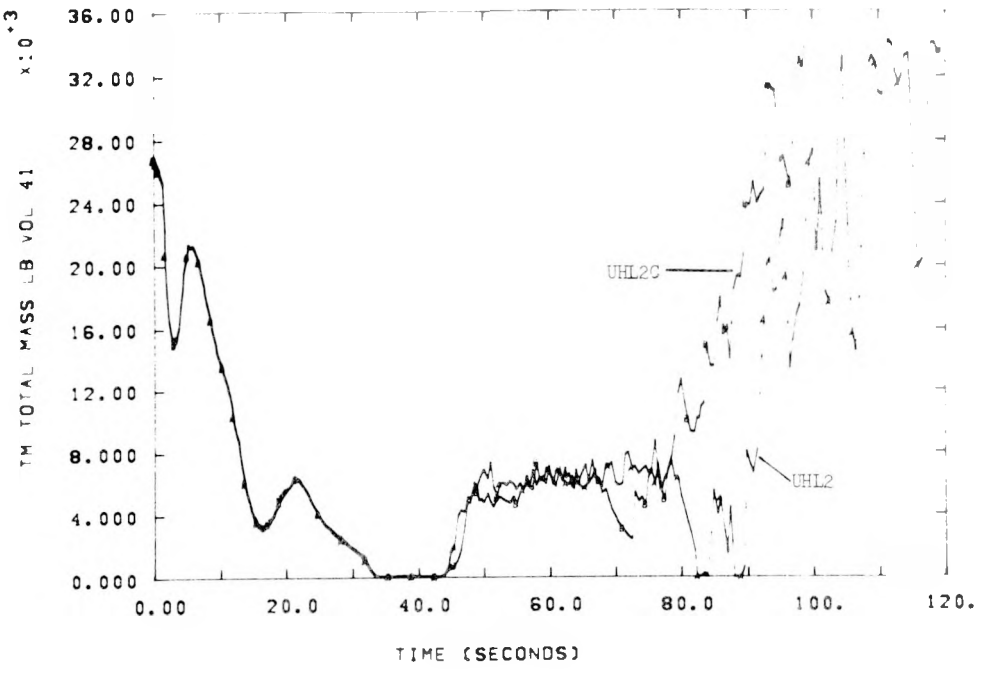

Figure 4-24. Total Mass in Upper Lower Plenum, With Slip and Quench Modifications, With and Without (UHL2C) Water-Packing Correction

4.2.5 UHL2D and UHL2E

As a part of the effort to determine the source, or sources, of flow oscillations which we regard as unrealistic, two calculations were run without the NIFTE recycle modifications, but with the new slip and quench models. The two calculations differed only in whether or not the potential energy correction was used. Figure 4-25 again shows that the new models exaggerate the effects of many of the variations in calculational techniques (compare with Figure 4-9). The pair of calculations (see Figure 4-26) also demonstrate that the changes made in NIFTE were not the source of the problems associated with two-phase flow in the UHL2 series. We, therefore, suspect that some basic inconsistency in the new slip modeling technique is responsible for our difficulties. Work will continue to pursue the resolution of this question.

4.2.6 UHL1 vs UHL6

The expansion of gas in the accumulators can be treated with a polytropic model in MOD6; i.e.,

$$PV^{\gamma} = \text{constant}$$

is the equation governing the expansion of gas (nitrogen) in the accumulators. For an adiabatic expansion of air in the accumulator, γ is 1.4 at room temperature. In MOD5, the requirement that liquid and gas be at the same temperature in an accumulator volume is essentially equivalent to an isothermal expansion with $\gamma = 1.0$ (due to the large thermal inertia of the liquid). A value of $\gamma = 1.22$ was used for the polytropic exponent in the MOD6 calculation UHL6. This value is based on Westinghouse experimental data and lies roughly between the adiabatic ($\gamma = 1.4$) and isothermal ($\gamma = 1.0$, as in the MOD5 calculation, UHL1) extremes.

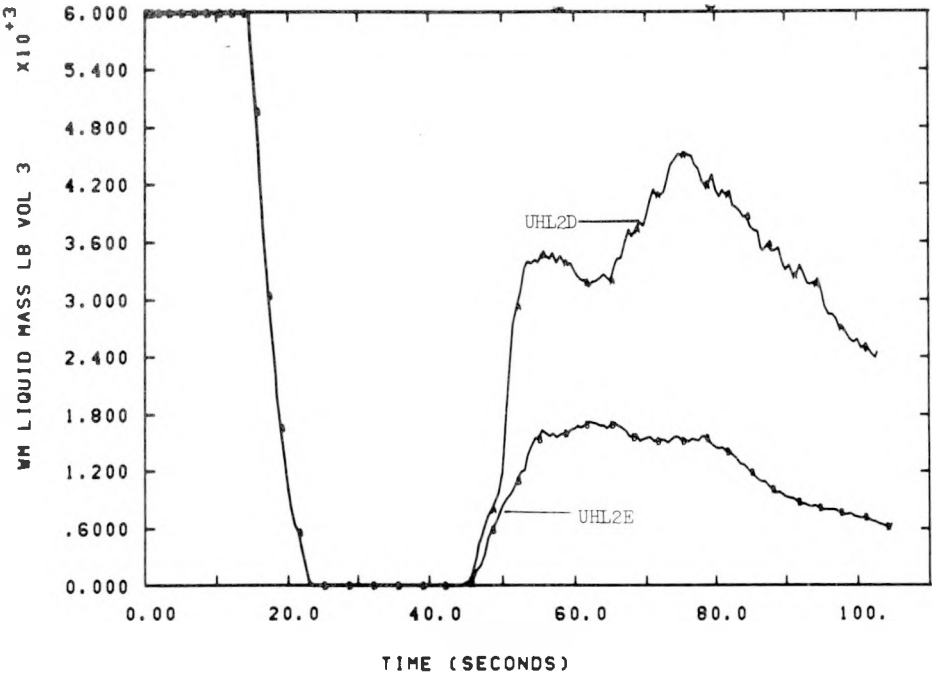

Figure 4-25. Liquid Mass in Steam Generator Primary, Modified Code but Without NIFTE, With and Without (UHL2D) Quick PE Fix

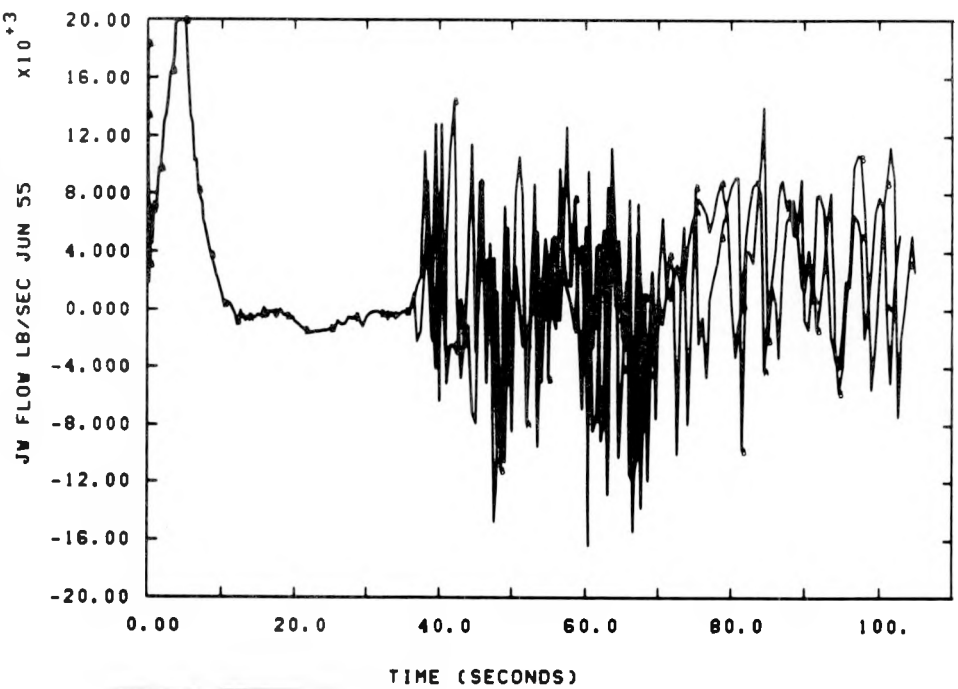

Figure 4-26. Downcomer Flow (J55), Modified Code but Without NIFTE, With (UHL2E) and Without (UHL2D) Quick PE Fix

From Figures 4-27 and 4-28, it may be seen that the effect of the polytropic expansion model on flows from the accumulator is not very great. Upper head draining occurs slightly more rapidly in the MOD6 calculation (Figures 4-29 and 4-30). Pressures and temperatures in the average core volumes (e.g., Figures 4-31 and 4-32) were calculated to be quite similar, with the exception of an early, anomalous dryout period (about 40 seconds in Figure 4-32) not seen in any other calculations. This is possibly due to a short cessation of support column flow, seen only in UHL1. The filling of the lower plenum volumes, however, was significantly different as calculated by MOD 5 and MOD6 (Figures 4-33 and 4-34); for the lower lower plenum volume, the MOD6 calculation delayed the filling by almost 50 seconds.

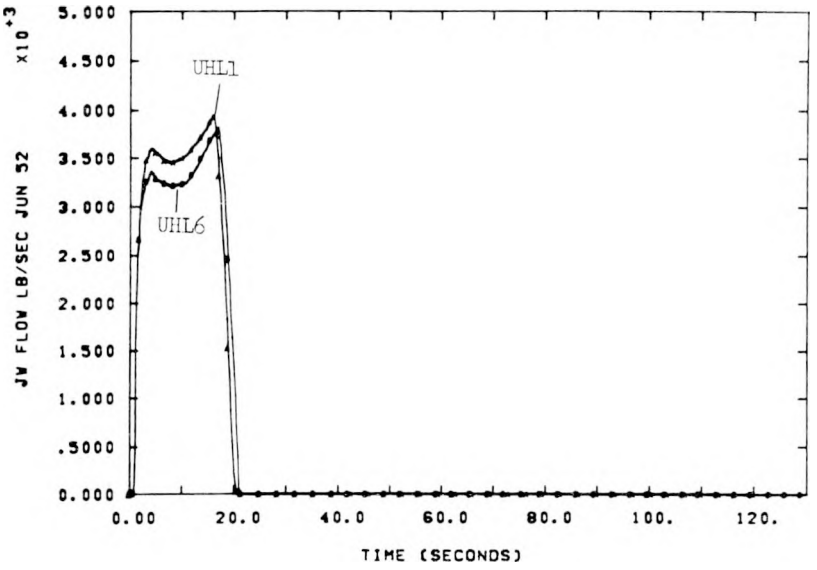

Figure 4-27. UHI Accumulator Flow (J52), New Nodalization, MOD5 (UHL1) vs MOD6 (UHL6, Polytropic Expansion Model)

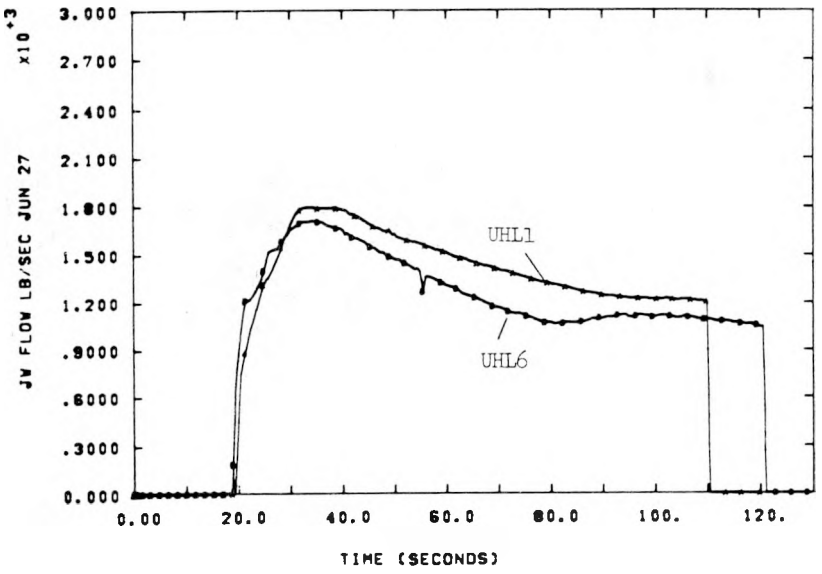

Figure 4-28. Cold Leg Accumulator Flow (J27), New Nodalization, MOD5 (UHL1) vs MOD6 (UHL6, Polytropic Expansion Model)

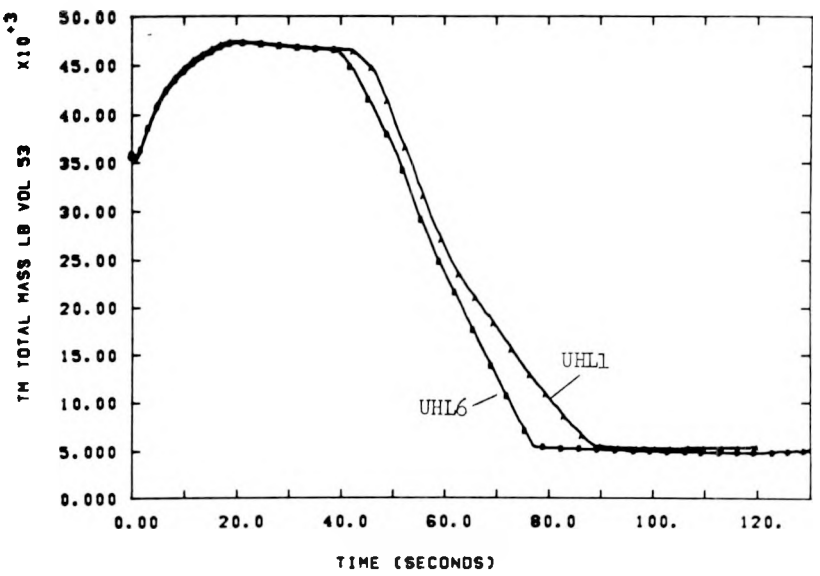

Figure 4-29. Upper Head Mass, New Nodalization, MOD5 (UHL1) vs MOD6 (UHL6, Polytropic Expansion Model)

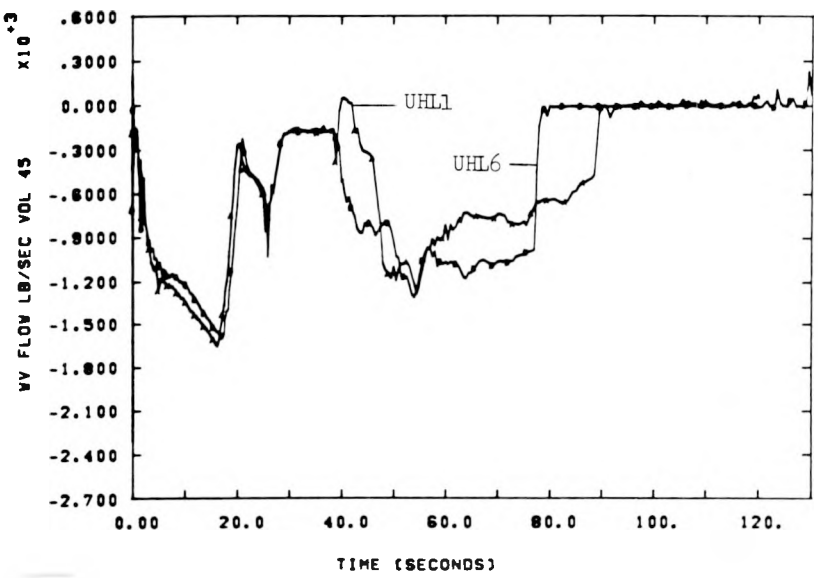

Figure 4-30. Draining Upper Head, New Nodalization, MOD5 (UHL1) vs MOD6 (UHL6, Polytropic Expansion Model)

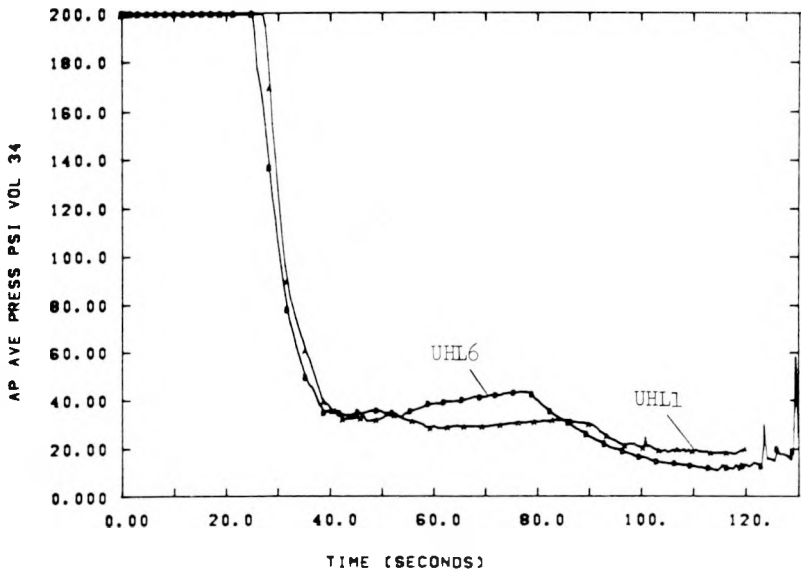

Figure 4-31. Average Pressure at Lowest Core Volume, New Nodalization, MOD5 (UHL1) vs MOD6 (UHL6, Polytropic Accumulators)

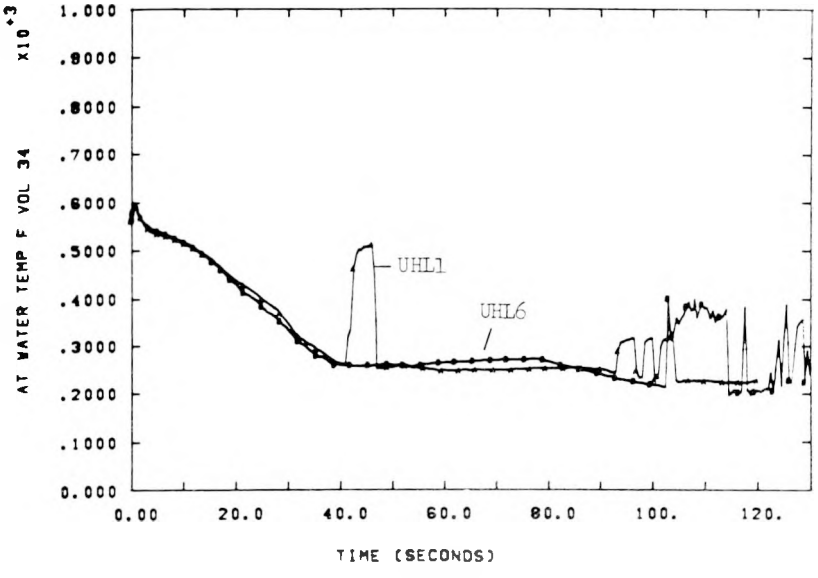

Figure 4-32. Water Temperature at Lowest Core Volume, New Nodalization, MOD5 (UHL1) vs MOD6 (UHL6, Polytropic Accumulators)

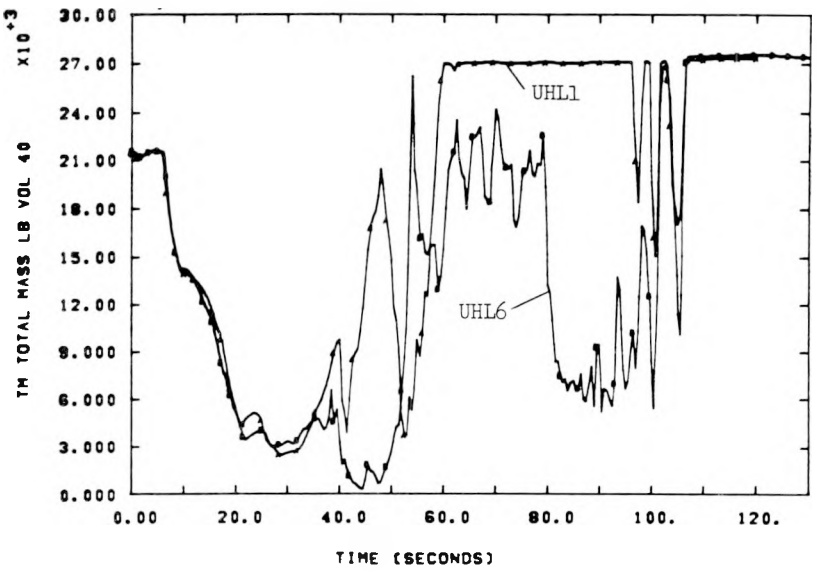

Figure 4-33. Mass in Lower Lower Plenum, New Nodalization, MOD5 (UHL1) vs MOD6 (UHL6, Polytropic Expansion Model)

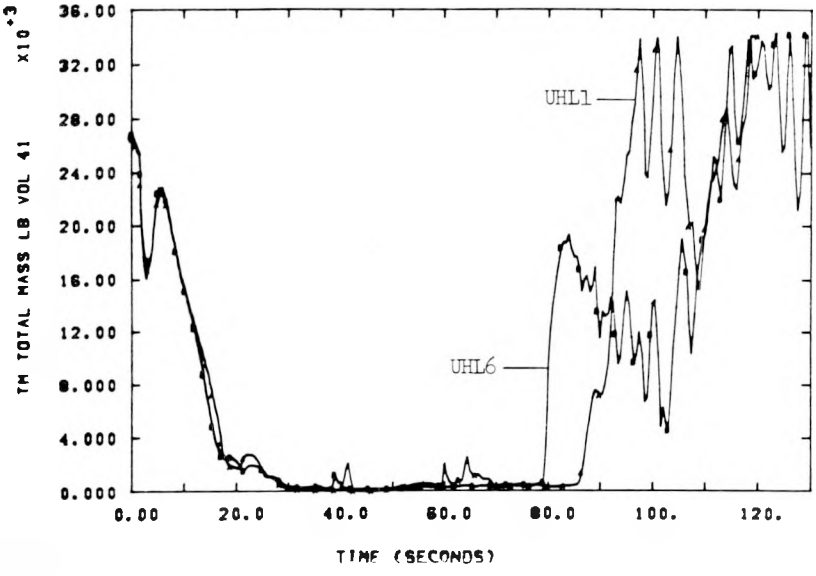

Figure 4-34. Mass in Upper Lower Plenum, New Nodalization, MOD5 (UHL1) vs MOD6 (UHL6, Polytropic Expansion Model)

Some other large differences between MOD5 and MOD6 are due to the differences in heat transfer modeling. Figure 4-35 shows quenching patterns in the core for the UHL1, UHL2, and UHL6 calculations. In that figure, the extreme left column of cells under each heading represents the slabs associated with the hot core assembly. We see that MOD 6 predicts early and complete quenching in the core, but no quenching for times greater than about 30 seconds. More of the core is quenched during most of the calculation in UHL2 than in the other two calculations. The results are shown in Figures 4-36 and 4-37 (see also Figures 4-10 and 4-12), in which temperatures display an early decrease compared to UHL1. The resulting MOD6 temperature history at the hot spot lies roughly midway between those from the UHL1 and UHL2 calculations.

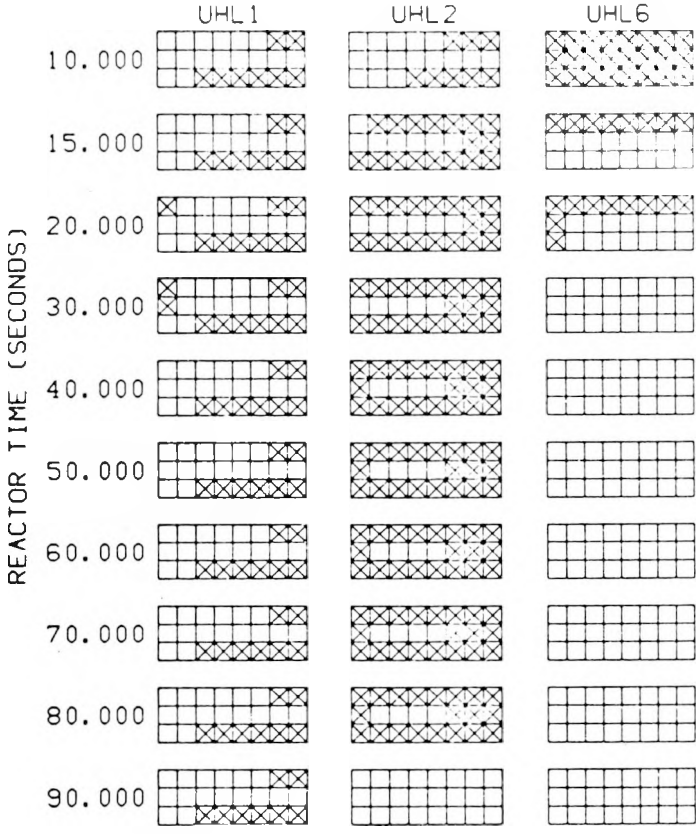

Figure 4-35. Core Quench Maps

We observed, when comparing the results of UHL6 and UHL6C, that the only effects of removing the water-packing correction were of a nature similar to those seen in the earlier comparisons of UHL1 to UHL1C and UHL2 to UHL2C. A final observation is that the MOD6 version of RELAP4 runs, at least for the UHL series of problems, more slowly than MOD5--sometimes considerably so (Figure 4-38).

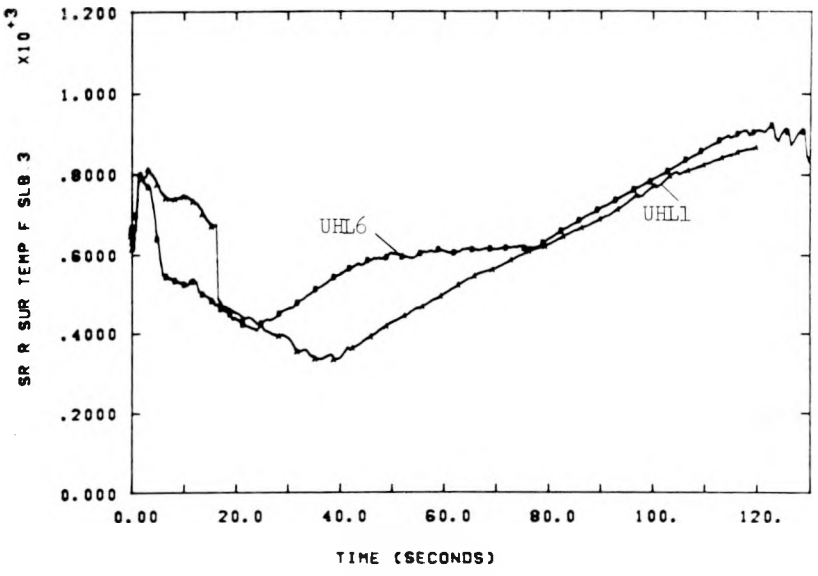

Figure 4-36. Temperature (at Slab 3), New Nodalization, MOD5 (UHL1) vs MOD6 (UHL6, Polytropic Expansion Model)

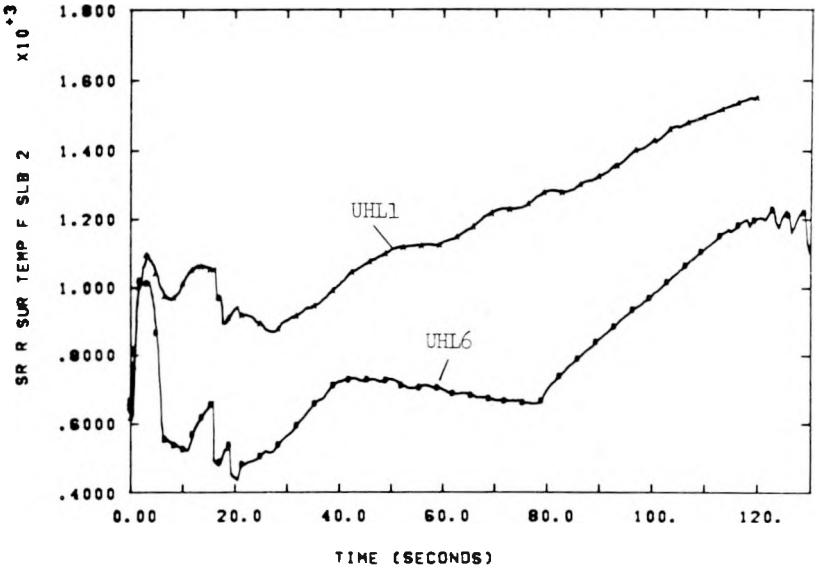

Figure 4-37. Temperature (at Slab 2), New Nodalization, MOD5 (UHL1) vs MOD6 (UHL6, Polytropic Expansion Model)

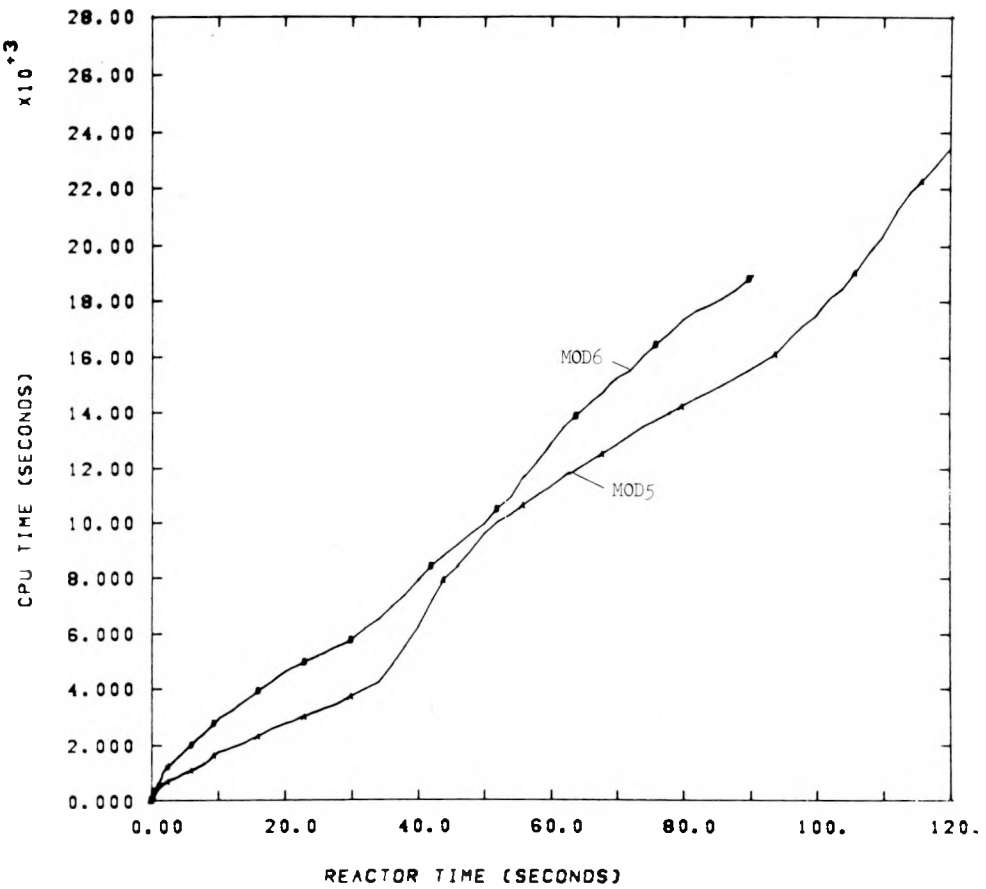

Figure 4-38. Computer Time for Two Modifications of RELAP4 Analytical Program

4.3 Potential Energy Correction

In the course of searching for the source, or sources, of problems appearing in some of our calculations, we became convinced that a fundamental error existed in the treatment of the energy equation. This equation contains quantities representing the transport of specific enthalpy, kinetic energy, and gravitational potential energy for flows into and out of volume nodes. Our interpretation of the code led us to believe that, in the case when actual flow directions are opposite the normal or logical flow directions, these terms were being interchanged among inlets and outlets in an incorrect way. Therefore, we performed a very simple calculation with two identical volumes, one at higher elevation than the other, connected by two frictionless junctions with the same logical flow orientation. The problem is started with one positive and one negative initial flow, proceeding as if a simple circulating flow were being calculated. Our predictions of the results of the error described above were that the fluid volumes would either heat and increase in pressure or cool and decrease in pressure, depending on whether the normal flow directions were down or up.

Some important conditions of the problem were 10 ft^3 volumes filled with water at 15 psi and 80 °F, an elevation difference of 10 ft, and initial flows of 6000 lbm/sec. Other conditions were chosen so that no frictional or form losses would have an effect. Under these conditions we expected, and RELAP calculated, a temperature change in both volumes of about 1.25 °F at the end of 10 seconds. This was accomplished with no observable change in mass flow rate, and so could go on indefinitely.

The evaluation of the energy equation difference analog may be thought of as a sum of one-dimensional spatial integrations over the volume nodes, done in the direction of positive normal flows. A modification taking account of this fact was made, and the test problem described above was recalculated. Apart from a small ($\sim 6 \times 10^{-4}$%) change in temperature as the code adjusts conditions for the difference in volume elevations, there was no observable alteration in initial conditions at the end of 10 seconds of problem time. Figures 4-39 and 4-40 demonstrate the results of this correction. The current form of the modification to RELAP has been termed the "quick PE fix," in recognition of the fact that a logically cleaner way of accomplishing its result exists.

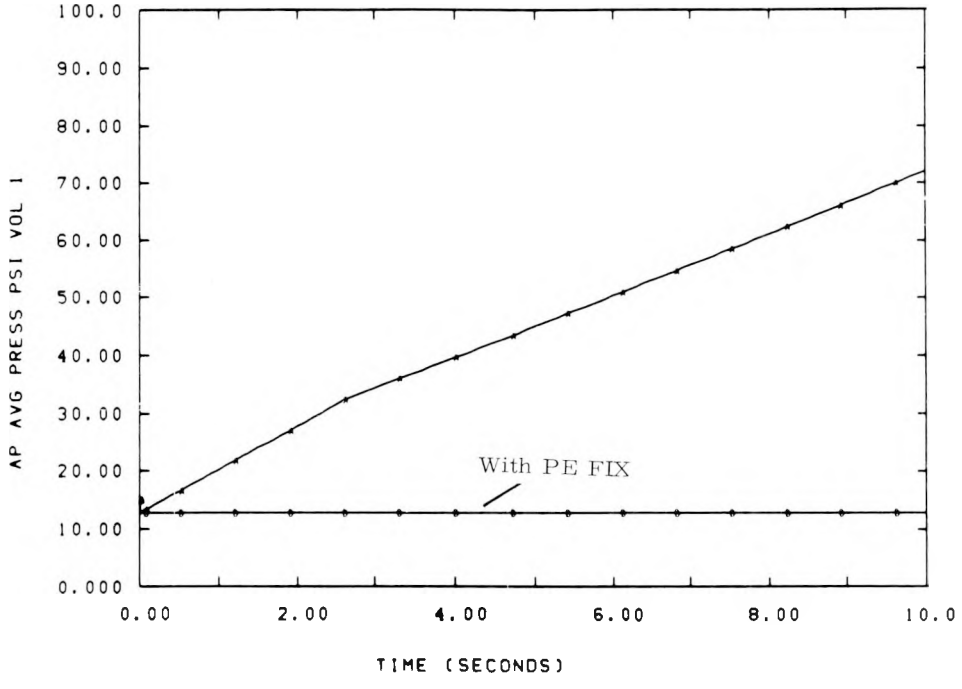

Figure 4-39. Average Pressure in Two-Volume Test With and Without Potential Energy "fix"

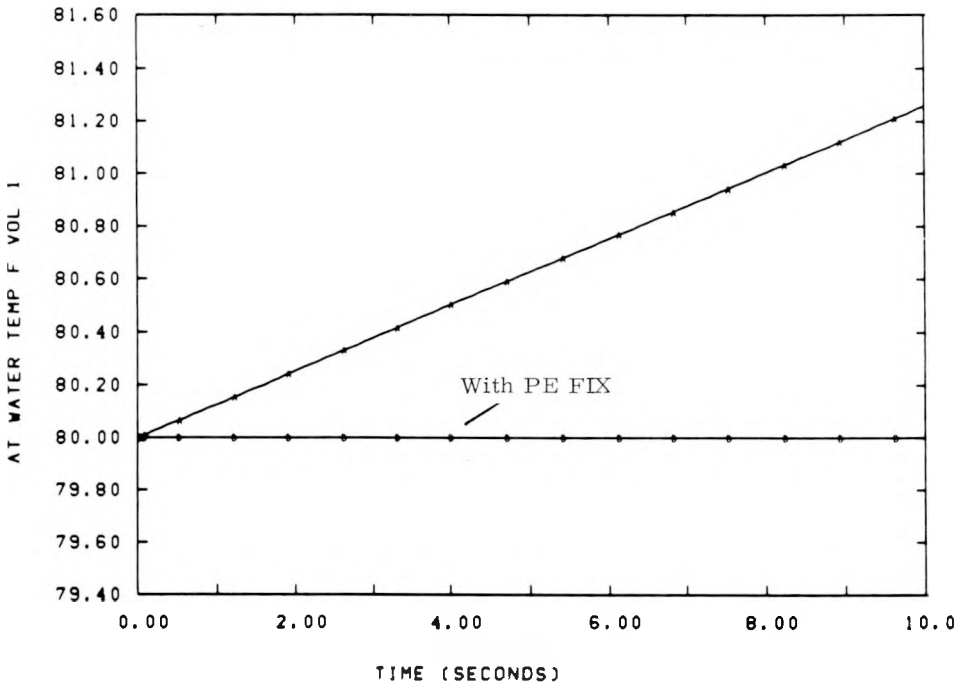

Figure 4-40. Water Temperature in Two-Volume Test, With and Without Potential Energy "fix"

4.4 Improved Inertial Flow Estimator

A set of calculations has been performed for a two-volume, one-junction problem intended to test the polytropic accumulator option in the MOD6 version of RELAP. The calculations were run with various combinations of inertial and Henry-Fauske-Homogeneous-Equilibrium (HF-HEM) critical flow models, compressible and incompressible fluid models, and three values of the ratio of specific heats for the air in the accumulator (1.0, 1.22, and 1.4). Initial pressure and temperature in the accumulator were about 450 psi and 80°F, so that very little difference was expected in compressible versus incompressible results. The junction empties into a moist-air-filled volume which is very large compared to the accumulator, making an analysis based on the assumptions of quasi-steady, incompressible flow easy to obtain. A valve on the junction opens in 10.5 seconds, providing an initially time-dependent flow area.

The RELAP results and the analytical results all agreed well whenever the junction flow was modeled in RELAP as inertial (see, for example Figures 4-41 through 4-43). However, the use of the HF-HEM model produced a variety of physically unrealistic phenomena, such as choking and alternating of flow direction, very rapid cooling (to about 32°F) of the accumulator, and emptying of the accumulator in roughly two thirds of the realistic time.

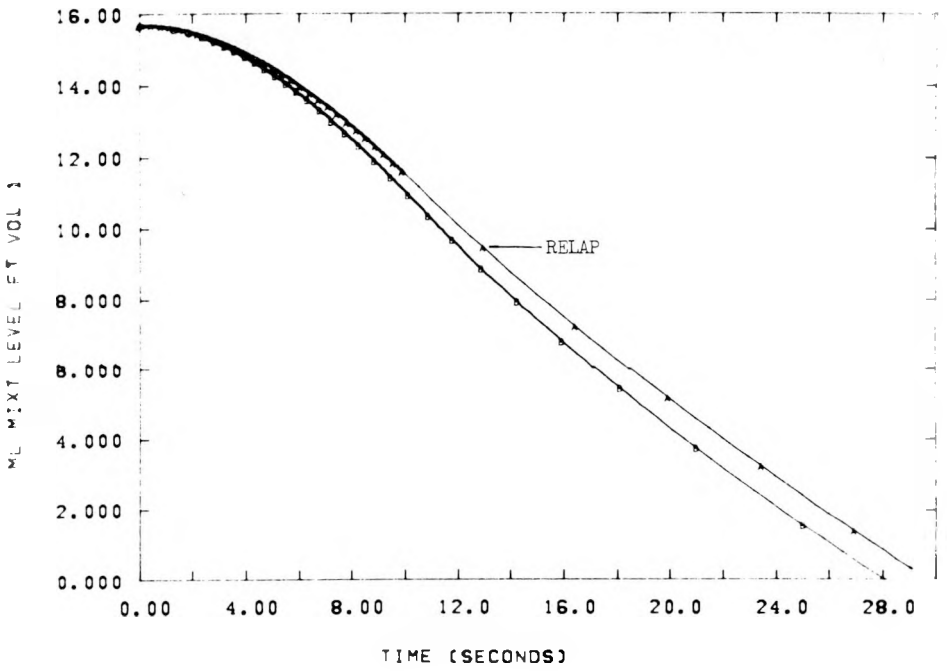

Figure 4-41. Mixture Level in Polytropic Accumulator Tests, Analytical vs RELAP

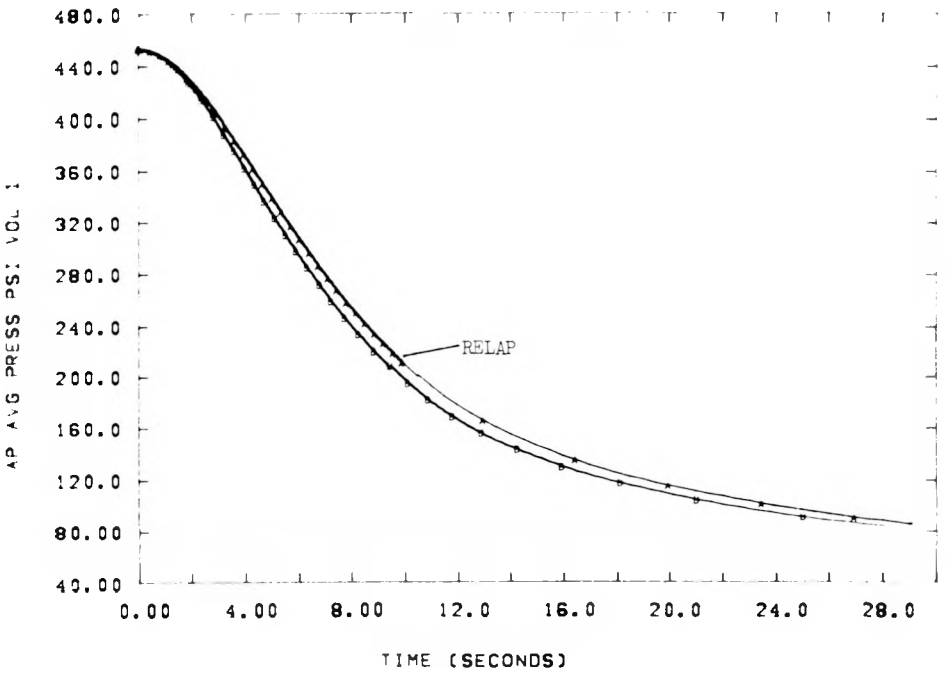

Figure 4-42. Average Pressure in Polytropic Accumulator Tests, Analytical vs RELAP

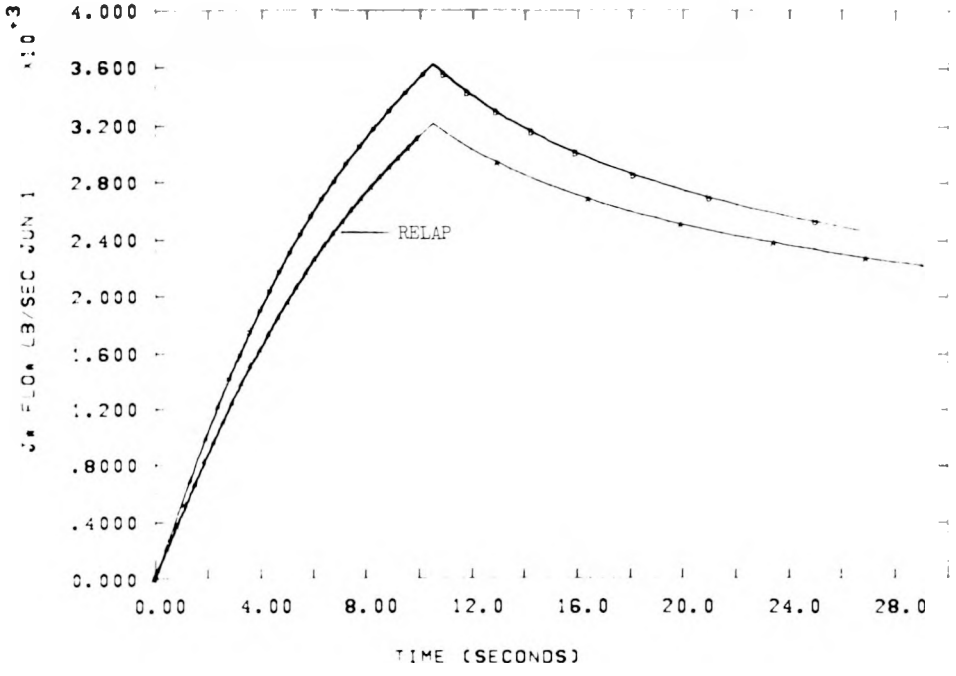

Figure 4-43. Flow in Polytropic Accumulator Tests, Analytical *vs* RELAP

The source of the aforementioned difficulties was found to be an inaccurate estimate of mass flow rate for use in the solution of the flow equations. Briefly, the flow change estimate being used was

$$\delta W = \frac{\delta t}{I}\left[\Delta p - KW|W|\right] ,$$

where W is the old mass flow rate, δt the timestep, Δp an effective pressure drop, and K some friction loss factor. This estimate can be reasonably accurate only if the difference method being used is explicit. When one writes a second-order accurate (roughly) difference approximation to the explicit-implicit scheme, the following estimate for the flow increment is obtained:

$$\delta W = \frac{\delta t}{I}\left[\Delta p - KW|W|\right]\left[1 + \frac{2\delta t}{I} K\alpha|W|\right]^{-1} ,$$

where α is the "implicitness factor."

The use of this latter estimate removed the peculiar results in the HF-HEM calculations alluded to earlier, and produced good agreement with other results. After the first time step, ratios of the old to new flow estimates ranged from about -2×10^4 to 20 over the very early part of the calculation. Figures 4-44 through 4-46 display RELAP results for one of the calculations as computed with and without the improved flow increment estimate.

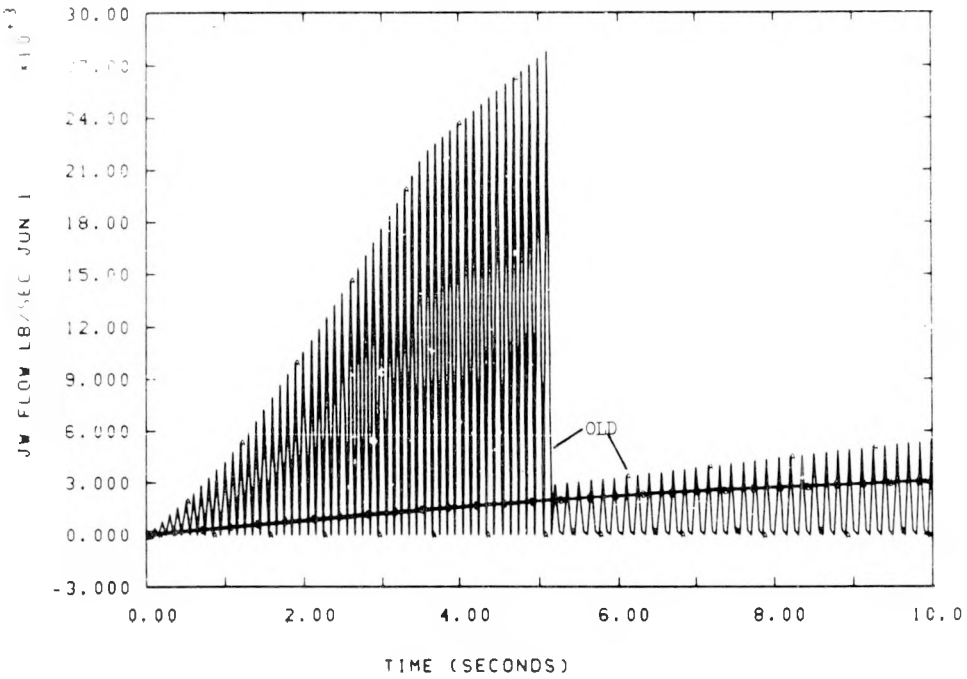

Figure 4-44. Effect on Flow in Polytropic Accumulator Tests, Old vs New Inertial Flow Estimator

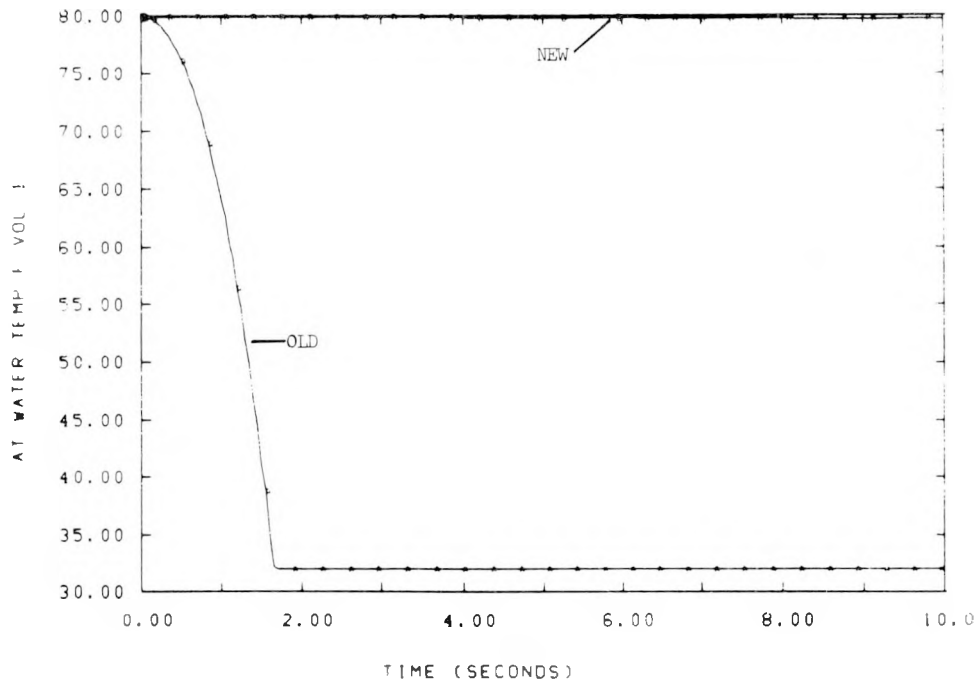

Figure 4-45. Effect on Water Temperature in Polytropic Accumulator Tests, Old vs New Inertial Flow Estimator

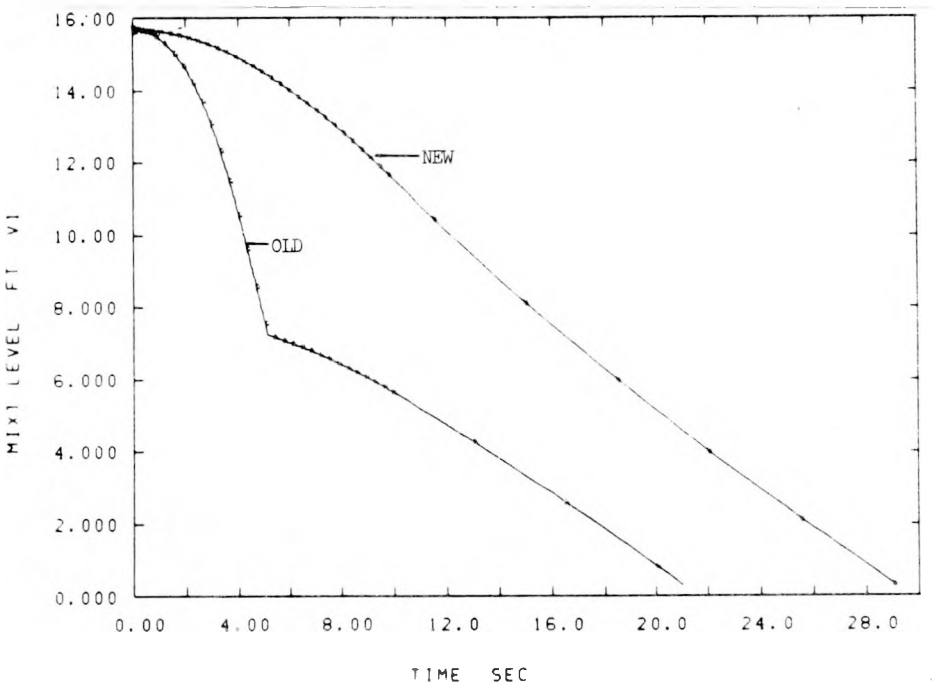

Figure 4-46. Effect on Mixture Level in Polytropic Accumulator Tests, Old vs New Inertial Flow Estimator

4.5 FRAP and FLOOD

The majority of our efforts this quarter have been concentrated on refining the calculation procedures for predicting carryout rate fractions (CRF) during reflood calculations. Modifications have been made to the RELAP4/MOD5 subroutine FLDEJ to calculate CRF more accurately. The subroutine now takes into account radial heat slab subdivisions wherein each subdivision represents fuel rod bundles at varying power levels. Since these bundles are located under both guide tubes and support columns, they experience different coolant conditions. To account for this radial power and coolant variation, the FLOOD mode of the RELAP code now requires additional input data for each radial division. These data comprise the following variables:

TMID (I)	Midplane clad temperature of the quenched portion of the rod at the beginning of reflood (°F),
HUNQCH (I)	Rod quench height (inches),
Q (I)	Power at rod midpoint (kW/ft),
XCOR (I)	Fraction of total core represented by each radial division (Σ XCOR (I) = 1) ,

where (I) goes from 1 through N, N being the number of radial divisions. TMID and HUNQCH are obtained from FRAP-T4 (Fuel Rod Analysis Program).* This code provides a detailed analysis of a single fuel rod based upon time-dependent coolant and rod power conditions input from the RELAP blowdown run. When analyzing rods located under guide tubes, coolant properties from the hot assembly are used as FRAP input. Conversely, for rods located under support columns, coolant properties from the average core are used. This recommended procedure is outlined in WCAP-8479-P (pp. 3-48).

A copy of the FRAP-T4 code was obtained from INEL and has been made operational on Sandia's CDC 7600 computer. Checkout runs are being made using the tape read option which obtains the time-dependent coolant conditions directly from the RELAP blowdown output tape. The generic FRAP code has been modified to include the same quench model as was previously used in Sandia's version of RELAP4/MOD5.

The sequence of calculations required to completely analyze a loss of coolant accident (LOCA) are outlined as follows:

1. Run the RELAP4/MOD5 code to obtain core coolant conditions for a LOCA up to the time when initial reflood occurs.

2. Use these time-dependent coolant conditions and power output levels as input conditions to the FRAP code to obtain quench levels and rod temperatures for the eight radial core divisions:

   For the rods located under the support columns, use average core coolant conditions.

   For the rods located under the guide tubes, use hot assembly coolant conditions. All of these rods can generally be combined into a single run using the rod power (kW/ft) of the hottest rod.

   As long as the rods remain quenched, the boundary conditions from the blowdown RELAP run are adequate. However, if a rod unquenches, an adiabatic heatup calculation is performed from the time the highest quenched elevation at or below the rod midplane unquenches to the beginning of reflood. The adiabatic assumption is simply that the rate of increase of stored energy in the heat slab is equal to the power generation. This calculation is performed to avoid misusing the Westinghouse carryout rate fraction correlation.

3. Use the quench levels and rod temperatures obtained from FRAP in conjunction with the RELAP blowdown output as initial data to calculate CRF for reflood.

---

*FRAP-T4, "A Computer Code for the Transient Analysis of Oxide Fuel Rods," CDAP-TR-78-027.

4.5.1 Sample Calculations

Sample calculations are currently being made to check out the RELAP (blowdown), FRAP (fuel rod), and RELAP (reflood) package. The UHL1 blowdown run has been used to supply the coolant conditions for FRAP. The core heat slabs in the run have been divided into eight radial divisions (Figure 4-47). Even though Westinghouse has 11 radial divisions, eight are being used in RELAP, because of storage limitations.

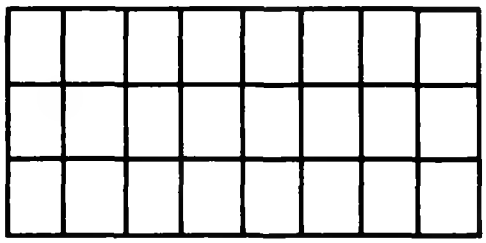

Figure 4-47. Core Heat Slabs

The first stack (slabs 1, 2, and 3) represents the hot assembly and the seven remaining stacks represent the average assembly. Using the power output of the first average core assembly (slabs 4, 5, and 6) as input to FRAP (with quench model) resulted in the quench pattern shown in Figure 4-48. It was determined from the blowdown data that the actual reflood phase is initiated at about 96 seconds. Therefore, from Figure 4-48 this slab must be considered completely unquenched (HUNQCH(1) = 0.0) at the beginning of the reflood run. Since the initial quench height used in the FLOOD program is strongly related to the core fill rate, it can be seen from this figure that the exact time at which reflood is initiated is extremely important.

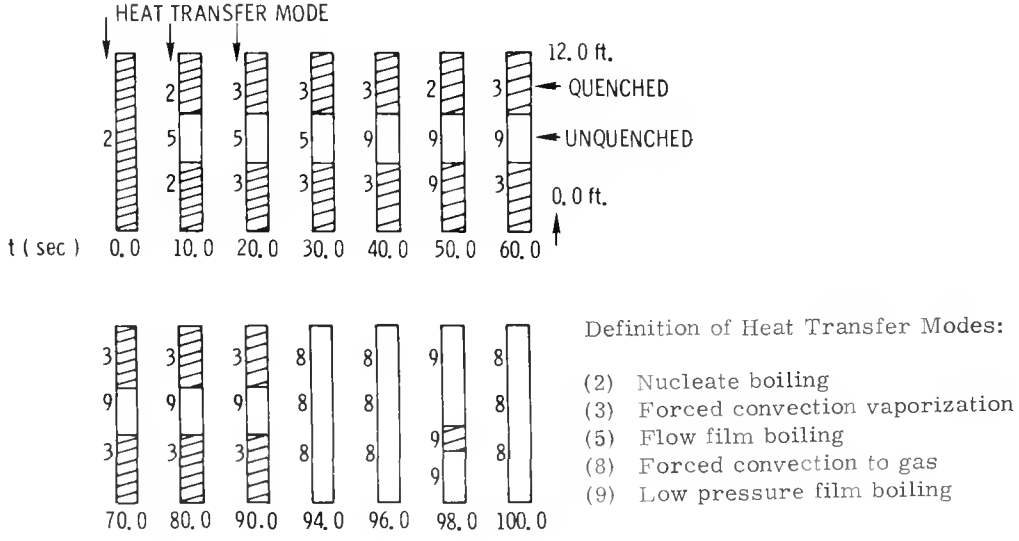

Figure 4-48. Fuel Rod Quench Height and Heat Transfer Modes as a Function of Time

4.5.2 Future Work

FRAP-T4 will be used to predict quench height and rod temperature for all eight radial heat slab divisions. These data will then be used to calculate the core reflood rate. Reflood data obtained with the use of FRAP-T4 will be compared to runs made before this update.

DISTRIBUTION:

US Nuclear Regulatory Commission
(356 copies for R3)
Division of Document Control
Distribution Services Branch
7920 Norfolk Ave
Bethesda, MD 20014

Kenforschungszentrum Karlsruhe (9)
Postfach 3640
7500 Karlsruhe 1
Federal Republic of Germany
Attn: Dr. J. P. Hosemann
Projekt Nucklear Sieherheit (PNS) (4)
Dr. M. Fischer
Projekt Nuklear Sicherheit (PNS)
Dr. H. Albrecht
Institut für Radiochemie (IRCH)
Dr. H. Holleck,
Institut für Material- und
Festkörperforschung (IMF)
Dr. W. B. Murfin
Projekt Nukleare Sicherheit (PNS)
Dr. M. Reimann
Institut für Reaktorbauelemente (IRB)

Prof. Dr.-Ing. F. Mayinger
Lehrstuhl und Institut für Verfahrenstechnik
TU Hannover
Callinstr. 36
3000 Hannover 1
Federal Republic of Germany

Milad Matthias
Dept. of Nuclear Studies and Safety
Ontario Hydro
700 University Ave. (H-16)
Toronto, Ontario
Canada M5G1X6

H. Seipel
BMFT
Federal Ministry for Research & Technology
53 Bonn
Federal Republic of Germany

Dr. E. Herkommer
Institute for Reactor Safety
5000 Koln 1
Gloschengasse 2
Federal Republic of Germany

Professor Dr. H. Unger
IKE
University of Stuttgart
7 Stuttgart - Vaihingen
Pfaffenwaldring 31
Federal Republic of Germany

Dr. Ian Brittain
United Kingdom Atomic Energy Authority
Atomic Establishment, Winfrith
Dorchester, Dorset
England

G. H. Kinchin
Safety & Reliability Directorate
Wigshaw Lane
Culcheth
NR Warnington, Cheshire
England

Dr. M. Peehs
KWU
Abt. Rb. 3
852 Erlangen
Postfach 325
Federal Republic of Germany

Dr. M. Dalle Donne (2)
Kernforschungszentrum Karlsruhe
Institut für Neutronenphysik und Reaktortechnik
7500 Karlsruhe 1
Postfach 3640
Federal Republic of Germany

Dr. H. Kottowski
c/o - Euratom Ispra
21020 Centro Euratom di Ispra
(Varese) Italy

US Nuclear Regulatory Commission (6)
Office of Nuclear Regulatory Research
Washington, DC 20555
Attn: W. C. Lyon
D. E. Solbert
T. Buhl
N. Zuber
S. Fabic
W. V. Johnston

US Nuclear Regulatory Commission (7)
Division of Systems Safety
Office of Nuclear Reactor Regulation
Washington, DC 20555
Attn: Z. R. Rosztoczy
B. Sheron
N. Lauben (3)
E. Throm
S. Hanauer

US Department of Energy (2)
Reactor Safety Research Coordination
Washington, DC 20545
Attn: R. W. Barber
T. E. McSpadden

DISTRIBUTION (Cont.):

US Department of Energy
Division of Naval Reactors
Washington, DC 20545
Attn: R. Brodsky

US Department of Energy
Operational Safety Division
Albuquerque Operations Office
P. O. Box 5400
Albuquerque, NM 87185
Attn: J. R. Roeder, Director

Westinghouse Electric Corporation
Research and Development Center
Churchill Boro
Pittsburgh, PA 15235
Attn: M. Mazumdar
Mathematics Department

Florida International University
Department of Statistics
Tamiami Trail
Miami, FL 33144
Attn: S. S. Shapiro

Argonne National Laboratory
9700 South Cass Avenue
Argonne, IL 60439
Attn: H. H. Hummel

Oak Ridge National Laboratory
Box Y, Bldg. 9201-3
Oak Ridge, TN 37830
Attn: M. H. Fontana

EG&G - Idaho, Inc. (10)
P. O. Box 1625
Idaho Falls, ID 83401
Attn: R. E. Rice
P. North
M Sahota
N. D. Cox
S. R. Risher
B. Saffell
G. W. Johnsen
D. M. Snider
T. K. Larson
A. W. Croneberg

Electric Power Research Institute (2)
3412 Hillview Avenue
Palo Alto, CA 94304
Attn: R. Gay
L. Agree

Offshore Power System
8000 Arlongton Expressway
Box 8000
Jacksonville, FL 32211
Attn: D. H. Walker

Westinghouse Advanced Reactor Division
P. O. Box 158
Madison, PA 15663
Attn: L. E. Strawbridge

Westinghouse Electric Corp. (2)
Bettis Atomic Power Laboratory
P. O. Box 79
West Mifflin, PA 15122
Attn: F. W. Lincoln
W. D. Peterson

Westinghouse Electric Corp. (3)
Nuclear Energy Systems
P. O. Box 355
Pittsburgh, PA 15230
Attn: R. P. Vijuk (2)
M. Y. Young

Battelle Pacific Northwest Laboratories
P. O. Box 999
Richland, WA 99352
Attn: C. McMonagle

Los Alamos Scientific Laboratory (3)
P. O. Box 1663
Los Alamos, NM 87545
Attn: M. McKay
W. Rivard
B. Daly

400 C. Winter
1200 L. D. Smith
Attn: L. D. Smith, 1260 (Actg)
1223 R. B. Easterling
1537 N. R. Keltner
4000 A. Narath
4216 K. L. Goin
4400 A. W. Snyder
4410 D. J. McCloskey
4412 J. W. Hickman
4420 J. V. Walker
4422 R. L. Coats
4422 H. G. Plein
4423 J. E. Powell
4424 P. W. Conrad
4424 R. L. Knight
4425 W. J. Camp
4441 M. Berman (10)
4441 L. D. Buxton (5)
4441 R. K. Byers
4441 R. K. Cole, Jr.
4441 L. Dike
4441 J. F. Muir
4443 D. A. Dahlgren
4450 J. A. Reuscher
4533 B. D. Zak
4550 R. M. Jefferson

DISTRIBUTION (Cont.):

5131 W. B. Benedick
5511 D. F. McVey
5511 R. R. Eaton
5511 D. O. Lee
5512 H. C. Hardee
5512 D. W. Larson
5520 T. B. Lane
5530 W. Herrmann
5533 H. J. Sutherland
5533 B. M. Butcher
5537 J. E. Smaardyk
5641 G. P. Steck
5830 M. J. Davis
5830 L. S. Nelson (5)
5831 N. J. Magnani
5831 T. M. Gerlach
5831 D. A. Powers (5)
5833 F. J. Zanner
5846 E. K. Beauchamp
5846 R. A. Sallach
8266 E. A. Aas
3141 T. L. Werner (5)
3151 W. L. Garner (3)
For DOE/TIC (Unlimited Release)
DOE/TIC (25)
(R. P. Campbell, 3172-3)